UNIVERSITY OF CALIFORNIA
Santa Barbara

InP Photonic Integrated Circuits Incorporating Photonic Crystals

A Dissertation submitted in partial satisfaction
of the requirements for the degree of

Doctor of Philosophy

in

Electrical and Computer Engineering

by

Marcelo I. Davanço

Committee in Charge:

Professor Daniel J. Blumenthal, Chair

Professor John E. Bowers

Professor Nadir Dagli

Professor Evelyn L. Hu

December 2005

UMI Number: 3202703

UMI Microform 3202703

ProQuest Information and Learning Company
300 North Zeeb Road
P.O. Box 1346
Ann Arbor, MI 48106-1346

The Dissertation of
Marcelo I. Davanço is approved:

Professor John E. Bowers

Professor Nadir Dagli

Professor Evelyn L. Hu

Professor Daniel J. Blumenthal, Committee Chairperson

December 2005

InP Photonic Integrated Circuits Incorporating Photonic Crystals

by

Marcelo I. Davanço

To whatever it is that makes airplanes fly.

Acknowledgements

First things first: I would like to thank Dr. C. E. Thomaz da Silva, who first suggested that I cross the equator, all the way from the other hemisphere, to obtain a Ph.D. degree in the United States, possibly in California, where he himself had graduated. It has been a long and at times not so smooth ride, however I certainly feel glad to have taken his suggestion to heart. I would like to thank Professor Hugo Hernández-Figueroa from the University of Campinas, Brazil, for supporting me and for offering very good advice during the application period.

I am very thankful to my Ph.D. advisor, Professor Dan Blumenthal, for giving me the opportunity to work in his research group, for his generosity, patience and good advice.

My experience at UCSB would undoubtedly not have been as pleasant without the support, both professional and personal, of my co-workers at the Optical Communications and Photonics Networks group: Lavanya Rau, Milan Mashanovitch (formerly Mašanović), Wei Wang, Vikrant Lal, Joe Summers, Roopesh (Roop) Doshi, Ramesh (Meshie, Meshi, Meshy) Rajaduray (*Senior Member, VPS*), Suresh (Sharky) Rangarajan, Amy Rushton, Bengt-Erik Olsson, Olga Lavrova, Henrik Poulsen, David Wolfson, Zhaoyang Hu, Wenbin Zhao, Lisa Garza, John Mack, Walt Donat, Melissa Chun, Ali Hitomi. It has been a great pleasure to work with such smart, knowledgeable, helpful and fun (and sometimes just plain annoying) individuals. I feel particularly indebted to the older OCPN crew members

Lavanya, Milan and Wei for the constant encouragement and always very useful technical help and discussions.

Quite a few people have helped me one way or another with a large number of different issues (e.g., device processing, borrowing equipment, technical discussions): Maura Rauburn, Kian-Giap Gan, Jon Barton, Matt Sysak, Chad Wang, Rintaro Koda, John Hutchinson, Kevin Hennessy, Cedric Meier, Chiou-Fu Wang, Lidong Zhang, Yingda Dong. I would like to thank Chuck Reese for introducing me to the field of photonic crystals. Also, I would like to thank James Raring, who grew the wafers (or rather, the wafer) used to produce the devices investigated in this work. I am very indebted to Aimin Xing, with whom I collaborated very closely and who transferred to me quite a lot of his vast knowledge of semiconductor device processing and photonic crystal fabrication.

I would like to thank Professor Evelyn Hu for her kindness and promptness and the many very helpful discussions on fabrication issues. I would also like to thank Professor John Bowers for the good advice and support and for pushing me to get certain results done. I am very grateful to Professor Nadir Dagli, who has patiently endured more than a few discussions on many curiously unusual ideas, always offering very good insights, useful suggestions, sensible advice and (alas, many times) frank opinions. Finally, I would like to thank Professor Claude Weisbuch for the very useful discussions on photonic crystals.

I could not possibly leave out of my acknowledgements our very competent cleanroom staff: Jack Whaley, Brian Thibeault, Don Freeborn, Bob Hill, Ning Cao, Luís Zuzunaga. I would like to specially thank Bill Mitchell, maintainer of

the e-beam writer (or the Millenium Falcon for the intimate), for saving me from many a pickle in the e-beam dungeon.

I would like to thank my roommate Marco Zuliani (*Fellow, VPS*) for the great companionship throughout all this time, for teaching me how to curse in truly creative ways in languages I never knew existed, and finally for demonstrating how half a pound of pasta might just not be enough. I would also like to thank everyone I was lucky enough to meet and become friends with along the way: Vittorio Badalassi, Gabriel Gomes (*Member, VPS*), Anna Salvatella, Rogério Feris (*Member, VPS*), Paola Matulli, Paolo Maccarini, Marco Ruocco (*Member, VPS*), Rodrigo Hurtado, António Santos, Daniel Lasaosa, Alessandro Chini (*Member, VPS*), Stefano Camatel (*Member, VPS*), Maria Montes, Dmytry Fedorov, (*Member, VPS*), Anna and Kevin Pedretti, Elison Matioli, Marco Carli (*Member, VPS*), Mylène and Marcelo Carvalho, Elisa Drelie.

A very special thanks is reserved for Emily Burmeister, who has been a wonderful companion throughout the past year, ever since our acquaintances were properly (and in fact quite well indeed) made. Incidentally, it was during this period that things in the lab started to take off...

It goes without saying that without the love and support of my parents, Osvaldo and Tsuneko Davanço, none of this would ever have come to be. I just could not thank them enough.

Curriculum Vitæ

Marcelo I. Davanço

Personal

1975	Born January 25th in Campinas, Brazil

Education

2000	Mestre em Engenharia Elétrica, Universidade Estadual de Campinas (UNICAMP), Campinas, Brazil
1998	Engenheiro Eletricista, Universidade Estadual de Campinas (UNICAMP), Campinas, Brazil

Experience

2000 – 2005	Graduate Student Researcher, University of California, Santa Barbara.
1998 – 2000	Graduate Student Researcher, Universidade Estadual de Campinas, Campinas, Brazil
1997 – 1998	Intern, Optical Networks Division, CPqD - Telebrás, Campinas, Brazil
1996 – 1997	Undergraduate Student Researcher, Universidade Estadual de Campinas, Campinas, Brazil

Awards

CNPq Undergraduate Research Fellowship

CAPES Master's Degree Program Fellowship

Selected Publications

1. M. Davanço, A. Xing, J. Raring, E. L. Hu, and D. J. Blumenthal, "Broadband Notch Filters Based on Quasi-2D Photonic Crystal Waveguides for InP-based Monolithic Photonic Integrated Circuits", *submitted to IEEE-Jour. Sel. Top. Quantum Electr. Nov. 2005.*

2. M. Davanço, A. Xing, J. Raring, E. L. Hu, and D. J. Blumenthal, "Compact Broadband Photonic Crystal Filters with Reduced Back-reflections for Monolithic InP-based Photonic Integrated Circuits", *in preparation.*

3. M. Davanço, A. Xing, J. Raring, E. L. Hu, and D. J. Blumenthal, "Broadband Photonic Crystal Passive Filters for Monolithically Integrated InP Photonic Integrated Circuits", *submitted to OFC 2006.*

4. M. Davanço, A. Xing, E. L. Hu, D. J. Blumenthal, "Perspectives on the application of InP-based photonic crystal waveguides for optical signal processing", Invited Talk, presented at SPIE Optics East 2005, Boston, MA, 23-26 October 2005.

5. M. Davanço, A. Xing, J. Raring, E. L. Hu, and D. J. Blumenthal, "Detailed characterization of slow and dispersive propagation near a mini-stop-band of an InP photonic crystal waveguide," Opt. Express 13, 4931-4938 (2005).

6. A. Xing, M. Davanço, S. Camatel, D. J. Blumenthal, E. L. Hu, "Pulse Compression in Line Defect Photonic Crystal Waveguide", OFC 2005, Paper OWD5.

7. A. Xing, M. Davanço, D. J. Blumenthal, E. L. Hu,, "InP photonic crystal membrane structures: fabrication accuracy and optical performance", Applied Physics Letters, vol.85, no.4, 26 July 2004, pp.522-4.

8. A. Xing, M. Davanço, D. J. Blumenthal, E. L. Hu, "Fabrication of InP-based two-dimensional photonic crystal membrane", Journal of Vacuum Science & Technology B Microelectronics & Nanometer Structures Processing Measurement & Phenomena, vol.22, no.1, Jan. 2004, pp.70-3.

9. M. Davanço, D. J. Blumenthal, "Design of an InP-Based Deeply-Etched Waveguide Grating for the Implementation of Entire C- or L Band Rejection Filters", 2004 IEEE LEOS Annual Meeting Conference Proceedings, Paper TuQ2.

10. Z. Hu, M. Davanço, D. J. Blumenthal, "Extinction ratio improvement by strong external light injection and SPM in an SOA for OTDM pulse source using a DBR laser diode", IEEE Photonics Technology Letters, vol.15, no.10, Oct. 2003, pp.1419-21.

11. A. Xing, M. Davanço, D. J. Blumenthal, E. L. Hu, "Systematic transmission characterization of 2D InP photonic crystal membrane structures", Quantum Electronics and Laser Science (QELS). Postconference Digest Optical Soc. of America, 2003, pp.2.

12. M. Davanço, P. Holmström, D. J. Blumenthal, L. Thylén, "Directional coupler wavelength filters based on waveguides exhibiting electromagnetically induced transparency", IEEE Journal of Quantum Electronics, vol.39, no.4, April 2003, pp.608-13

13. E. L. Hu, A. Xing, M. Davanço, C. Reese, D. Blumenthal, "InP photonic crystal membrane structures", Invited Talk, 2003 International Conference Indium Phosphide and Related Materials. Conference Proceedings (Cat. No.03CH37413). IEEE. 2003, pp.69-73.

14. M. Davanço, D. J. Blumenthal, L. Thylén "An Extremely Narrowband Directional Coupler Wavelength Filter Based on Electromagnetically Induced Transparency," Technical Digest of the Integrated Photonics Research Conference (IPR '02), Vancouver, Canada, Paper IThF2, September 17-19, (2002).

15. M. Davanço, D. J. Blumenthal, "Exploring slow and dispersive propagation in 2D line-defect photonic crystal waveguides", 2003 IEEE LEOS Annual Meeting Conference Proceedings, Vol.1, 2003, pp.216-1.

16. C. E. Rubio-Mercedes, M. I. Davanço, H. E. Hernandez-Figueroa, "Padé boundary conditions for the frequency domain finite-element solution of arbitrary planar junctions", Proceedings of the 2001 SBMO/IEEE MTT-S International Microwave and Optoelectronics Conference. (Cat. No.01TH8568). IEEE. Part vol.1, 2001, pp.453-6 vol.1.

17. M. I. Davanço, C. E. Rubio-Mercedes, H. E. Hernández-Figueroa, "Novel boundary condition for the finite-element solution of arbitrary planar junctions", IEEE Photonics Technology Letters, vol.13, no.1, Jan. 2001, pp.46-8.

18. M. I. Davanço, C. E. Rubio-Mercedes, H. E. Hernández-Figueroa, "Novel boundary condition for the finite-element simulation of planar optical junctions", Trends in Optics and Photonics. Integrated Photonics Research. Vol.45. Technical Digest. Postconference Edition. Opt. Soc. America. 2000, pp.54-6.

Abstract

InP Photonic Integrated Circuits Incorporating Photonic Crystals

Marcelo I. Davanço

Photonic crystals are materials with a periodic and usually very strong index modulation offering crystal-like propagation characteristics for electromagnetic waves. These structures have for many years attracted much attention in the integrated photonics community, offering exciting prospects for the realization of extremely compact photonic devices and circuits.

The work presented is an investigation on possible applications of quasi-2D photonic crystals in InP-based monolithic photonic integrated circuits for optical communications, with focus on stop-band formation and slow and dispersive waveguide propagation. Initially, a theoretical assessment of band-edge propagation in line-defect photonic crystal waveguides is carried out based on calculated photonic band structures, numerical simulations and simplified analytical models. Capabilities and limitations of the line-defect waveguide filtering characteristics are discussed in detail.

The subsequent experimental assessment involved the development of a novel fabrication process to produce photonic integrated circuits incorporating deeply etched photonic crystals based on a mature integration platform. The photonic crystals consisted of lattices of air holes of diameters on the order of a few hundreds of nanometers, etched more than 2.5μm into the semiconductor material.

Devices including both electrically pumped ridge waveguides and photonic crystal structures were fabricated and used for the characterization of the photonic crystal filter characteristics, including phase information. Both the fabrication technique and experimental characterization technique are explained.

Experimental results are presented demonstrating the availability of 20dB-extinction transmission stop-bands with bandwidths of tens of nanometers in structures of less than 80μm in length. Finally, results showing slow and extremely dispersive band-edge propagation are presented.

Contents

List of Figures

Chapter 1

Introduction

1.1 Photonic Crystals

Since the introduction in 1987 of the concept of Photonic Band-Gaps (PBG) as a means to inhibit spontaneous emission [1], the number of publications per year on the topic of photonic crystal materials has increased exponentially [1]. This enormous interest was fuelled along the years by the prediction of many very exciting properties and possibilities related to electromagnetic wave propagation and confinement: complete wave confinement for waveguiding and resonators [2, 3]; extreme feature-size reduction for dense photonic integration [4, 5]; enhanced nonlinearities [6, 7]; highly refractive propagation [8, 9]; anomalous propagation leading to effective 'negative-refractive-index' propagation [10, 11]; etc.

The applicability of many such properties in real-life devices, however, is in general not straightforward; several times, simpler, better-understood structures and techniques prove to be just as effective for particular applications, offering

[1] In fact, according to the regularly updated online photonic band-gap reference list compiled by J. P. Dowling at the Louisiana State University (http://phys.lsu.edu/~jdowling/pbgbib.html), the number of publications per year can be quite well fitted with the expression $N_{pub.} = 6 \cdot \exp[(Y - 1987)/3]$, Y being the year since 1987.

thus a clear advantage over Photonic Crystal (PC) alternatives, regarding simplicity of implementation and design. One good example is the realization of *closed* waveguides with confinement provided by the PBG, which in simulations allows the realization of extremely low-loss sharp bends [12], envisaging extremely compact photonic circuits [2]. As it turns out, similar performances have been predicted for high-index-contrast waveguides [13]; experimentally, these have in fact outperformed equivalent PC waveguides in terms of losses [14]. The search for sensible photonic crystal applications thus is by itself a rather hard challenge.

The purpose of the present work was the development of novel PC-based applications for InP Photonic Integrated Circuits (PICs) [15]. Rather than aiming towards the realization of entirely PC-based circuits, the present approach consisted in incorporating PC structures to small portions of a standard PIC with the purpose of adding functionality and reducing overall circuit dimensions, while maintaining low overall losses by minimizing interaction with lossy PC regions.

The investigation was focused on two promising, unique properties offered by PC waveguides: the formation of very broad guided-wave stop-bands and slow and dispersive band-edge propagation, both of which offer good prospects for the realization of monolithically integrated optical filters. The exploration was biased towards practical applications, keeping in mind aspects that could be understood or achieved in a straightforward manner, or those that could not be easily avoided.

Photonic Integrated Circuits Incorporating Photonic Crystals

Semicondutor PICs are generally composed of a series of planar structures (waveguides, trenches, mesas, mirrors, etc) realized on the surface of epitaxially grown wafers. Semiconductor fabrication processes consist in essence of a series of steps involving deposition and etching of semiconductor, metal or dielectric materials at selected areas on the wafer surface.

The possibilities of implementation of the different structures of a PIC are strongly limited by the availability of suited fabrication techniques. In general, much time, effort and money are involved in the development of a stable fabrication process; novel processes as such are developed from stable, previously available ones, through the introduction of a few compatible steps, making use of the available fabrication tools and techniques. This was in fact the approach taken in the present work, which ended up defining the type of PC structure to be explored: quasi-2D photonic crystals. The following section describes the detail the most important features of these structures.

1.2 Quasi-2D Photonic Crystals

Many different implementations of PCs have been proposed or demonstrated in the literature, however, keeping in mind the many issues involved in their incorporation within functional planar Photonic Integrated Circuits (PIC), those of the lattice-of-holes kind are in general chosen given their fabrication simplicity: the process consists mainly of etching 2D periodic arrays of holes on a semiconduc-

tor wafer. Crystals thus implemented present periodicity in only two dimensions; confinement in the remaining direction grants quasi-2D crystal-like wave propagation on the plane. In general the epitaxial structure forms a slab-waveguide which provides weak or strong vertical confinement, depending upon the refractive index discontinuity between the different material layers.

One may separate quasi-2D crystals into two classes, depending on whether the vertical confinement is weak or strong. Schematics of the two kinds of quasi-2D crystals are depicted in Figs. 1.1(a) and 1.1(b).

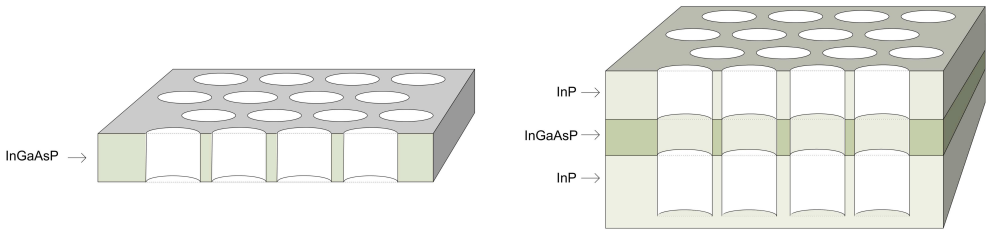

(a) (b)

Figure 1.1: (a) Schematic of strong vertical confinement (membrane-type) lattice-of-holes PC. (b) Schematic of weak vertical confinement (slab-type) lattice-of-holes PC.

The advantages and disadvantages of each scheme, as well as the current state-of-the-art are discussed in the following paragraphs.

1.2.1 Strong Vertical Confinement Photonic Crystals

Strong vertical field confinement provided by large vertical index contrasts allows the existence of actual vertically bound Bloch modes (i.e. Bloch modes with no intrinsic out-of-crystal-plane losses) in infinite structures, which translates into lower propagation losses [16]. Theoretical analysis and design become

more involved in this case, since in general full-vector, three-dimensional field computations are required for a satisfactory assessment of the crystal properties. In general, however, the requirement on hole depth is not very demanding, since crystals are defined on reasonably thin (on the order of a few hundreds of nanometers) semiconductor layers.

Strongly confining PCs have been realized in Silicon and Silicon-on-Insulator (SOI) material [17, 18, 19], GaAs [20] and InP [21, 22]. Strong confinement in Si, GaAs and InP systems is achieved with the removal of underlying substrate material, in which case actual *membranes* of photonic crystal material are formed, as shown schematically in Fig. 1.1(a). In the case of SOI and certain types of GaAs systems, the substrate is kept, however presenting a large index step with respect to the confinement layer.

The main disadvantage of membrane systems is the extra difficulty involved in the monolithic integration with PICs, due to the fragility of the fabricated structures. Notice, though, that this does not pose a fundamental limitation to the applicability of such structures.

The lowest propagation losses reported so far for line-defect photonic crystal waveguides have been obtained from strongly guided structures in Si membranes: 0.7dB/mm [14]. These losses were achieved with waveguides with extremely smooth sidewalls. It must be noted though that extremely compact (0.5nm width) high quality strip waveguides on SOI material have been reported to offer lower levels of propagation losses (0.35dB/mm) [23]. Moreover, losses per 90°-bend as low as 0.013dB were reported, clearly proving the value of such structures. These

waveguides are advantageous relative to PC guides from the point of view of the simplicity of fabrication and analysis and are thus in principle more convenient for the realization of highly integrated waveguide-based photonic circuits. On the other hand, these do not offer the same dispersive propagation characteristics found in PC waveguides.

Optically pumped, InP-membrane micro-cavity quasi-2D PC lasers were reported for the first time in InGaAsP material with multiple quantum-wells in [24]. Following that, many membrane-based surface-emitting lasers were demonstrated, good examples of which are [25, 26, 27]. Electrically-driven membrane InGaAsP lasers were reported in [28, 29].

The highest micro-cavity quality factor achieved so far was of 600,000, reported in [19]. The cavity was realized on a Si membrane, designed such that the cavity mode presented fewer radiative (spatial) spectral components. This allowed the development of the resonator-based, extremely compact multi-channel drop-filters reported in [30], which demonstrates the integration potential offered by membrane-based PC structures.

1.2.2 Weak Vertical Confinement Photonic Crystals

A slab-type lattice-of-holes PC consists of a weakly guided slab waveguide onto which very deep holes are etched, as schematized in Fig. 1.1(b). Idealized structures consisting of infinitely deep holes have been predicted to be intrinsically leaky [31]; reference [31] however predicts radiation losses to scale with the square

of the slab index-step, $(\Delta\epsilon)^2$, which means lower radiation leakage for weakly confining structures in leaky-wave propagation regimes [2]. This result was obtained in a perturbative approach with many simplifying assumptions by considering both the 3D index distribution and PC modes to be separable (i.e., $f(x, y, z) = u(x, z)v(y)$, y being the direction of holes) and by considering dipole-like radiation from the effective perturbations introduced in the slab waveguide.

Accurate 3D computational models have later shown good evidence that the intrinsic radiation losses are not necessarily high and in some cases might even compare to what is found in strongly confining geometries in leaky propagation regimes [32, 33].

Etched hole imperfections such as insufficient depth [34, 35, 36, 37], sidewall verticality [38, 37] and irregular bottom shapes [39, 37] have been pointed out as main sources of out-of-plane radiation losses in real PCs. This imposes strict requirements on etching techniques for the realization of low-loss PCs, since typical aspect-ratios of more than 10 must be achieved, corresponding to etch-depths beyond 2μm, with very straight sidewalls.

The effects of sidewall roughness on the reflectivity of 1D PCs has been investigated in [40], where a band-gap red-shift and narrowing was theoretically observed using Finite-Difference Time-Domain simulations. In Ref. [41], low-index-contrast 1D air-trench PCs were related to higher radiation losses caused by sidewall imperfections, by considering the latter as radiating dipoles excited by an incident

[2]Strong-confinement PCs also present unconfined modes in the vertical direction.

waveguide mode. Higher losses were attributed to a less-effective re-capture of power radiated by the effective dipoles in weakly guided PCs.

Weakly confining quasi-2D structures reported in the literature are in general either GaAs- or InP-based. GaAs structures in general provide slightly higher confinement factors, given the GaAs-AlGaAs index discontinuity. These in general are used for wavelengths approaching 1μm [42]. The present work is concerned with InP-based PCs, keeping in mind their application in monolithic photonic integrated circuits for optical communications wavelengths ($\lambda \approx 1.5\mu$m).

Deep Hole Etching

High-density plasma etching techniques have yielded the best results in terms of deep-hole etching. For InP material, Cl_2 chemistries are in general used under low pressures (<10mTorr), high temperatures (>200°) and high plasma densities. Electron-Cyclotron Resonance (ECR) Reactive Ion Etching (RIE) has been used in [43, 44, 45], using a Cl_2/Ar gas mixture to produce etch-depths exceeding 3.5μm, .

Chemically assisted Ion Beam Etching (CAIBE) with a Cl_2/Ar mixture at a low pressure has been shown to produce 4.5-μm-deep holes with diameters above 350nm, with very straight sidewalls and tapered bottoms [46]. Estimated losses in this case were lower than those found in a similar structure etched with ECR [44] and were related to a lower hole-bottom sidewall angle. This etching technique was also able to produce 250-nm-diameter, 4.5-5.5μm-deep holes in [47], with extremely straight sidewalls.

The Inductively Coupled Plasma (ICP) source technique on the other hand has been used in [48] with $SiCl_4$ to produce >3.5-μm-deep holes with very straight sidewalls, which yielded comparable lower losses than the equivalent ECR-etched PCs of [44]. The better performance was once again accredited to a smaller tilt angle, as well as larger hole depth. Similar etching conditions also produced 2.8-3.7μm-deep holes with aspect-ratios of 12 and 14 in [49].

In the present work, ICP has been used with a Cl_2/Ar mixture at 2.5mTorr and 200°C to produce > 2-μm-deep holes with similar hole-morphology characteristics as above. The present technique was on the other hand capable of producing etch-depths exceeding 3.0μm for$\approx$ 240nm-diameter holes.

Waveguide Losses

In terms of waveguide losses, the lowest reported to date were 1.8dB/mm for the CAIBE-etched PCs of [47] and 1.5dB/mm for the ECR-etched PCs of [45]. Both estimates were obtained from triangular lattice three-line-defect waveguides in the Γ-K ($W3^{(K)}$) direction in slightly different epitaxial wafers. Losses of 0.2dB/mm were also reported in the latter reference, triangular lattice seven-line-defect waveguide ($W7^{(K)}$), which has a much wider waveguide channel.

The loss figures above were obtained with relatively thin top InP claddings (0.6μm in the former 0.2μm in the latter case) and thicker waveguide layers (1.6μm in the former 0.9μm in the latter case), which seems to point to the fact that larger confinement factors may lead to lesser interaction with imperfect hole-bottoms and therefore lesser losses. Reference [50] on the other hand relates higher losses to

higher confinement factors and points out that proper optimization of the vertical epi-structure (based on e.g. the analytical expressions obtained in [31, 39, 38]) is required for loss minimization.

In the present work, the epitaxial structure included waveguide and top cladding layers of 300nm and 1.0μm respectively. This structure was based on an optimized platform for photonic integrated circuits [51]. The top cladding was highly p-doped and was topped by an equally highly p-doped InGaAs contact layer, both features which contribute to increase mode propagation losses. In addition, etched holes were $\approx$2.5-μm deep, barely enough to cover the entire slab-mode profile. Losses obtained for a triangular lattice three-line-defect waveguides in the Γ-M direction (which has a much narrower channel width than its Γ-K counterpart) were estimated to be $\approx$13dB/mm. As proposed in [49], this may be improved by 1) deeper hole etching and 2) proper epi-structure design.

It must be pointed out that rigorous 3D computational PC models have shown that losses of single-line-defect waveguides were at least two orders of magnitude higher in the deeply etched (infinite hole) case than in equivalent strongly confining PCs [52]. On the other hand, weakly confining waveguides with much wider channel widths (e.g. >3-line defects) present losses up to three orders of magnitude lower than their single-line counterparts, reaching in some cases compatible levels to those found in strongly confining single-line defect waveguides in the non-leaky regime (i.e. below the air light-line) [33, 52].

Monolithic Integration with Photonic Integrated Circuits

The main advantage offered by slab-type PCs is the possibility of simpler incorporation with standard photonic integrated circuits. Additionally, theoretical analysis and design are considerably simplified: despite the fact that most modes of deeply etched PC waveguides are intrinsically leaky, effective 2D PC band-structures can still approximate quite well those obtained from a full-3D calculation [53]. Given a complete vertical overlap between slab modes and etched-hole profiles, it is possible to assume Bloch modes of the quasi-2D crystal to be composed of slab-mode waves propagating in the crystal plane, coupled by the 2D lattice. As such, an effective band-structure can be obtained considering the background effective index to be that of the considered slab-mode of the unperturbed vertical-layer structure. The existence of 2D Bloch modes at specific frequencies can then be directly correlated to transmission or reflection measurements from real devices. This procedure has in fact been carried out successfully in various articles[36, 53, 39, 54]. Notice that 2D waves can be separated into two classes, TE and TM, respectively having only electric or magnetic field components on the propagation plane; PC modes are classified accordingly, with respect to the crystal plane.

Ridge waveguide lasers with PC mirrors were first realized in GaAs, providing light at $\lambda \approx 800\mu$m [55] (here, CAIBE was used to produce 2-3μm-deep holes). Later, a similar laser was demonstrated in InP at $\lambda \approx 1.55\mu$m, however with a shallow-rib waveguide [56]. In both cases, the laser cavity was very short, on the

order of 200μm. Power levels exceeding 10mW were reported for currents around 300mA (pulsed) in the first case, with a threshold current close to 100mA. In the latter case, threshold currents below 20mA were observed, however with a maximum output powers of 9mW due to device heating.

Tunable coupled-cavity lasers composed exclusively of PC line-defect waveguides were demonstrated in [57], demonstrating the good potential for device size reduction. The two laser cavities in this case were approximately 200μm in length.

1.3 Description of this Thesis

The first chapter of this thesis includes theoretical and practical considerations regarding 2D and quasi-2D photonic crystals necessary for the understanding of the following chapters. The material includes basic theoretical concepts and a brief description of the method used for band-structure calculation, as well as a discussion on deep-hole etching.

Chapter 3 covers in depth wave propagation in 2D line-defect waveguides, with focus on slow and dispersive band-edge propagation. The discussion is done based on calculated band-structures and Finite-Difference Time-Domain (FDTD) simulations, as well as in generalized 1D Coupled-Mode Theory (CMT) equations, which seem to approximate band-edge propagation with reasonable accuracy [42, 54].

Chapter 4 details the fabrication process used to produce test devices and deeply etched photonic crystals. The entire process is described initially, then relevant aspects of the electron-beam lithography and dry-etching techniques are discussed next.

Chapter 5 explains many aspects of the experimental characterization process, including the theory and analysis of Müller matrices, extensively used to obtain the results presented in Chapter 6.

In Chapter 6 experimental measurement results are presented for four different types of photonic crystal-based structures: one extremely compact grating filter based on a bulk rectangular lattice crystal; a line-defect waveguide presenting a mini-stop-band for TM polarization, offering slow and extremely dispersive band-edge propagation; multi-mode asymmetric line-defect waveguides offering broad-band stop-bands convenient for the realization of monolithically integrated notch filters; an extremely compact single-mode line-defect waveguide offering very slow band-edge propagation.

Finally, general conclusions and suggestions for future work are presented in Chapter 7.

Main Thesis Contributions

The present investigation yielded the development of a novel fabrication process for monolithic, InP-based photonic integrated circuits incorporating deeply etched photonic crystals. The newly developed PIC platform extends the set of structures available for device design based on the mature platform from whence it was

derived. Clearly, design flexibility is gained, envisaging the development of novel functions and reduction of circuit dimensions.

The investigation on slow and dispersive band-edge propagation in PC line-defect waveguides provides insight into the involved mechanisms and the relevant parameters for filter design. The investigation in fact is an attempt towards the description of PC waveguides in terms of specific transfer functions, which is in general taken for granted in the literature.

Finally, the experimental results presented show good evidence, complementary to that found in the literature, of the potential of deeply etched photonic crystal as monolithically integrated filtering elements.

References

[1] E. Yablonovitch, "Inhibited spontaneous emission in solid-state physics and electronics," *Phys. Rev. Lett.*, vol. 58, no. 20, 1987.

[2] A. Mekis, J. C. Chen, I. Kurland, S. Fan, P. R. Villeneuve, and J. D. Joannopoulos, "High transmission through sharp bends in photonic crystal waveguides," *Phys. Rev. Lett.*, vol. 77, p. 3787, 1996.

[3] A. Mekis, S. Fan, and J. D. Joannopoulos, "Bound states in photonic crystal waveguides and waveguide bends," *Phys. Rev. B*, vol. 58, no. 8, 1998.

[4] S. Fan, P. R. Villeneuve, J. D. Joannopoulos, and H. A. Haus, "Channel drop filters in photonic crystals," *Optics Express*, vol. 3, no. 1, 1998.

[5] J. Joannopoulos, P. Villeneuve, and S. Fan, "Photonic crystals: Putting a new twist of light," *Nature(London)*, vol. 387, pp. 143–149, 1997.

[6] K. Sakoda and K. Ohtaka, "Sum-frequency generation in a two-dimensional photonic lattice," *Phys. Rev. Lett.*, vol. 43, no. 8, 1996.

[7] J. N. Winn, S. Fan, and J. D. J. abd E. P. Ippen, "Interband transitions in photonic crystals," *Phys. Rev. B*, vol. 59, no. 3, 1999.

[8] H. Kosaka, T. Kawashima, A. Tomita, M. Notomi, T. Tamamura, T. Sato, and S. Kawakami, "Self-collimating phenomena in photonic crystals," *App. Phys. Lett.*, vol. 74, no. 9, 1999.

[9] B. Gralak, S. Enoch, and G. Tayeb, "Anomalous refractive properties of photonic crystals," *J. Opt. Soc. Amer. A*, vol. 17, no. 6, 2000.

[10] M. Notomi, "Theory of light propagation in strongly modulated photonic crystals: Refractionlike behavior in the vicinity of the photonic band gap," *Phys. Rev. B*, vol. 62, pp. 10696–10705, 2000.

[11] C. Luo, S. G. Johnson, J. D. Joannopoulos, and J. P. Pendry, "All-angle negative refraction without negative effective index," *Phys. Rev. B*, vol. 65, pp. 201104:1–4, 2002.

[12] J. D. Joannopoulos, R. D. Meade, and J. N. Winn, *Photonic Crystals: Molding the Flow of Light*. Princeton, N.J.: Princeton, 1995.

[13] C. Manolatou, S. G. Johnson, S. Fan, P. R. Villeneuve, H. A. Haus, and J. D. Joannopoulos, "High-density integrated optics," *Jour. Lightwave Technol.*, vol. 17, no. 9, 1999.

[14] Y. A. Vlasov and S. J. McNab, "Waveguiding in silicon-on-insulator photonic crystal and single-mode strip waveguides," in *IEEE LEOS Annual Meeting Conference Proceedings*, pp. 809–810, 2004.

[15] L. A. Coldren and S. W. Corzine, *Diode Lasers and Photonic Integrated Circuits*. New York: Wiley-Interscience, 1999.

[16] S. G. Johnson, S. Fan, P. R. Villeneuve, J. D. Joannopoulos, and L. A. Kolodziejski, "Guided modes in photonic crystal slabs," *Phys. Rev. B*, vol. 60, pp. 5751–5758, 1999.

[17] S. J. McNab, N. Moll, and Y. A. Vlasov, "Ultra-low loss photonic integrated circuit with membrane-type photonic crystal waveguides," *Opt. Express*, vol. 11, pp. 2927–2939, 2003.

[18] M. Notomi, A. Shinya, S. Mitsugi, E. Kuramochi, and H.-Y. Ryu, "Waveguides, resonators and coupled elements in photonic crystal slabs," *Optics Express*, vol. 12, pp. 1551–1561, 2004.

[19] B. Song, S. Noda, T. Asano, and Y. Akahane, "Ultra-high-q photonic double heterostructure nanocavity," *Nature Mater.*, vol. 4, March 2005.

[20] N. Ikeda, Y. Sugimoto, Y. Tanaka, K. Inoue, and K. Asakawa, "Low propagation losses in single-line-defect photonic crystal waveguides on gaas membranes," *Jour. Select. Areas Communic.*, vol. 23, no. 7, 2005.

[21] A. Xing, M. Davanço, D. J. Blumenthal, and E. L. Hu, "Fabrication of InP-based two-dimensional photonic crystal membrane," *J. Vac. Sci. Technol. B*, vol. 22, no. 8, pp. 70–73, 2004.

[22] A. Scherer, O. Painter, J. Vuckovic, and T. Yoshie, "Photonic crystals of confining, guiding, and emitting light," *IEEE Trans. Nanotech.*, vol. 1, pp. 4–11, March 2002.

[23] Y.A.Vlasov and S. J. McNab, "Losses in singlemode silicon-on-insulator strip waveguides and bends," *Opt. Express*, vol. 12, pp. 1622–1631, 2004.

[24] O. Painter, R. Lee, A. Scherer, A. Yariv, J. D. O'Brien, P. D. Dapkus, and L. Kim, "Two-dimensional photonic band-gap defect mode laser," *Science*, vol. 284, pp. 1819–1821, 1999.

[25] H.-Y. Ryu, S.-H. Kim, H.-G. Park, and Y.-H. Lee, "Characteristics of single defect laser modes in a two-dimensional square lattice photonic crystal slab," *Jour. App. Phys.*, vol. 93, no. 2, 2003.

[26] M. Loncar, T. Yoshie, A. Scherer, P. Gogna, and Y. Qiu, "Low threshold photonic crystal laser," *App. Phys. Lett.*, vol. 81, pp. 2680–2682, 2002.

[27] M. Imada, S. Noda, A. Chutinan, T. Tokuda, M. Murata, and G. Sasaki, "Coherent two-dimensional lasing action in surface-emitting laser with triangular-lattice photonic crystal structure," *Appl. Phys. Lett.*, vol. 75, p. 316318, 1999.

[28] H.-G. Park, S.-H. Kim, S.-H. Kwon, Y.-G. Ju, J.-K. Yang, J.-H. Baek, S.-B. Kim, and Y.-H. Lee, "Electrically driven single-cell photonic crystal laser," *Jour. Quantum Elec.*, vol. 305, pp. 1444–1447, 2004.

[29] H.-G. Park, S.-H. Kim, M.-K. Seo, Y.-G. Ju, S.-B. Kim, and Y.-H. Lee, "Characteristics of electrically driven two-dimensional photonic crystal lasers," *Jour. Quantum Elec.*, vol. 41, pp. 1131–1141, September 2005.

[30] A. Shinya, S. Mitsugi, E. Kuramochi, and M. Notomi, "Ultrasmall multi-channel resonant-tunneling filter using mode gap of width-tuned photonic crystal waveguide," *Optics Express*, vol. 13, May 2005.

[31] H. Benisty, D. Labilloy, C. W. C. J. M. Smith, T. F. Krauss, D. Cassagne, A. Béraud, and C. Jouanin, "Radiation losses of waveguide-based two-dimensional photonic crystals: Positive role of the substrate," *App. Phys. Lett*, vol. 76, pp. 532–534, 2000.

[32] R. G. Hadley, "Out-of-plane losses of line-defect photonic crystal waveguides," *Photon. Technol. Lett.*, vol. 14, pp. 642–644, May 2002.

[33] P. Lalanne, "Electromagnetic analysis of photonic crystal waveguides operating above the light cone," *J. Quantum Electron.*, vol. 38, pp. 800–804, July 2002.

[34] B. D'Urso, O. Painter, J. O'Brien, T. Tombrello, A. Yariv, and A. Scherer, "Modal reflectivity in finite-depth 2-d photonic crystal microcavities," *J. Opt. Soc. Amer. B*, vol. 15, p. 1155, 1998.

[35] P. Lalanne, "Out-of-plane losses of two-dimensional photonic crystal waveguides: Electromagnetic analysis," *App. Phys. Lett.*, vol. 89, pp. 1512–1514, January 2001.

[36] H. Benisty, P. Lalanne, S. Olivier, M. Rattier, C. Weisbuch, C. J. M. Smith, T. F. Krauss, C. Jouanin, and D. Cassagne, "Finite-depth and intrinsic losses

in vertically etched two-dimensional photonic crystals," *Opt. Quantum Elec.*, vol. 34, pp. 205–215, 2002.

[37] M. Kafesaki, C. M. Soukoulis, and M. Agio, "Losses and transmission in two-dimensional slab photonic crystals," *App. Phys. Lett.*, vol. 96, pp. 4033–4038, 2004.

[38] T. Ferrini, B. Lombardet, B. Wild, R. Houdré, and G.-H. Duan, "Hole depth- and shape-induced radiation losses in two-dimensional photonic crystals," *App. Phys. Lett.*, vol. 82, pp. 1009–1001, February 2003.

[39] T. Ferrini, R. Houdré, H. Benisty, M. Qiu, and J. Moosburger, "Radiation losses in planar photonic crystals: two-dimensional representation of hole depth and shape by an imaginary dielectric constant," *J. Opt. Soc. Am. B.*, vol. 20, pp. 469–478, March 2003.

[40] K. R. Maskaly, W. C. Carter, R. D. Averitt, and J. L. Maxwell, "The effect of interfacial roughness on the normal incidence bandgap of one-dimensional photonic crystals," *Optics Express*, October 2005.

[41] W. Bogaerts, P. Bienstman, and R. Baets, "Scattering at sidewall roughness in photonic crystal slabs," *Opt. Lett.*, vol. 28, pp. 689–691, May 2003.

[42] S. Olivier, H. Benisty, C. Weisbuch, C. Smith, T. F. Krauss, and R. Houdré, "Coupled-mode theory and propagation losses in photonic crystal waveguides," *Opt. Express*, vol. 11, p. 1490, 2003.

[43] T. D. Happ, A. Markard, M. Kamp, A. Forchel, S. Anand, J.-L. Gentner, and N. Bouadma, "Nanofabrication of two-dimensional photonic crystal mirrors for 1.5 mm short cavity lasers," *J. Vac. Sci. Technol. B*, vol. 19, pp. 2775–2778, Nov/Dec 2001.

[44] J. Mossburger, M. Kamp, A. Forchel, R. Ferrini, D. Leuenberger, R. Houdré, S. Anand, and J. Berggren, "Nanofabrication of high quality photonic crystals for integrated optics circuits," *Nanotechnology*, vol. 13, pp. 341–345, 2002.

[45] J. Zimmermann, H. Scherer, M. Kamp, S. Deubert, J. P. Reithmaier, A. Forchel, R. März, and S. Anand, "Photonic crystal waveguides with propagation losses in the 1db/mm range," *J. Vac. Sci. Technol. B*, vol. 22, pp. 3356–3358, Nov/Dec 2004.

[46] M. Mulot, S. Anand, R. Ferrini, B. Wild, R. Houdré, J. Moosburger, and A. Forchel, "Fabrication of two-dimensional InP-based photonic crystals by chlorine based chemically assisted ion beam etching," *J. Vac. Sci. Technol. B*, vol. 22, no. 2, 2004.

[47] M. V. Kotlyar, T. Karle, M. D. Settle, L. O. Faolain, and T. F. Krauss, "Low-loss photonic crystal defect waveguides in InP," *App. Phys. Lett.*, vol. 84, May 2004.

[48] R. Ferrini, B.Lombardet, B. Wild, R. Houdré, S. Olivier, H. Benisty, A. Doudji, L. Legouézigou, S. Hubert, S. Sainson, J.-P. Chandouineau, S. Fabre, F. Pommereau, and G.-H. Duan, "Optical characterization of 2D

InP-based photonic crystals fabricated by inductively coupled plasma etching," *Elect. Lett.*, vol. 38, pp. 962–964, August 2002.

[49] F. Pommereau, L. Legouézigou, S. Hubert, S. Sainson, J.-P. Chandouineau, S. Fabre, , G.-H. Duana, B. Lombardet, R. Ferrini, and R. Houdre, "Fabrication of low loss two-dimensional InP photonic crystals by inductively coupled plasma etching," *J. App. Phys.*, vol. 95, pp. 2242–2245, March 2004.

[50] A. Berrier, L. A. Dunbar, R. Houdr, M. Mulot, S. Anand, S. de Rossi, and A. Talneau, "Minimization of out-of-plane losses in planar photonic crystals by optimizing the vertical waveguide," *App. Phys. Lett.*, vol. 85, pp. 3998–4000, November 2004.

[51] M. L. Mašanović, V. Lal, J. A. Summers, J. S. Barton, E. J. Skogen, L. G. Rau, L. A. Coldren, and D. J. Blumenthal, "Widely-tunable monolithically-integrated all-optical wavelength converters in InP," *J. Lightwave Technol.*, vol. 23, pp. 1350–63, 2005.

[52] W. Kuang, C. Kim, A. Stapleton, W. J. Kim, and J. D. OBrien, "Calculated out-of-plane transmission loss for photonic-crystal slab waveguides," *Opt. Lett.*, vol. 28, pp. 1731–1783, 2003.

[53] M. Qiu, "Effective index method for heterostructure-slab-waveguide-based two-dimensional photonic crystals," *App. Phys. Lett.*, vol. 81, pp. 1163–1165, 2002.

[54] M. Davanço, A. Xing, J. Raring, E. L. Hu, and D. J. Blumenthal, "Detailed characterization of slow and dispersive propagation near a mini-stop-band of an InP photonic crystal waveguide," *Opt. Express*, vol. 13, pp. 4931–4938, 2005.

[55] J. O'Brien, O.Painter, R. Lee, C. C. Cheng, A. Yariv, and A. Scherer, "Lasers incoporatig 2D photonic bandgap mirrors," *Elect. Lett.*, vol. 32, pp. 2243–2244, November 1996.

[56] T. D. Happ, A. Markard, M. Kamp, J.-L. Gentner, and A. Forchel, "Short cavity InP-lasers with 2D photonic crystal mirrors," *IEE Proc.-Optoelecton.*, vol. 148, pp. 183–187, August 2001.

[57] S. Mahnkopf, H. Hsin, G.-H. Duan, F. Lelarge, T. Happ, M. Kamp, R.März, and A. Forchel, "Wavelength switching by mode interference between longitudinally coupled photonic crystal channel waveguides," *Elect. Lett*, vol. 40, pp. 29–30, January 2004.

Chapter 2

Photonic Crystal Background Theory

2.1 Introduction

In this chapter, basic aspects of Photonic Crystal (PC) theory related to this thesis investigation are presented. Focus is given only to the relevant information necessary for the understanding of the material presented in the following chapters. The more general aspects of the PC topic can be found in a good number of published books and articles [1, 2, 3, 4].

Photonic Crystal theory is mainly based on the study of Bloch-mode band-structures, obtained from the solution of the electromagnetic field wave equations presented in Section 2.2. Propagation can actually be understood from the existence of Bloch-modes within specific frequency ranges and their dispersive characteristics, which can be assessed through calculation of the Bloch-mode group velocities.

The band-structures studied in this work were obtained with the MIT Photonic Bands program [5], which is based on the Plane-Wave Expansion (PWE) method

described in Section 2.3; Section 3.2.4 shows a glimpse of the correlation between calculated band structures and PC power transmission.

The structures fabricated and characterized in the present work are quasi-2D, in the sense that they they present crystal periodicity on a given 2D plane, however not in the remaining dimension of 3D space. The treatment of such crystals as effective 2D structures is finally explained in Section 2.5.

2.2 Photonic Crystal Band-Structure

Following the established analogy between electronic wavepackets in periodic potentials and optical waves in media with periodic refractive index distribution, wave propagation in PCs can be equally understood from the study of Bloch modes in infinite crystal structures. In an *ab-initio* approach [2], one may start from the time-harmonic Maxwell's equations in differential form for linear isotropic dielectric media, considering spatially periodic dielectric constants, and arrive at the magnetic field vector wave-equation

$$\nabla \times \frac{1}{\epsilon} \nabla \times \mathbf{H} = \left(\frac{\omega}{c}\right)^2 \mathbf{H}, \tag{2.1}$$

which in summary describes the propagation of electromagnetic waves of frequency ω. In Eq. (2.1), the scalar [1] ϵ describes the PC index distribution. An alternative

[1] Considering isotropic dielectric media. In general media, ϵ is a tensor that causes coupling between the different field components. The birefringence of all materials in the present work is considered to be negligibly small so that ϵ is always considered to be scalar. A more general treatment can be found in [5].

formulation for this uses the electric, rather than magnetic field:

$$\frac{1}{\epsilon}\nabla \times \nabla \times \mathbf{E} = \left(\frac{\omega}{c}\right)^2 \mathbf{E}. \tag{2.2}$$

In the presented form, Eqs. 2.1 and 2.2 constitute eigenvalue problems concerning respectively the operators $\nabla \times \frac{1}{\epsilon}\nabla\times$ and $\frac{1}{\epsilon}\nabla \times \nabla\times$. The former of the two can be shown to be Hermitian under the standard $\mathbb{R}^3$ inner product and thus is generally preferred for numerical calculations.

Considering that the translational symmetry of the medium causes the electromagnetic field to obey the same lattice periodicity [2], an equivalent electromagnetic-wave version of Bloch's theorem may be proved [2, 3], stating that the eigenequations above yield eigenfunctions of the form $\mathbf{H} = \mathbf{H}_\mathbf{k}(\mathbf{r}) \cdot \exp(-i\mathbf{k}\cdot\mathbf{r})$. Clearly, eigenvalues are directly related to the wavenumber $\mathbf{k}$.

Notice that since the operator $\nabla \times \frac{1}{\epsilon}\nabla\times$ is Hermitian, Eq. 2.1 yields a complete set of orthogonal Bloch eigenmodes which completely describe wave propagation in the crystal. This is not true for Eq. 2.1, since the Hamiltonian in this case is not Hermitian. Alternative electric field formulations on the other hand can be developed that yield eigenvalue equations with Hermitian operators. [3].

It must be pointed out that the two wave-equations above are scalable. Defining $\mathbf{r}' = f \cdot \mathbf{r}$, f a scalar, $\nabla = f \cdot \nabla'$, where ∇' is the gradient with respect to r'. Taking Eq. 2.1, the following is then valid:

$$\nabla \times \frac{1}{\epsilon(\mathbf{r}')}\nabla \times \mathbf{H} = f^2 \cdot \nabla' \times \frac{1}{\epsilon(\mathbf{r}')}\nabla' \times \mathbf{H} = \Omega^2\mathbf{H}, \tag{2.3}$$

[2] In mathematical terms, $\mathbf{H}(\mathbf{r} - \mathbf{G}) = \mathbf{H}(\mathbf{r})$, the same being valid for $\mathbf{E}$, where $\mathbf{r}$ is a vector inside the unit-cell and $\mathbf{G}$ is any lattice-translation vector.

Then

$$\nabla' \times \frac{1}{\epsilon(\mathbf{r}')} \nabla' \times \mathbf{H} = \Omega'^2 \mathbf{H}, \tag{2.4}$$

with $\Omega' = f^{-2} \cdot \Omega$, which is the same as Eq. 2.1. As such, scaling the dielectric function simply causes the photonic bands to shift in frequency.

Group Velocity

In periodic structures, the energy velocity of a Bloch wave is numerically equal to its group velocity [1, 3]: $\mathbf{v_g} = \nabla_k \omega$. The expression for the group velocity of a calculated Bloch mode as such can be obtained from the Hellmann-Feynman theorem applied to the eigenvalue equation 2.1 [3]. Consider a normalized eigenvector $|\mathbf{u}_n\rangle$ of the operator $\hat{H} = \nabla \times \epsilon^{-1} \nabla \times$ such that

$$\hat{H} \left| \mathbf{u}_n \right\rangle = \omega_n \cdot \left| \mathbf{u}_n \right\rangle . \tag{2.5}$$

Then, from the Hellmann-Feynman theorem,

$$\nabla_k \omega = \left\langle \mathbf{u}_n \left| \frac{\partial \hat{H}}{\partial k} \right| \mathbf{u}_n \right\rangle . \tag{2.6}$$

In general, the operator $\frac{\partial \hat{H}}{\partial k}$ can be obtained in a straightforward way from the $\hat{H}$ operator, depending upon the Bloch-mode calculation method used.

Wave Equations in Two Dimensions

Solutions of the wave equation in two dimensions can be separated into two complementary cases, Tranverse-Electric (TE) and Transverse-Magnetic (TM), in which respectively electric or magnetic fields have no components in the direction

normal to the photonic crystal plane [3]: consider for instance the crystal plane to coincide with the xz plane in Real space. Waves with $\mathbf{H} = H_y\hat{\mathbf{y}}$ are defined as TE, those with $\mathbf{E} = E_y\hat{\mathbf{y}}$ as TM. In this case, Eqs. 2.1 and 2.2 can be reduced to scalar wave equations on the components normal to the crystal plane, which are considerably simpler to solve:

$$\nabla_{\parallel} \cdot (p \cdot \nabla_{\parallel}\phi) = -q\frac{\omega}{c}^2 \phi, \tag{2.7}$$

Here, $\nabla_{\parallel}$ is the gradient in x and z, $\phi = H_y$, $p = 1/\epsilon$, $q = 1$ in the TE case and $\phi = E_y$, $p = 1$, $q = \epsilon$ in the TM case.

Throughout this work, all studied PC structures are two-dimensional and thus present Bloch modes of either TE or TM polarization; these in general present very diverse propagation characteristics. In the following chapters, for each PC structure investigated, either TE or TM individually or both polarizations are studied. The choice of which polarization to investigate in each case is based on what convenient propagation features are offered. In each particular case, the polarization under study is specified for clarity.

Bloch Modes and Wave Transmission in Finite Systems

Power transmission from finite PC structures can be directly related to the existence of and power coupling to Bloch modes of the corresponding infinite crystal structure. Moreover, the Bloch-mode dispersion characteristics are directly

[3] This is actually a homework problem in many electromagnetic theory textbooks

related to the propagation characteristics of waves in finite crystals [4]. Examples are given in Section 3.2.4 and in the following Chapters of this thesis.

2.3 The Plane-Wave Expansion Method

The factor involving the periodic dielectric constant ϵ in Eq. 2.1 can be expanded in Fourier series in the following way:

$$\frac{1}{\epsilon(\mathbf{r})} = \sum_{\mathbf{G}} \kappa(\mathbf{G}) \exp(i\mathbf{G} \cdot \mathbf{r}), \tag{2.8}$$

where $\mathbf{G}$ are the reciprocal lattice vectors. A Bloch solution of the eigen-equation for a particular $\mathbf{k}$ and band order n is in the form $\mathbf{H}_{\mathbf{k}n} = \mathbf{u}_{\mathbf{k}n}(\mathbf{r}) \cdot \exp(-i\mathbf{k} \cdot \mathbf{r})$, with $\mathbf{u}_{\mathbf{k}n}(\mathbf{r} + \mathbf{G}) = \mathbf{u}_{\mathbf{k}n}(\mathbf{r})$. This last factor may as well be expanded in Fourier series to yield the following expression for the Bloch mode:

$$\mathbf{H}_{\mathbf{k}n} = \sum_{\mathbf{G}} \mathbf{H}_{\mathbf{k}n}(\mathbf{G}) \exp[i(\mathbf{k} + \mathbf{G}) \cdot \mathbf{r}]. \tag{2.9}$$

Replacing Eqs. 2.8 and 2.9 into Eq. 2.1 and matching exponential terms gives the following matrix eigenvalue equation:

$$-\sum_{\mathbf{G}'} \kappa(\mathbf{G} - \mathbf{G}')(\mathbf{k} + \mathbf{G}) \times \{(\mathbf{k} + \mathbf{G}) \times \mathbf{H}_{\mathbf{k}n}(\mathbf{G}')\} = \left(\frac{\omega_{\mathbf{k}n}}{c}\right)^2 \mathbf{H}_{\mathbf{k}n}(\mathbf{G}) \tag{2.10}$$

This equation can be solved for a desired $\mathbf{k}$-vector, yielding a particular set of eigenvalues in each case. A large number of plane-waves (i.e., $\mathbf{G}$' factors) is usually necessary for a good calculation accuracy, which causes the generated matrices to become very large. In general, iterative computational methods are used to solve

[4] A very good article in which the relationship between Bloch-mode phases and transmission characteristics in finite 1D systems is studied in detail is [6].

this type of eigenvalue problems. Notice, on the other hand, that Gauss's law for the magnetic field in a dielectric non-magnetic medium,

$$\nabla \cdot \mathbf{H} = 0, \tag{2.11}$$

when applied to Eq. 2.9, yields the result that $\mathbf{H}_{\mathbf{k}n} \cdot (\mathbf{k} + \mathbf{G}) = 0$. By describing the vector $\mathbf{H}_{\mathbf{k}n}(\mathbf{G})$ in terms of two vectors perpendicular to $(\mathbf{k} + \mathbf{G})$, Eq. 2.9 becomes a regular eigenvalue problem of rank $2N$, with N the number of used plane-waves [5].

The software used for the band-structures calculation took a plane-wave basis function $\mathbf{b}_j = \exp\left(\sum_j m_j \mathbf{G}_j \cdot \mathbf{r}\right)$, with $j = 1, 2, 3$ (for 3D space) and $m_j = -\lceil N_j/2 \rceil + 1, ..., \lfloor N_j/2 \rfloor$, such that the plane-wave expansions of the field and dielectric constant could be readily identified as Discrete Fourier Transforms (DFTs). Computation of the matrix multiplication in 2.10 at each iteration thus followed through the procedure

$$-(\mathbf{k} + \mathbf{G}) \times \mathrm{FFT}^{-1}\{\epsilon^{-1}(\mathbf{r}) \cdot \mathrm{FFT}\{(\mathbf{k} + \mathbf{G}') \times \mathbf{H}_{\mathbf{k}n}(\mathbf{G})\}\} \tag{2.12}$$

With this, any type of dielectric function distribution could be treated in a generalized (without requiring the analytical expansion of ϵ^{-1}) and efficient way. In order to improve convergence, however, the dielectric constant ϵ is replaced by an effective, smooth dielectric constant function. The details of this procedure are beyond the scope of this work, and can be found in [5].

2.4 The 2D Lattice-of-holes Photonic Crystal

A two-dimensional PC can be conveniently realized by defining a periodic array of air holes on a background of refractive index different (and usually much larger) than 1. This system is advantageous in terms of both the theoretical analysis, given the scalar nature of its eigen-equations, and fabrication, which in principle requires not much beyond a good hole-etching process. The crystal-like propagation characteristics, band-gap included, depend on the lattice itself, on the background refractive index n, hole radius r and lattice constant a; since these are 2D systems, propagation can be separated into TE and TM polarizations, as remarked above.

The relative air volume within one crystal unit cell has a strong influence on the achievable band-gaps, as the Bloch eigenfrequencies depend on the field distribution within the cell. The air-filling ratios of course can be varied through the hole radii, however ultimately the crystal lattice itself determines the maximum achievable ratio.

Triangular Lattice

Consider a 2D triangular lattice of air holes of radius r on an a background medium with refractive index $n > 1.0$ depicted in Fig. 2.1. Its lattice vectors can be taken to be $\mathbf{a_1} = (\frac{\sqrt{3}}{2}\hat{\mathbf{x}} + \frac{1}{2}\hat{\mathbf{y}}) \cdot a$ and $\mathbf{a_2} = (\frac{\sqrt{3}}{2}\hat{\mathbf{x}} - \frac{1}{2}\hat{\mathbf{y}}) \cdot a$, with corresponding reciprocal-lattice unit vectors $\mathbf{a_1} = (\frac{1}{\sqrt{3}}\hat{\mathbf{x}} + \hat{\mathbf{y}}) \cdot \frac{2\pi}{a}$ and $\mathbf{a_2} = (\frac{1}{\sqrt{3}}\hat{\mathbf{x}} - \hat{\mathbf{y}}) \cdot \frac{2\pi}{a}$. The first Brillouin zone is hexagonal, aligned with the direct-space crystal lattice

as depicted in the inset of Fig. 2.1; the irreducible Brillouin zone is highlighted within, as well as the high-symmetry points Γ, M and K.

Figure 2.1(b) shows the Bloch-mode band-structures for TE and TM polarizations, calculated with the PWE method [5], where the horizontal axis represents k-vectors on the irreducible Brillouin zone boundary and the vertical axis is the normalized eigenfrequency $a/\lambda = \omega \cdot a/c$. High-symmetry points are indicated in the horizontal axis.

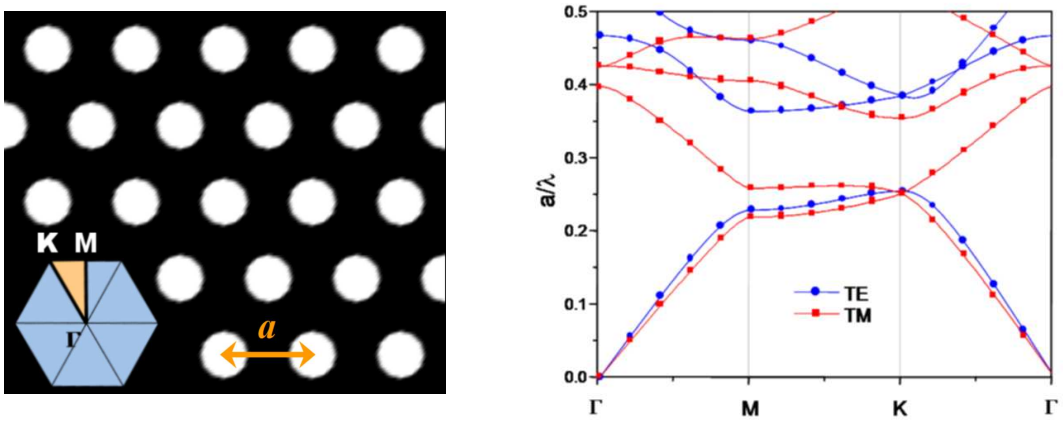

(a) (b)

Figure 2.1: (a) Triangular lattice of air holes photonic crystal and its First Brillouin zone. (b) TE- and TM-polarization band structures.

An omnidirectional band-gap for TE modes is clearly visible in the diagram, between $a/\lambda \approx 0.25$ at the K k-point and $a/\lambda \approx 0.37$ at the M point. Notice that the gap width varies considerably with k-vector. The TM polarization does not present an omnidirectional band-gap, however a small gap is formed at the M-point. The largely different band-structures for TE and TM modes can be understood considering that in the former case the electric field components are on the crystal plane: in order for the electric-field boundary-conditions to be

fulfilled between air and semiconductor regions [5], a fast spatial field variation must be established. In the TM polarization case, the electric field component is continuous everywhere, since it is always perpendicular to the crystal plane, thus always parallel to the air-semiconductor interfaces.

The TE band-gap is very broad: considering the mid-gap to be at $\lambda = 1.55\mu$m (which would require the lattice constant to be $a \approx 0.48\mu$m), the total band-width would exceed 600nm. This is a desirable characteristic for waveguiding, envisioning wave confinement provided by the band-gap over broad wavelength ranges.

Bloch Modes and Wave Transmission in Finite Systems

The incidence of a TE-polarized gaussian beam onto a finite, 10-period PC with the band-structure shown in Fig. 2.1 was simulated using Finite-Differences Time-Domain technique [7]. Incidence in both Γ-M and Γ-K directions of the PC Brillouin Zone were tested, resulting in the transmission amplitude spectra of Fig. 2.2. The grey regions in the amplitude transmission graphs indicate band-gap frequencies at the two high-symmetry points considered. A clear correspondence can be established between transmission stop-bands and the Bloch-modes band-gaps in each direction.

Fringes on the pass-bands are due to Fabry-Pérot-like resonances in the finite PC medium, being intrinsically related to the dispersion characteristics of the Bloch-modes [6].

[5] The electric field component normal to the boundary surface between two different dielectric regions is discontinuous across the interface.

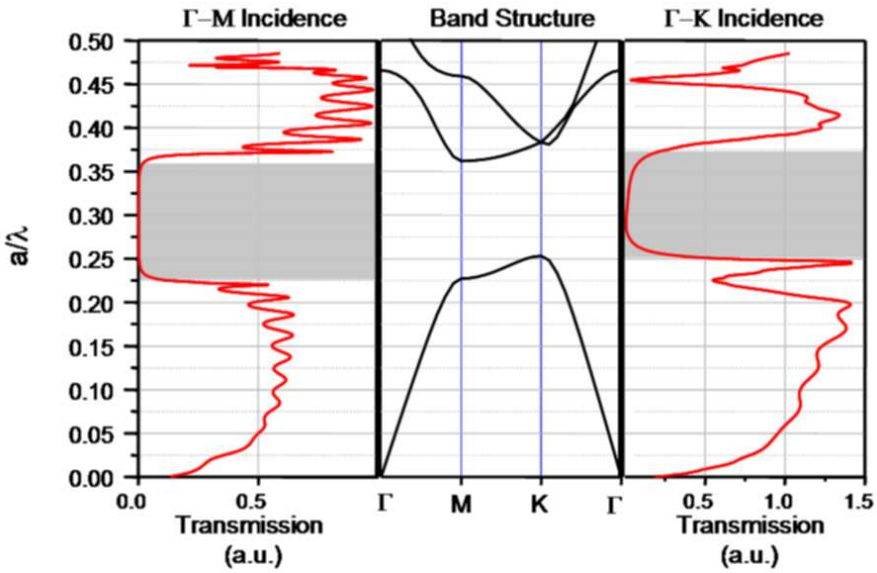

Figure 2.2: Band-structure for the PC in Fig. 2.1 and corresponding field transmission amplitude for incidence in the Γ-M and Γ-K directions of the Brillouin zone. Grey regions in the transmission graphs correspond to the band-gap in the corresponding direction.

2.5 Quasi-2D Photonic Crystal Slabs

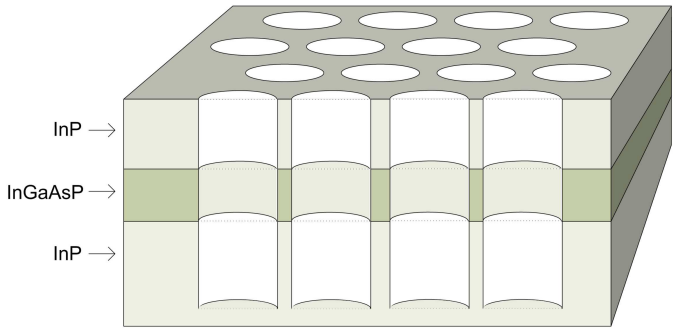

Figure 2.3: Quasi-2D lattice-of-holes PC.

Deeply etched PCs are three-dimensional structures with intrinsically lossy wave propagation due to out-of-crystal-plane radiation [2, 8], however effective two-dimensional crystals have been shown to have very similar Bloch band-struc-

tures, as shown in [9]. In [9], band-structures of 3D weak-confinement PCs were compared to those of equivalent 2D crystals, showing a very close agreement.

Moreover, effective 2D Bloch band-structures have been employed in many instances in the literature (a few good examples are [8, 10, 11]), comparing quite well with experimental results. The advantages of using effective 2D models are the considerably lesser computational effort in band-structure calculations and in computational simulations in general, and the great simplification of the analysis process. The approximation is realized under the assumption that Bloch modes are formed by combinations of bound waves of the slab guide onto which the holes are etched. Good experimental evidence in favor of this assumption has in fact been reported in [12], where a multi-mode slab was used as the background crystal-carrying material. Naturally, the band-structure is obtained considering the background effective index of the unperturbed slab-mode [8, 9, 11].

At the same time, the main reason for out-of-crystal-plane radiation losses has been identified as insufficient hole depth, which should be enough to overlap with the full extent of the pertinent modes of the unperturbed slabs [13, 14, 8, 15]; excessive power leakage toward the substrate may happen otherwise. Substrate leakage could also be linked to coupling between guided and substrate-radiation slab modes due to the introduction of the holes (from the point of view of perturbation theory) which would lead to the inference that hole depth might also influence the band-structure.

From these considerations, effective 2D models are used to analyze photonic crystal waveguides in the following sections, and are assumed to be good approx-

imations to real 3D PC structures with sufficiently deep holes. The experimental sections of this work in general present very good correlation with results obtained from these effective 2D models, offering good evidence for the validity of the above assumption.

Out-of-Crystal-Plane Radiation Losses

Overall, out-of-crystal-plane radiation losses in deeply etched PCs have two contributions. One is intrinsic, linked to the fact that most Bloch modes of the PC are not vertically bound. The second is extrinsic, linked to etched hole imperfections (insufficient depth, sidewall verticality and irregular bottom shapes).

Reference [16] predicts intrinsic radiation losses to scale with the square of the slab index-step, $(\Delta\epsilon)^2$, which means lower radiation leakage for weakly confining structures in leaky-wave propagation regimes. It is important to point out that accurate 3D simulations have shown evidence that the intrinsic radiation losses are not necessarily high and in some cases might even compare to what is found in strongly confining geometries in leaky propagation regimes [17, 18].

Etched hole imperfections such as insufficient depth [13, 14, 8, 15], sidewall verticality [19, 15] and irregular bottom shapes [11, 15] have on the other hand been pointed out as the main sources of out-of-plane radiation losses in real PCs. So far, extrinsic losses reported in the literature were found to be in general one order of magnitude higher than the intrinsic contribution [11, 20]. The main extrinsic loss factor is insufficient hole depth; sidewall tilt has also been predicted to have a very important contribution to radiation losses.

The following section shows the effect of insufficient hole depth on the reflectivity characteristic of a deeply etched PC.

Hole-etch Depth

The effects of insufficient hole etch-depth on PC reflectivity can be observed from a simple Finite-Differences Time-Domain simulation of the deeply etched 1D grating shown in Fig. 2.4(a). This quasi-1D crystal can be designed (by varying the relative air and dielectric section lenghts L_A and L_S [21]) to have a band-gap covering an extremely wide wavelength range. Vertical confinement is provided by a weak multi-layer slab waveguide with modes that extend considerably within the top cladding and substrate regions. Figure 2.4(b) in fact shows the overlap between slab waveguide modes with various top-cladding thicknesses and etched-trenches of varying depths. The horizontal axis corresponds to the position of the trench bottom, with the top of the waveguide starting at position 0. In general, complete overlap is achieved for holes extending about 1μm below the guiding layer. For 1μm top cladding, this would correspond to a $\gtrapprox$ 2-μm-deep trench.

The zero-order TE slab-mode reflectivity for a waveguide with $H_{clad} = 2\mu$m is shown in Fig. 2.5 for different trench depths. The reflectivity is very high within the band-gap ($1.1 \lesssim \lambda/a \lesssim 2.3$) for infinite trenches. Notice that the reflectivity changes little for a 2μm trench depth; in this case, the overall out-of-plane radiation losses are very close to the intrinsic limit for this particular structure. A dramatic reflectivity reduction is on observed for gratings with insufficiently deep trenches ($h_{trench} < 2.0$ in Fig. 2.5). Another important feature are the

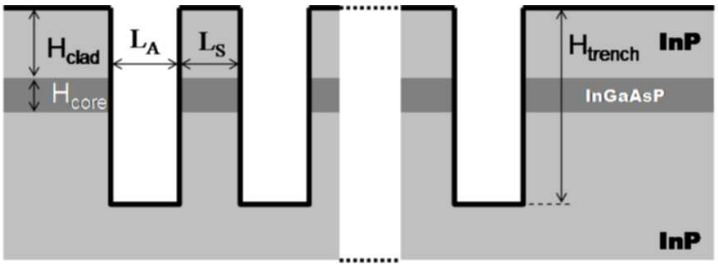

(a)

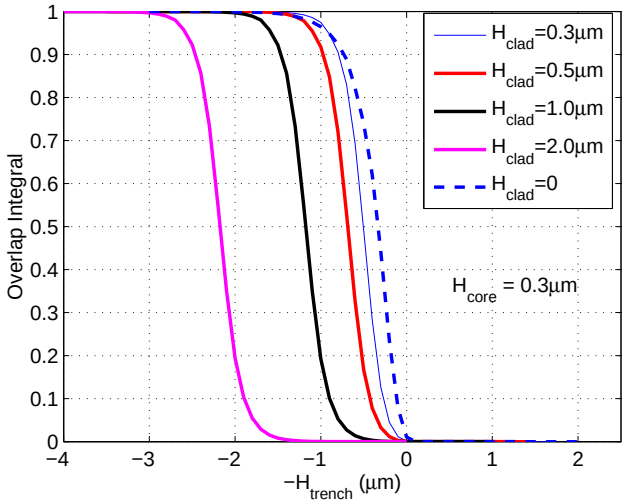

(b)

Figure 2.4: (a) Membrane-type lattice-of-holes PC.(b) Slab-type lattice-of-holes PC.

less-pronounced dips on the right-hand-side of the bandgap as trenches become shallower. The less efficient destructive wave-interference is in this case due to the higher out-of-plane radiation losses into the substrate.

Clearly, trenches should be sufficiently deep for radiation losses to be minimized. It must be pointed out however that the presented results consider only perfectly straight sidewalls. As mentioned above, tilted sidewalls add considerably to the overall radiation losses. This topic has been treated in more detail in [15].

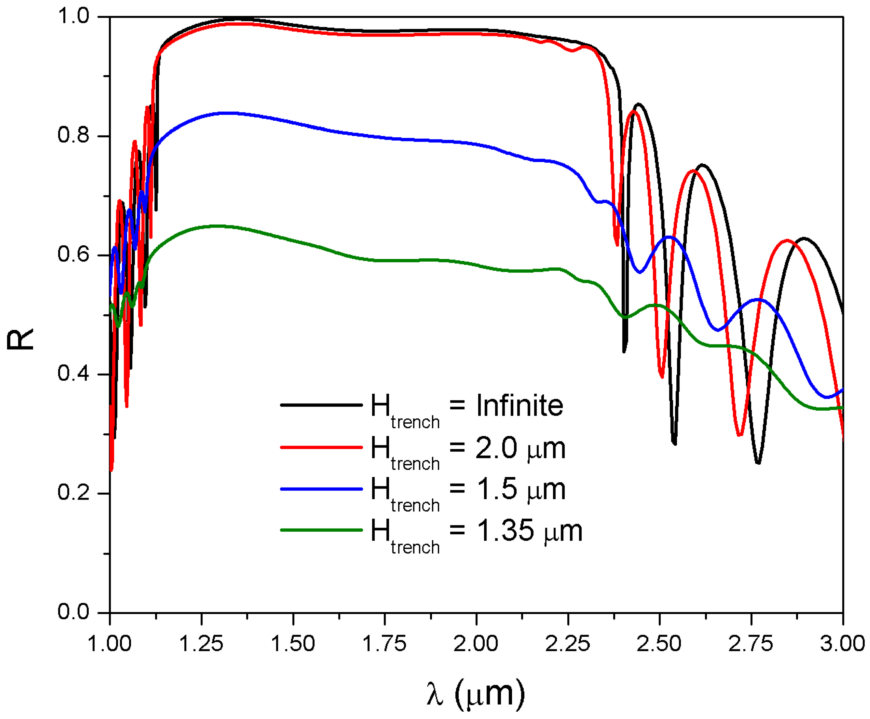

Figure 2.5: Simulated reflectivity from gratings of different trench depths.

2.6 Summary and Conclusions

In this chapter, basic aspects of 2D PC theory were studied, necessary for the understanding of the material that follows.

Quasi-2D slab PCs of the lattice-of-holes type with weak vertical confinement can in general be analyzed through effective 2D PC models, at least as far as the Bloch band-structures are concerned. Band structures yield information about existence and dispersion of Bloch modes within specific frequency ranges, which can be directly correlated to transmission data from the excitation of finite crystals.

It is important to remember that, given the two-dimensional nature of the studied PCs, the electromagnetic field can be described in terms of Bloch modes of two complementary wave polarizations: Transvese-Electric (TE), which has

no electric field components in the direction perpendicular to the crystal plane; Transverse-Magnetic (TM), which has no magnetic field components in the direction normal to the crystal plane. In quasi-2D PCs with weak vertical confinement, TE and TM Bloch modes are assumed to be formed by combinations of TE and TM modes of the weak slab waveguide formed by the epitaxial layer structure respectively. Throughout this work, either polarization or both individually are studied for each PC structure.

The Plane-Wave Expansion (PWE) method, used to calculate PC band structures throughout this thesis, was explained briefly. Although many other methods exist for finding Bloch-type eigenfunctions for the electromagnetic wave equations, the PWE method offers good accuracy and efficiency; additionally, a software based on this scheme was readily available for use [5], which allowed for all presented band structures to be calculated in a straightforward manner.

Out-of-crystal-plane radiation losses, studied in the last section of this chapter, are the main factor limiting the performance of PC structures. Most Bloch modes of PC slabs with weak vertical confinement are intrinsically lossy. These losses have however been predicted to be quite low; losses due to imperfections such as insufficient etch depth, sidewall tilt and conical bottoms on the other hand are much very significant and in fact have a direct impact on the performance of PC structures such as waveguides, cavities and mirrors. In summary, holes with sufficient depth and straight enough sidewalls are required for the minimization of out-of-plane radiation losses, which ultimately imposes very stringent requirements on PC etching techniques.

References

[1] P. Yeh, *Optical Waves in Layered Media*. New York: Wiley-Interscience, 1988.

[2] J. D. Joannopoulos, R. D. Meade, and J. N. Winn, *Photonic Crystals: Molding the Flow of Light*. Princeton, N.J.: Princeton, 1995.

[3] K. Sakoda, *Optical Properties of Photonic Crystals*. Berlin Heidelberg: Springer-Verlag, 2001.

[4] S. G. Johnson and J. D. Joannopoulos, *Photonic Crystals: The Road from Theory to Practice*. Berlin Heidelberg: Springer-Verlag, 2002.

[5] S. G. Johnson and J. D. Joannopoulos, "Block-iterative frequency-domain methods for Maxwell's equations in a planewave basis," *Opt. Express*, vol. 8, no. 3, pp. 173–190, 2001.

[6] J. M. Bendickson, J. P. Dowling, and M. Scalora, "Analytic expressions for the electromagnetic mode density in finite, one-dimensional photonic band-gap structures," *Phys. Rev. E*, vol. 53, pp. 4107–4121, 1994.

[7] A. Taflove, *Computational Electrodynamics - The finite-difference time-domain method, 2nd edition.* Norwood, Massachussets: Artech House, 2000.

[8] H. Benisty, P. Lalanne, S. Olivier, M. Rattier, C. Weisbuch, C. J. M. Smith, T. F. Krauss, C. Jouanin, and D. Cassagne, "Finite-depth and intrinsic losses in vertically etched two-dimensional photonic crystals," *Opt. Quantum Elec.*, vol. 34, pp. 205–215, 2002.

[9] M. Qiu, "Effective index method for heterostructure-slab-waveguide-based two-dimensional photonic crystals," *App. Phys. Lett.*, vol. 81, pp. 1163–1165, 2002.

[10] M. Davanço, A. Xing, J. Raring, E. L. Hu, and D. J. Blumenthal, "Detailed characterization of slow and dispersive propagation near a mini-stop-band of an InP photonic crystal waveguide," *Opt. Express*, vol. 13, pp. 4931–4938, 2005.

[11] T. Ferrini, R. Houdré, H. Benisty, M. Qiu, and J. Moosburger, "Radiation losses in planar photonic crystals: two-dimensional representation of hole depth and shape by an imaginary dielectric constant," *J. Opt. Soc. Am. B.*, vol. 20, pp. 469–478, March 2003.

[12] A. David, C. Meier, R. Sharma, F. S. Diana, S. P. DenBaars, E. Hu, S. Nakamura, C. Weisbuch, and H. Benisty, "Photonic bands in two-dimensionally patterned multimode GaN waveguides for light extraction," *Appl. Phys. Lett.*, vol. 87, pp. 101107:1–3, 2005.

[13] B. D'Urso, O. Painter, J. O'Brien, T. Tombrello, A. Yariv, and A. Scherer, "Modal reflectivity in finite-depth 2-d photonic crystal microcavities," *J. Opt. Soc. Amer. B*, vol. 15, p. 1155, 1998.

[14] P. Lalanne, "Out-of-plane losses of two-dimensional photonic crystal waveguides: Electromagnetic analysis," *App. Phys. Lett.*, vol. 89, pp. 1512–1514, January 2001.

[15] M. Kafesaki, C. M. Soukoulis, and M. Agio, "Losses and transmission in two-dimensional slab photonic crystals," *App. Phys. Lett.*, vol. 96, pp. 4033–4038, 2004.

[16] H. Benisty, D. Labilloy, C. W. C. J. M. Smith, T. F. Krauss, D. Cassagne, A. Béraud, and C. Jouanin, "Radiation losses of waveguide-based two-dimensional photonic crystals: Positive role of the substrate," *App. Phys. Lett*, vol. 76, pp. 532–534, 2000.

[17] R. G. Hadley, "Out-of-plane losses of line-defect photonic crystal waveguides," *Photon. Technol. Lett.*, vol. 14, pp. 642–644, May 2002.

[18] P. Lalanne, "Electromagnetic analysis of photonic crystal waveguides operating above the light cone," *J. Quantum Electron.*, vol. 38, pp. 800–804, July 2002.

[19] T. Ferrini, B. Lombardet, B. Wild, R. Houdré, and G.-H. Duan, "Hole depth- and shape-induced radiation losses in two-dimensional photonic crystals," *App. Phys. Lett.*, vol. 82, pp. 1009–1001, February 2003.

[20] F. Pommereau, L. Legouézigou, S. Hubert, S. Sainson, J.-P. Chandouineau, S. Fabre, , G.-H. Duana, B. Lombardet, R. Ferrini, and R. Houdre, "Fabrication of low loss two-dimensional InP photonic crystals by inductively coupled plasma etching," *J. App. Phys.*, vol. 95, pp. 2242–2245, March 2004.

[21] M. Davanço and D. J. Blumenthal, "Design of an inp-based deeply etched waveguide grating for the implementation of entire c- or l-band rejection filters," *2004 IEEE LEOS Annual Meeting Conference Proceedings*, vol. 1, 2004.

Chapter 3

Photonic Crystal Line-Defect Waveguides

3.1 Introduction

The name *line-defect* waveguide comes from an analogy to the concept of electronic defect-modes in solid-state physics. A line-defect waveguide is formed by suppression of one or more rows of holes of a bulk PC in a given direction, which creates a defect in the crystalline lattice. The resulting channel is expected to have propagating modes within the bulk crystal photonic band-gap frequency range, with lateral confinement provided by the crystal walls. Fig. 3.1(a) shows a triangular lattice-of-holes crystal and its Brillouin zone; Figures 3.1(b) and 3.1(c) display two waveguides realized by suppression of three row of holes in the Γ-K and Γ-M directions of the Brillouin zone. It is important to notice that while the lattice periodicity is broken in the direction perpendicular to the waveguide, longitudinal periodicity is maintained. This will cause the coupling of counter-propagating waves and, consequently, the existence of guided-mode band-gaps in the waveguide direction. One of the earliest proposed photonic crystal applications

was the realization of actual *closed* optical *dielectric* waveguides for very high density photonic integration. As opposed to their open counterparts in which total-internal-reflection provides lateral confinement, PC waveguides would rely on the crystal band-gap for guiding light, thus preventing radiative power leakage for all band-gap frequencies, allowing the realization of lossless sharp bends and compact junctions in general [1, 2, 3]. Recent developments have shown however that the performance of many such structures can be impaired by out-of-crystal-plane radiation losses, either intrinsic or caused by fabrication imperfections [4, 5]. At the same time, high-index-contrast strip waveguides[4, 6, 7] have demonstrated very promising waveguiding characteristics for high-density photonic integration.

On the other hand, photonic crystal waveguides can be designed to offer photonic band-gaps that can be conveniently used for the realization of extremely compact integrated optics band-rejection filters. In addition, there is the possibility of slow and highly dispersive propagation at photonic band-edges, [8, 9, 10, 11], which can in principle find use in integrated-optics pulse-shaping applications. This concept has been explored in the past in transmission-mode Fiber Bragg

(a) (b) (c)

Figure 3.1: (a) Triangular lattice-of-holes photonic crystal and its first Brillouin zone. (b) Three-line defect $W3^{(K)}$ PC waveguide. (b) Three-line defect $W3^{(M)}$ PC waveguide.

Gratings (FBG)[12, 13]; the advantages offered by PC waveguides in this context are the availability of large index discontinuities and strong optical confinement, which, as discussed below, may lead to the implementation of very compact devices, as well as more flexibility in the design of integrated optical signal-processing elements.

The following discussion is an attempt to explain the main effects involved in the applications just described, based on photonic crystal theory.

3.2 Photonic Band-structure Analysis

The propagation characteristics of PC waveguides are generally studied by the assessment of their calculated Bloch modes. As discussed in Chapter 2, the existence of Bloch modes and their dispersion characteristics can be directly correlated to transmission or reflection measurements from finite PCs, the same naturally being valid for PC waveguides as well. The considerations from Section 2.5 regarding the intrinsic leaky nature of propagation in quasi-2D PCs and the validity of 2D band-structures for the analysis of these structures for are taken into account in what follows.

3.2.1 Band-structure Calculation

The band-structure calculation for waveguides can be done in a similar fashion to that of bulk Bloch modes. Starting from the vector harmonic wave-equation

$$\nabla \times \frac{1}{\epsilon} \nabla \times \mathbf{H} = \left(\frac{\omega}{c}\right)^2 \mathbf{H} \tag{3.1}$$

in which ϵ describes the PC index distribution, it is possible to find Bloch-type solutions $\mathbf{H} = \mathbf{H_k}(\mathbf{r}) \cdot \exp(-i\mathbf{k} \cdot \mathbf{r})$ and their respective eigenfrequencies for particular k-vectors in the waveguide direction[14]. Solutions of the wave equation in two dimensions can be separated into two polarizations, TE and TM, in which respectively electric or magnetic fields have no components in the direction normal to the crystal plane. In this case, Eq. 3.1 is reduced to a scalar wave equation on the component normal to the crystal plane (H_y in the TE case, E_y in the TM case).

In general, the Plane-Wave Expansion method [15] considers periodic refractive index and field distributions along the two dimensions of the problem. In order to calculate bound modes of a PC waveguide using this method, one must therefore consider a calculation super-cell encompassing the defect region plus enough rows of holes next to it. For a sufficient number of rows of holes between defect regions, bound modes in the individual defect regions will be isolated from each other and will correspond to individual, isolated defect-modes. This concept is illustrated in Fig. 3.2. It is important to notice that, given the intrinsically leaky nature of certain modes in a deeply-etched PC, 3D super-cell calculations would not work properly, since it would be impossible to completely isolate modes from their counterparts in adjacent cells perpendicular to the crystal plane [16].

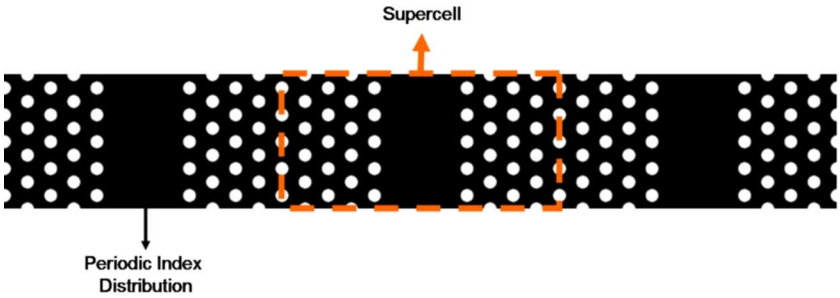

Figure 3.2: Supercell used for calculation of the band-structure of a PC line-defect waveguide.

3.2.2 Band-structure Analysis

Without loss of generality, we next analyze the TE Bloch-mode band-structure of a 2D three-line-defect waveguide in the Γ-K-direction (denominated $W3^{(K)}$, shown in Fig. 3.1(b)), in order to illustrate the various features of guided propagation in line-defect PC waveguides. The band-structure is shown in Fig. 3.3. All depicted propagation bands are for modes with even symmetry with respect to the longitudinal waveguide direction; odd modes are also supported, however these do not add any useful information to the discussion and were thus suppressed.

The band-structure calculation was performed with the Plane-Wave Expansion (PWE) method[15], considering a super-cell with six rows of holes next to the defect region. Modes sought were of the form $u_{\mathbf{k}}(\mathbf{r}) \cdot \exp(-i\mathbf{k} \cdot \mathbf{r})$, with $\mathbf{k}$ pointing in the Γ-K direction in the irreducible Brillouin zone. The background index was considered to be $n_{TE} = 3.26$. Since TE polarization is considered, the scalar Bloch wavefunctions are for the (only) magnetic field component H_y, perpendicular to the crystal plane.

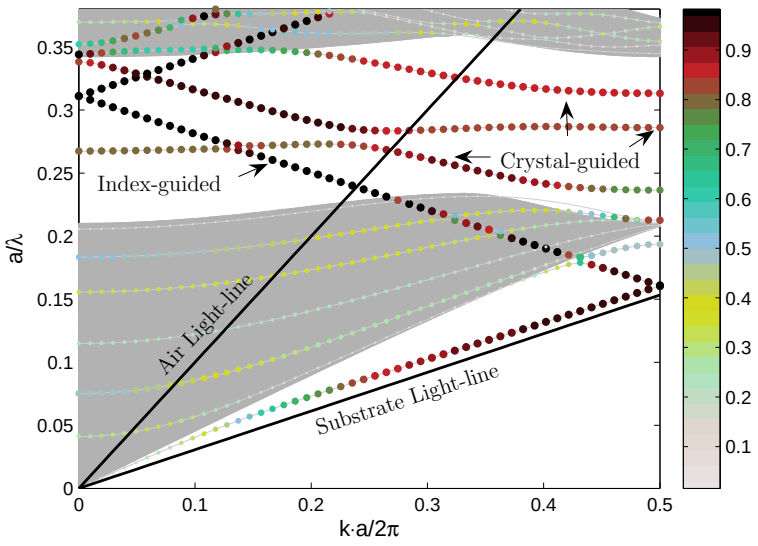

Figure 3.3: Band-structure for a three-line defect waveguide in the $\Gamma - K$ direction, with r/a = 0.35 and n = 3.16. The color-scale corresponds to the magnetic field energy confinement in the defect region.

Mode Confinement

Most modes of the line-defect waveguide structure are perturbed versions of bulk crystal ones and have eigenfrequencies departing slightly from their unperturbed values; the electromagnetic energy is distributed throughout the crystal regions in such cases. At the same time, many modes exist whose fields are localized within the defect regions, and are thus more significant for efficient guided light transmission. In order to discern guided modes from unbound crystal ones in Fig. 3.3, a color scale was created that relates to the magnetic-field energy confinement in the defect region. The confinement is calculated as

$$\Gamma = \frac{\int_{V_{def.}} |\mathbf{H}|^2 dV}{\int_{V_{cell}} |\mathbf{H}|^2 dV}, \tag{3.2}$$

where V_{def} is the volume of the defect region and V_{cell} the computational-cell volume. High confinement values are a good (however not final) indication of a laterally bound mode.

The band-structure of the original bulk PC was plotted as the gray-shaded regions in Fig. 3.3 so waveguide modes could be located with respect to the crystal band-gap. Waveguide modes within the gray areas are at frequencies where bulk-crystal modes exist: assuming that the bands vary smoothly within the Brillouin zone and are bounded by their values at the zone boundaries, all bulk PC modes with k-vector components in the direction of the waveguide will be mapped into the gray regions. It is clear from the figure that the bulk crystal band-gap extends between $a/\lambda \approx 0.225$ and $a/\lambda \approx 0.348$. Although the bulk gap provides useful information about the character of the waveguide modes, it does not provide complete information about lateral confinement.

The Air and Substrate light-lines mark the limits of when the Bloch k-vector in the longitudinal direction becomes larger than the 'free-space' k-vector either in air or in the substrate material. Modes located above these lines are expected to radiate correspondingly into the air or substrate, or both in a real 3D structure[14].

In general, two different types of guiding mechanisms exist in a PC waveguide: crystal-guiding and index-guiding. Confinement in the first case is provided by the high crystal reflectivity at bulk band-gap frequencies; crystal walls act similarly to metallic reflectors, allowing the field to extend very little past the defect region. Previous studies have in fact shown that such crystal-guided modes share many features with those of metallic-waveguide.[17, 18] Examples of crystal-

guided modes are pointed out within the bulk crystal band-gap in Fig. 3.3. In the index-guiding case, a mechanism similar to total-internal reflection takes place, where the crystal regions act as uniform media with effective, average refractive indices. A band of index-guided modes is indicated in Fig. 3.3 starting from $a/\lambda = 0$, becoming better confined at increasing frequencies; confinement higher than 0.7 in fact is achieved at $a/\lambda \approx 0.1$. Similar behavior is observed in regular dielectric waveguides. It is interesting to notice that, as a consequence of the guiding mechanism, index-guided modes remain well-confined even within the bulk dielectric-band range $a/\lambda \approx 0.18$ - $a/\lambda \approx 0.21$.

Field Profiles

Figure 3.4(a) shows a detail of the band-gap region of Fig. 3.3, with three highlighted modes belonging to three distinct bands at $k = 0.186$. Modes *b.* and *c.* are crystal-guided, while *a.* is index-guided. All three have field distributions closely resembling those of the first three even guided modes of a regular closed metallic waveguide, apparent from the amplitude-squared magnetic-field distribution maps shown in Fig. 3.4(b): mode *a.* has a single maximum within the defect; modes *b.* and *c.* respectively three and five maxima. From a different point of view: the magnetic field component changes sign along the defect width zero times in mode *a.* and two and four times respectively in modes *b.* and *c.*. These modes will be henceforth referred as modes of order n, with n being the number of zero-crossings of its magnetic field component. Notice that in the case of even modes such as the ones above, the number of zero-crossings is always even. In

the case of odd modes, this number is equally odd, one of the crossings happening close to the center of defect.

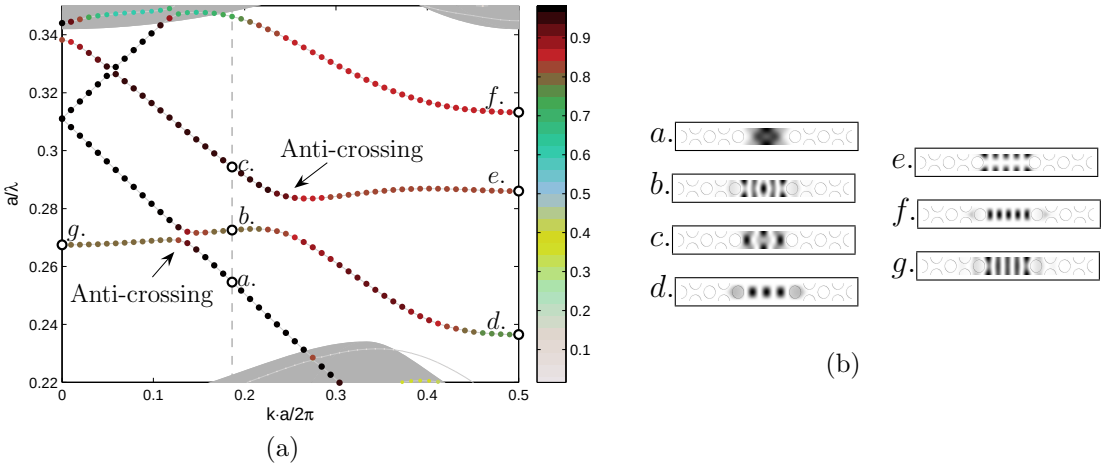

Figure 3.4: (a) Detail of the band-structure shown in Fig. 3.3. (b) Amplitude-squared magnetic field component of the TE-polarized modes *a.*, *b.*, *c.*, *d.*, *e.*, *f.* and *g.* highlighted in (a). The magnetic field is perpendicular to the crystal plane.

Simulations show [10] that preferential excitation of PC modes of a particular order can be achieved through the incidence of matching-order modes of a butt-coupled slab waveguide. From a practical point of view, however, the excitation of high-order modes in slab waveguides presents its own challenges and for this reason coupling to zero-order PC waveguide modes is in general preferable.

The anti-crossings indicated in Fig. 3.4(a) show instances of satisfaction of the Bragg condition between counter-propagating plane-waves in the waveguide direction. This happens however in a way that an anti-crossing can be considered as result of a longitudinal perturbation that couples effective counter-propagating *modes* of different orders [19]. Evidence of this is the fact that modes *d.* and *c.* are of the same order, the same being valid for modes *b.* and *e.* Notice as well

that the band-gap between modes $e.$ and $f.$ at the Brillouin-zone boundary comes from the Bragg condition between modes of the same order.

3.2.3 Slow-Wave Propagation and Mode Coupling

As in Chapter 2, the group velocity of calculated Bloch modes can be obtained from the expression

$$\nabla_k \omega = \left\langle \mathbf{u}_n \left| \frac{\partial \hat{H}}{\partial k} \right| \mathbf{u}_n \right\rangle, \tag{3.3}$$

where $|\mathbf{u}_n\rangle$ is a normalized Bloch mode and $\hat{H}$ is the Hamiltonian of Eq. 3.1. Applied to the zero-order modes at the left-most anti-crossing in Fig. 3.4(a), this expression leads to the group velocity curves in Fig. 3.5. On both sides of the gap, the group velocity tends quickly to zero; the Group Velocity Dispersion (GVD), however, given by $D = -dv_g/d\lambda$, clearly has different signs on each side. This interesting feature, common to all Bloch modes at band anti-crossings, will be explored in more detail in Section 3.3.

It is clear that $v_g = \nabla_k \omega$ tends to zero whenever a band edge is approached. Modes with group velocity tending to zero are henceforth referred to as slow waves. In the band structure of Fig. 3.4(a) -and in fact in the band structure of any line-defect waveguide-, band edges of bound modes can be found either at the anti-crossings or at the Brillouin-zone boundary $k = \pi/a$ or at $k = 0$.

The slow propagation of mode $g.$ in Fig.3.4(a) and nearby modes on the same band falls into the latter case. This phenomenon is very similar to what is observed near mode-cutoff in hollow metallic waveguides, another consequence of the

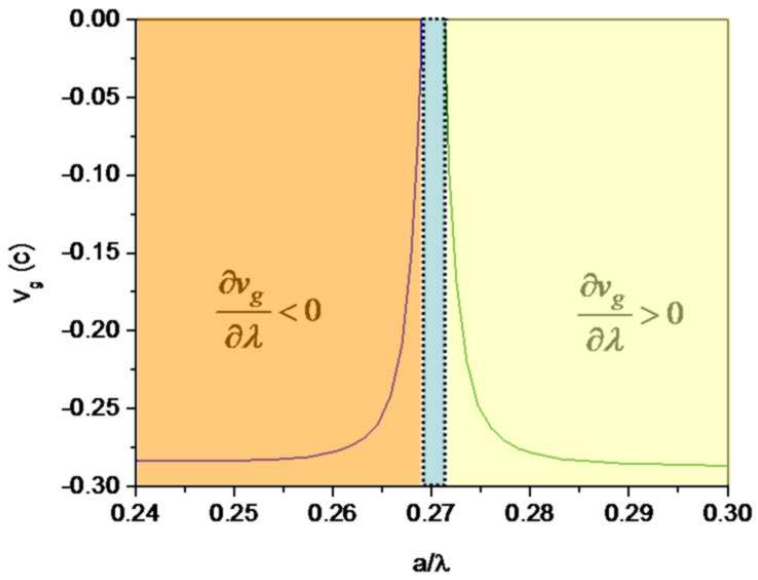

Figure 3.5: Group velocity for zero-order Bloch modes near the left-most anti-crossing in the band-diagram of Fig. 3.4(a).

similarity between crystal-guided and metallic-waveguide modes discussed above. As cutoff is approached in metallic waveguides, the longitudinal component of the propagating guided mode k-vector tends to zero; expansion of the field in plane-wave components reveals that these tend to travel ever more obliquely with respect to the waveguide as cutoff draws near. The field distribution of mode g. in Fig. 3.4(b) presents small longitudinal variations that can be correlated with the small longitudinal travel of its plane-wave components. It is important to notice though that this mechanism is not the only one responsible for slow-wave propagation at $k = 0$, as coupling of counter-propagating waves may also happen at this particular k-vector [20].

Slow wave propagation at band anti-crossings is caused by the coupling between counter-propagating waves, as detailed in what follows. Consider two bands of modes that anti-cross at a certain k-vector in the band diagram. Far away from

the anti-crossing, coupling between plane waves is weak in the longitudinal direction, and coupling in the lateral direction defines order of the guided Bloch modes on both bands. As the anti-crossing is approached, coupling between longitudinal components of the Bloch modes becomes strong resulting from partial satisfaction of the Bragg condition in that direction; at the same time the strong lateral coupling that defines the mode order is maintained and thus propagation near such band-gaps can be reasonably well described by considering the coupling of two effective, unperturbed counter-propagating *straight* waveguide modes, caused by an effective longitudinal waveguide-wall perturbation. Effectively, this constitutes a one-dimensional system that can be described by 1D Coupled-Mode Theory [21, 22], a topic explored in more detail in Section 3.3 below.

It is important to point out that the slow propagation of crystal-guided modes of the same nature as *g*. near $k = 0$ (and far away from any band anti-crossing) does not rely on the mechanism just described; as such the transmission transfer function for light carried by these will be similar to that of a regular (i.e., with no longitudinal variation) waveguide with the dispersion relation displayed in the band-structure. The disadvantage of using this particular set of modes for slow propagation is that they are of higher order and thus demand special schemes for efficient coupling from external ridge waveguides. On the other hand, an indirect use of this crystal-guided band can be realized at its anti-crossing with the index-guided band. This would correspond once again to the effective counter-propagating mode coupling case.

Coupling of Modes of Different Parity

Coupling between effective even and odd counter-propagating modes can be achieved by shifting the waveguide walls in the propagation direction by half lattice constant relative to each other [19, 23]. An example of such waveguides is shown in Fig. 3.6(b), the original structure of which is the $W3^{(K)}$ of Fig. 3.6(a); its band structure is shown in Fig. 3.7(a).

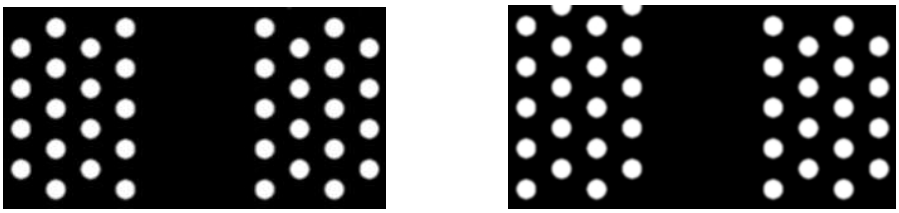

(a) (b)

Figure 3.6: (a) Three-line defect $W3^{(K)}$ PC waveguide. (b) Asymmetric three-line defect $W3^{(K)}$ PC waveguide, formed by shifting the left $W3^{(K)}$ waveguide wall by half lattice constant it the longitudinal waveguide direction.

Here, singled-out Bloch modes with subscript e have even symmetry, while those with subscript o have odd symmetry, as illustrated by the field distributions in Fig. 3.7(a). It is clear that bands include Bloch modes of both even and odd parities and that each anti-crossing involves modes of different parity. An additional interesting feature in the diagram is the existence of mode degeneracies at the Brillouin zone boundary at $k = \pi/a$: due to the absence of coupling, no frequency gap is created between counter-propagating modes at the Brillouin-zone boundary.

The coupling of different-parity modes can be predicted from coupled-mode theory considering a waveguide with periodic sidewall corrugations, the corru-

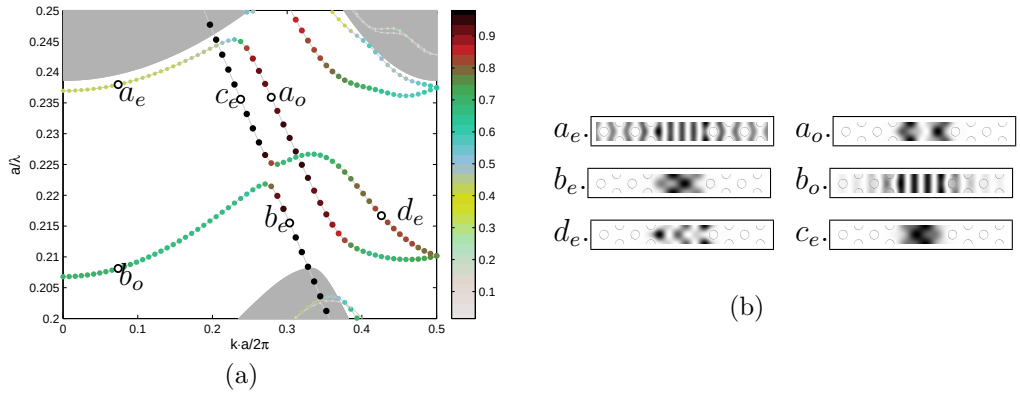

(a) (b)

Figure 3.7: (a) Detail of the band-structure shown in Fig. 3.3. (b) Amplitude-squared magnetic field component of the TE-polarized modes a_e., a_o., b_e., b_o., c_e. and d_e. highlighted in (a). The magnetic field is perpendicular to the crystal plane.

gations on each sidewall being de-phased by half lattice constant. Following the perturbation theory of [24], consider a waveguide extending along the z-direction, providing field confinement in the x-direction. The side-wall corrugation provided by the PC waveguide walls can be assumed equivalent to a periodic perturbation $\Delta\epsilon$ of the dielectric constant in the z-direction [25]:

$$\Delta\epsilon(x,z) = \Delta\epsilon(x)\sum_{-\infty}^{+\infty} a_m e^{i(2m\pi z/\Lambda)} \tag{3.4}$$

The coupling between two TE counter-propagating waves p and q of different orders (and therefore different propagation constants β_p and β_q) caused by the n-th z-harmonic above is given by the expression

$$\kappa = a_n \frac{i\omega\epsilon_0}{4}\int_{-\infty}^{+\infty} \Delta\epsilon(x) E_y^{(p)}(x)\cdot E_y^{(q)}(x)dx. \tag{3.5}$$

In this situation $2n\pi/\Lambda \approx \beta_p + \beta_q$. If $\Delta\epsilon(x)$ is an odd function of x, the coupling coefficient κ is null for $E_y^{(p)}(x)$ and $E_y^{(p)}(x)$ of the same parity.

Bandgap Tuning

The position of anti-crossings can be made to depart from an original position by 'fine' tuning of the defect region width [19, 23]. Consider an asymmetric waveguide such shown in Fig. 6.15, derived from a $W3^{(K)}$ waveguide $W3^{(K)}$ waveguide whose walls were longitudinally displaced by $a/2$ with respect to each other and laterally by $2{\cdot}d$ with respect to their original positions. Figures 6.17(b)-6.17(c) show TE band diagrams for different values of d, for $r/a = 0.24$ and a background index $n_{TE} = 3.3$. Values of d used were $0.15 \cdot a_x$, $0.30 \cdot a_x$, $0.50 \cdot a_x$ and $0.8 \cdot a_x$, with $a_x = \sqrt{3} \cdot a/2$.

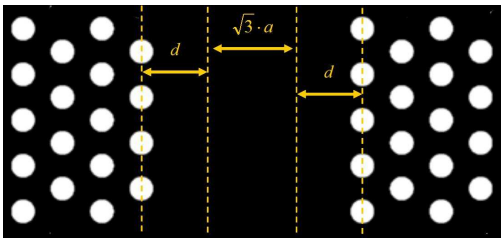

Figure 3.8: Asymmetric waveguide derived from a $W3^{(K)}$ waveguide $W3^{(K)}$ waveguide whose walls were longitudinally displaced by $a/2$ with respect to each other and laterally by $2 \cdot d$ with respect to their original positions.

The original ($d = 0$) waveguide presents an anti-crossing at $a/\lambda \approx 0.221$ between a zero-order (even) and a third-order (odd) band. Increasing the defect width by $d = 0.15 \cdot a_x$ causes the anti-crossing to move to lower frequencies, a trend also followed for $d = 0.30 \cdot a_x$. Notice that the eigenfrequencies at $k = 0$ shift downwards as well; this is similar to what happens to the eigenmode of a metallic waveguide, the cutoff frequencies of which is inversely proportional to the guide width. For $d = 0.5 \cdot a_x$, the band is at low enough frequencies that the anti-crossing is non-existent, having collapsed into the dielectric band. On the

other hand, another anti-crossing forms with a 5th-order band, at $a/\lambda \approx 0.238$. Further increase of the channel width, $d = 0.8 \cdot a_x$, brings this band-gap down to $a/\lambda \approx 0.23$.

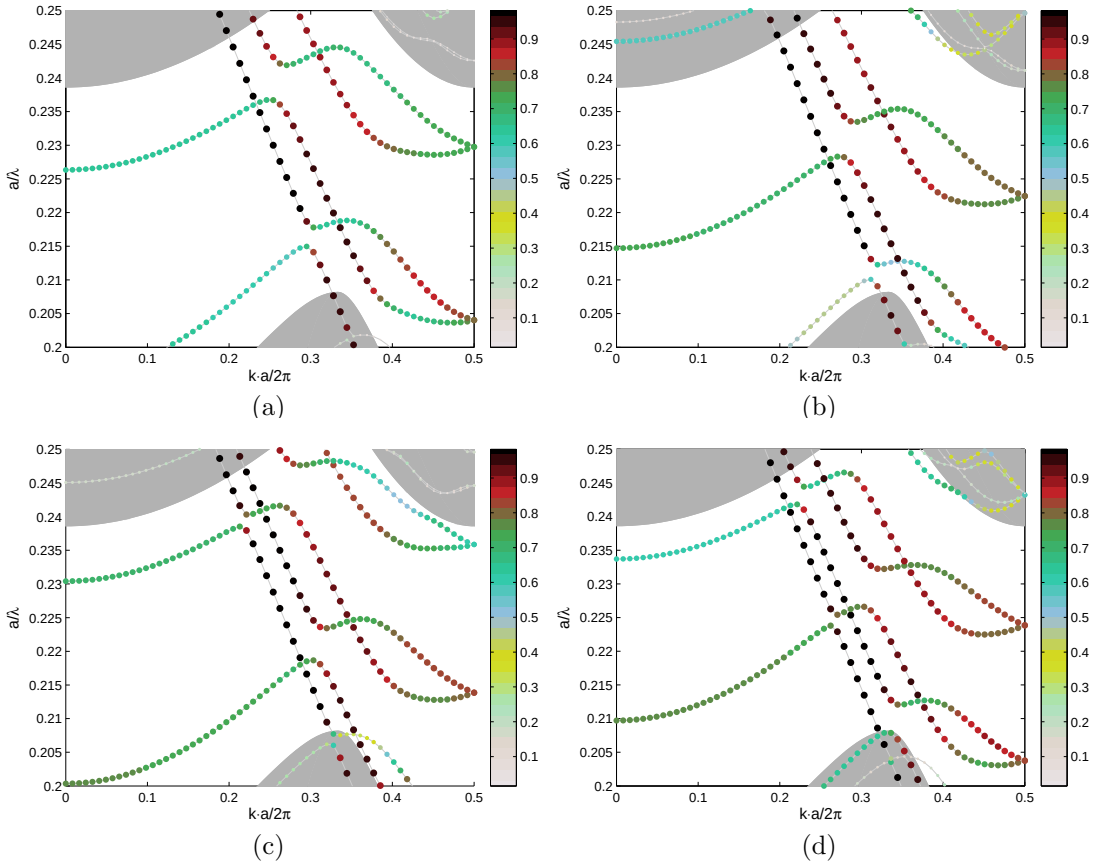

Figure 3.9: Band structures for asymmetric waveguides with (a)$d = 0.15 \cdot a_x$, (b)$d = 0.30 \cdot a_x$, (c)$d = 0.50 \cdot a_x$ and (d)$d = 0.8 \cdot a_x$, with $a_x = \sqrt{3} \cdot a/2$.

An important aspect to be noticed in the band structures is that, as the bands approach the bulk crystal dielectric band, confinement in the defect region tends to decrease. This results from the less efficient reflectivity observed close to bulk waveguide band-edges. Band-gaps appear to become narrower wider channels. This can be understood considering a stronger wave coupling due to the narrower waveguide widths.

A discussion on stop-band position tuning by carrier-injection-induced refractive index changes can be found in the future work section of Chapter 7.

3.2.4 Correlating Band Structure and Transmission Spectra

In the same way as described in Chapter 2, the existence of Bloch modes in infinite PC waveguides can be correlated with transmission spectra of finite structures: power is expected to be carried by Bloch-like waves in a finite PC guide only within the frequency ranges where corresponding Bloch modes exist in the infinite case. In general, band-gaps for guided modes can be readily identified in the transmission spectra, and so can a few fine features such as Fabry-Perot-like resonances. These give clues as to which Bloch-like modes are responsible for power transmission, for which propagation characteristics can be calculated.

A good example of this is displayed in Fig. 3.10, where the TE band-structure (a) of a symmetric $W3^{(K)}$ waveguide is shown next to two transmission spectra, obtained by exciting the guide input with the (c) fundamental and (b) second-order modes of an air-cladding slab waveguide of the same width as the PC guide channel. The spectra were extracted from Finite-Differences Time-Domain simulations of a 48-row waveguide connected to input and output air-cladding slab waveguides as described above. Short Gaussian pulses with the mentioned spatial field profiles were made incident upon the input guide and the power coupled into the same modes was monitored at the output.

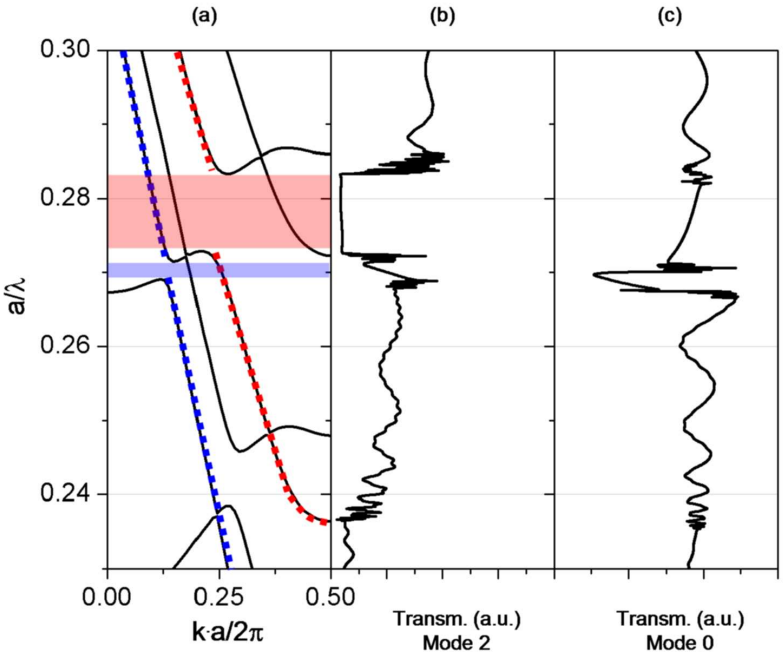

Figure 3.10: (a) Detail of a $W3^{(K)}$ band-structure. Blue dashed lines indicate zero-order bound Bloch modes, red dashed lines correspond to second-order (even) Bloch modes. (b) FDTD-calculated transmitted power for 2nd-order mode excitation. (c) FDTD-calculated transmitted power for zero-order mode excitation.

The 0-order mode excitation will cause most power to couple to the 0-order Bloch-like modes indicated by the blue dashed lines in the band-structure. Features in the spectrum that corroborate this prediction are the small stop-band centered at $a/\lambda = 0.27$ and the fast fringes at its edges. Both features correspond to the small 0-order mode band-gap around the same frequency in the band, indicated by the blue rectangle in the band structure.

Excitation with the 2nd-order mode, by the same token, will tend to cause most power to couple to second-order PC modes, indicated by the dashed red lines in the band structure. A very wide band-gap exists close to $a/\lambda = 0.28$ for such modes, indicated by the red rectangle. This wide gap translates into an

equally wide stop-band in the transmission spectrum. Notice also that the band reaches the Brillouin zone boundary at $a/\lambda \approx 0.235$. This is manifested by the fast fringes in the transmission diagram. Notice that the same fringes also appear in the 0-order mode excitation spectrum. This is because part of the incident power is also coupled into second-order modes.

Further information from the band diagram can be obtained as follows. Figure 3.11(a) shows the group velocity normalized to the velocity of light in vacuum c as a function of a/λ for the 2nd-order PC band. It is evident that the group velocity becomes very small close to the Brillouin-zone limit. Also, it changes very rapidly in the frequency interval $a/\lambda = 0.236 - 0.25$, which translates into a rather large dispersion. Group velocity for the 0th-order PC band is shown in Fig. 3.11(b). For the frequency range $a/\lambda = 0.236 - 0.25$, the group velocity is flat and approximately equal to $0.3 \cdot c$. Almost null dispersion is observed for this band. The band diagram and the group velocities were obtained from a plane-wave expansion-method, using a seven-period super-cell in the lateral direction [15]. This information can be related to the evolution of zero- and second-order mode pulses along the waveguide, which can be obtained from the FDTD simulations described above.

Figures 3.12(a) and 3.12(c) show the time evolution of pulse power at the PC guide input for 0- and 2nd- order mode excitations respectively. Figures 3.12(b) and 3.12(d) show their respective pulse powers at the output waveguide. The carrier of the signal was chosen such that $a/\lambda = 0.237$. As expected for 0-order mode excitation, the pulse at the output shows almost no broadening, since mostly

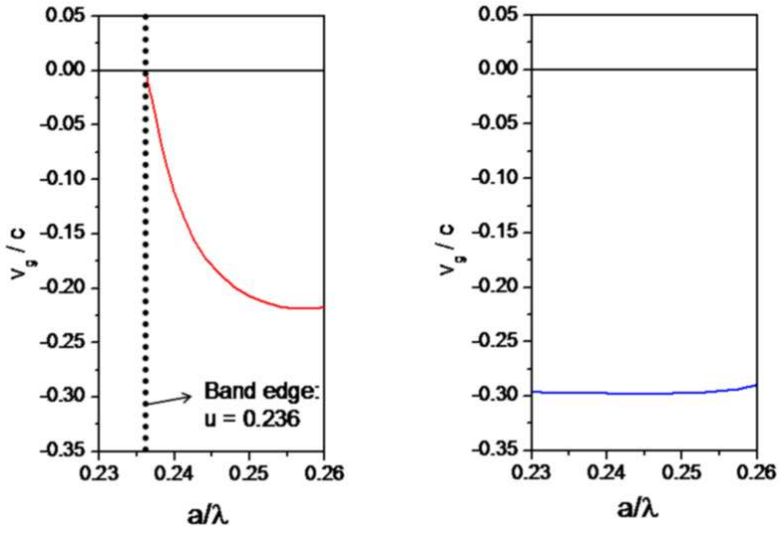

Figure 3.11: (a) Group velocity for the second-order Bloch modes from Fig. 3.10. (b) Group velocity for the zero-order Bloch modes from Fig. 3.10.

modes on the non-dispersive 0th-order band were excited. The delay between input and output traces is about 0.32ps, measured between the maxima. The distance between input and output time-monitors was 28.3μm, leading to a group velocity of approximately $0.29 \cdot c$, as expected. For the 2nd-order mode excitation, the delay between input and output pulses is of about 1.2ps, yielding a group velocity of approximately $0.08 \cdot c$. Also, the output pulse's FHWM is about 3.1 times that of the input: the propagation is extremely dispersive. The small trailing pulse in Fig. 3.12(d) is delayed by the same amount as the pulse in Figure 3.12(b); this is due to partial coupling of the input field into the 0th-order PC band modes. This shows that power can be preferentially coupled to specific PC modes by changing the input field profile, and thus their useful propagation characteristics can be explored. It is important to point out, though, that the peak power for the 2nd-order excitation case is close to only 3% that of the input peak power;

most part of the energy is reflected at the input of the PC guide due to the large mismatch between the group velocities in the slab and in the crystal.

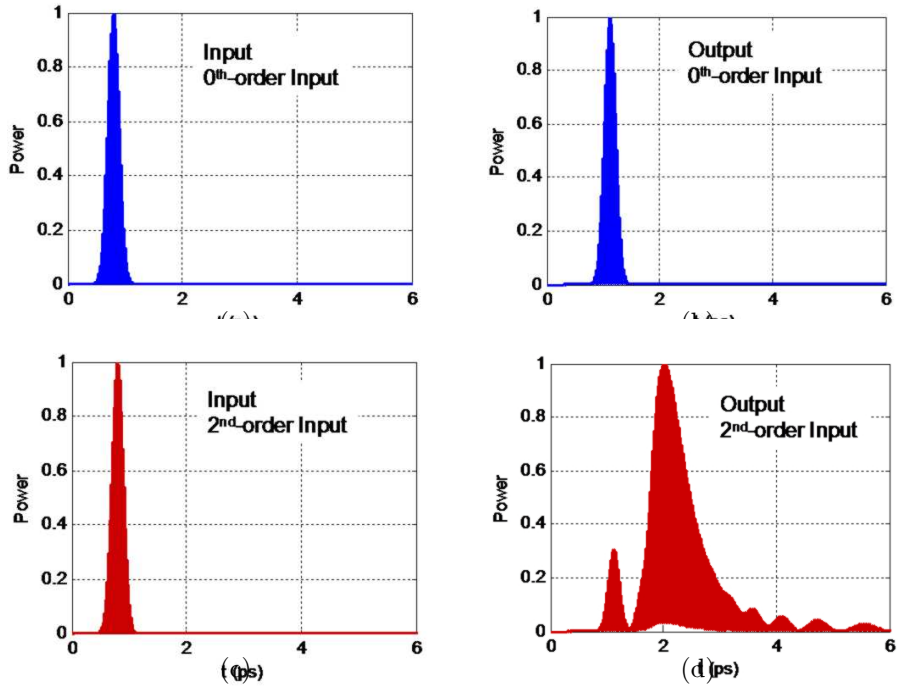

Figure 3.12: FDTD simulation results. (a) Pulse envelope for 0-order slab mode at the PC waveguide input. (b) Output pulse envelope for 0-order mode excitation. (c) Pulse envelope for second-order slab mode at the PC waveguide input. (d) Output pulse envelope for second-order mode excitation.

Notice all of the information obtained above point to the fact that different modes of the PC waveguide can be preferentially excited by proper incidence at the guide input.

3.3 Band-edge Propagation

We now return to the study of the band gap for zero-order modes analyzed in 3.2.3 (displayed again in Fig. 3.13 for convenience). This region is interesting due to the availability of low group velocities and large GVD of opposite signs on

its opposite edges. An additional advantage is that the Bloch modes in question are preferentially excited with a zero-order slab mode at the guide input. Such features are convenient from the point of view of optical signal processing because they would in principle allow 1) longer transmission group delays 2) enhanced GVD and dispersion management capabilities and finally 3) easy coupling to the useful Bloch modes.

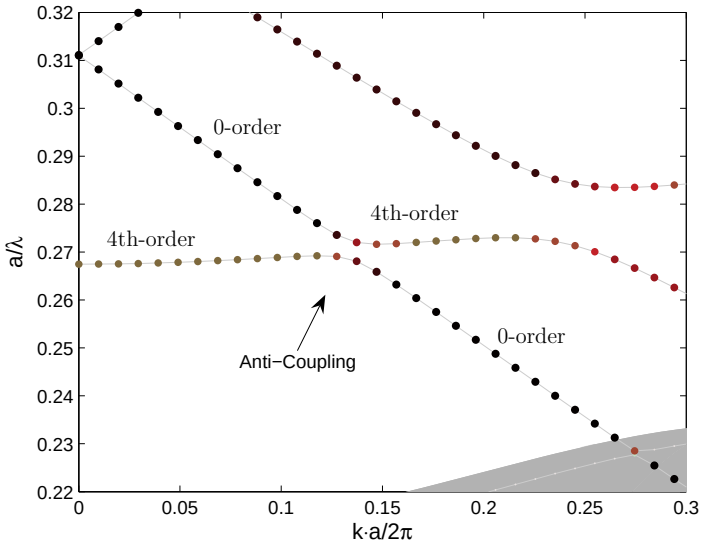

Figure 3.13: Detail of the anti-crossing between 0- and 4th-order modes in the $W3^{(K)}$ band-structure of Fig. 3.4.

The availability of slow propagation and large dispersion can be evaluated with a series of FDTD simulations, in a similar procedure to that of 3.2.4. In the present case, fundamental slab waveguide modes at various wavelengths around the gap are made incident upon the $W3^{(K)}$ input and pulse envelopes at the output are analyzed. The total delay experienced by the pulses are compared to the delay experienced by a pulse traveling through an air-cladding guide of the same length as the PC guide, to yield the curves of *relative* delay shown in Fig. 3.14(a). Input

pulses were chosen to be 1-ps-FWHM Gaussians and the comparison was realized between pulse peaks.

The figure shows that as the band-gap is approached on both sides, pulses experience increasing time-delays with a maximum achieved time-delay of ≈1ps. At the same time, Fig. 3.14(b) shows the broadening suffered by the pulses at each corresponding wavelength. Broadening can be related to two effects: the considerable group-velocity dispersion incurred at the edges, as predicted in Fig. 3.5; and the proximity to band edge, which causes attenuation of part of the pulses' frequency components (i.e. band-gap frequencies). The maximum broadening observed was of $\approx 45\%$ of the $3-dB$ bandwidth, a figure compatible with 20m of standard optical fiber. It is important to notice as well that, far away from the band-gap, the extra delay tends to zero and the pulse is not considerably broadened, as expected.

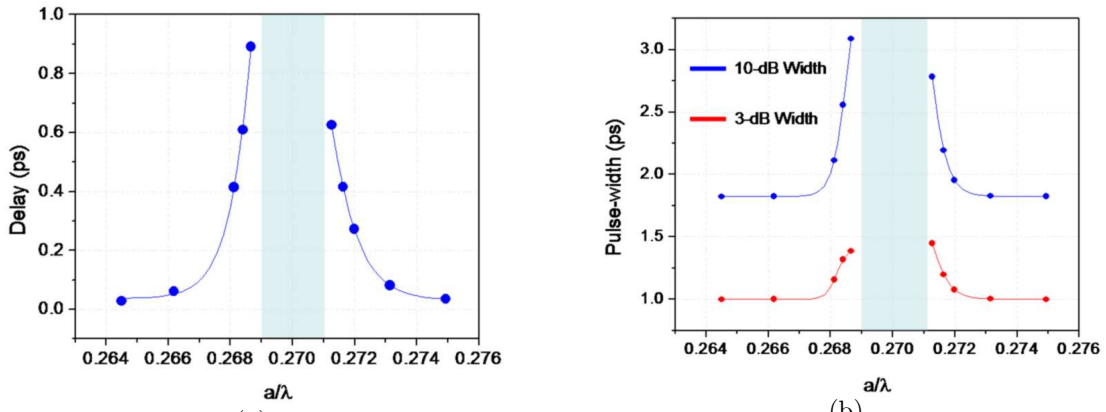

(a) (b)

Figure 3.14: (a) Simulated relative pulse delay as a function of normalized frequency for various input pulse wavelengths close to the band-gap. (b) Corresponding pulse broadening. The blue rectangular region corresponds to the band-gap described in Section 3.2.3.

To show that dispersion plays an important role in pulse broadening, chirped pulses of the format

$$H_y = \phi_0(x) \cdot e^{-\left(\frac{t}{T0}\right)^2} \cdot \sin\left[\omega_0 t + C \cdot \left(\frac{t}{2 \cdot T0}\right)^2\right] \tag{3.6}$$

were launched into the PC waveguide, centered at the wavelengths where maximum broadening was observed on each side of the gap. The chirp parameter C was set to be 0, -5 and +5 at each wavelength. The output pulse envelopes for each case are shown in Fig. 3.15, indicating, as expected, that pulses with opposite chirp signs will be either compressed or broadened complementarily.

Notice that pulse distortion due to dispersion on one of the band-edges can be compensated by propagation on the opposite band-edge, which presents dispersion of opposite sign. One could in principle cascade two waveguides with slightly different lattice constants, such that the signal would be on opposite sides of the band-gap in each guide. Proper design of each section would lead to minimal pulse distortion. This scheme has been explored in Fiber Bragg Gratings (FBGs) in [26].

3.4 Slow-wave Propagation and Coupled-Mode Theory

Inasmuch as FDTD simulations might accurately model pulse propagation in PC waveguides, a better understanding of band-edge slow-wave propagation can be achieved from the introduction of a simplified physical model describing the

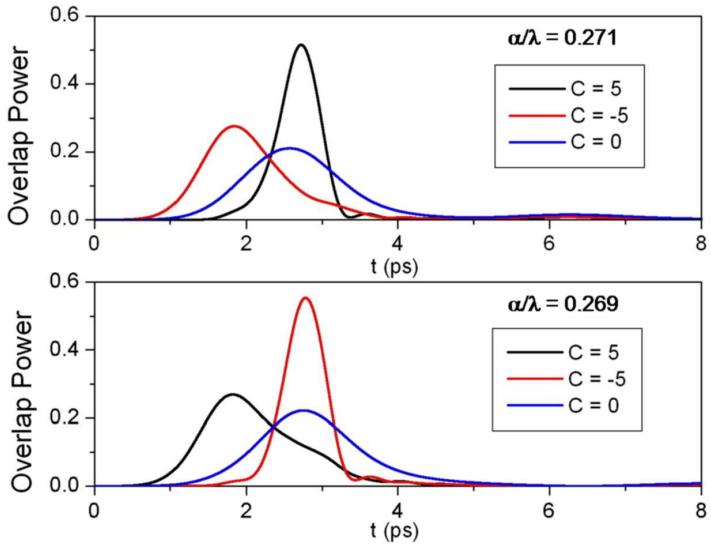

Figure 3.15: Simulated output pulse envelopes at opposite sides of the band-gap for different input pulse chirp parameters C.

underlying physical mechanism. As mentioned in 3.2.3, band-gaps at band anti-crossings such as depicted in Fig. 3.13 can be considered to stem from the coupling of two effective counter-propagating waveguide modes[19, 27, 11], the coupling being provided by an effective longitudinal wall corrugation; from a different angle, propagation near the band-gap edges can be modeled with an effective one-dimensional model, such as developed in Coupled-Mode Theory (CMT)[21, 22]. In its basic form, CMT describes the evolution of an optical mode as it travels along a medium with a longitudinal periodic refractive index perturbation. The periodicity of the perturbation causes coupling between a forward- propagating mode and a backward-propagating counterpart, at frequencies close to where the Bragg condition is satisfied. A transmission stop-band is observed centered at the Bragg frequency, due to a strong energy transfer from the impinging wave into its backward-traveling counterpart. The propagation characteristics of both waves

are clearly dependent on the coupling strength between the two and detuning from the Bragg frequency. CMT predicts the following equations for transmission and reflection coefficients of a finite 1D periodic medium:

$$t = \frac{2\sigma \cdot e^{\delta_- L}}{(\delta_+ + \sigma)\, e^{+\sigma L} - (\delta_+ - \sigma)\, e^{-\sigma L}} \tag{3.7}$$

$$r = \frac{2i|\kappa| \sinh(\sigma L)}{(\delta_+ + \sigma)\, e^{+\sigma L} - (\delta_+ - \sigma)\, e^{-\sigma L}} \tag{3.8}$$

In these equations, which are valid for coupling of waves of different propagation constants, κ is the coupling coefficient, $\delta_\pm = \bar{\alpha}_\pm + i(\bar{\beta}_\pm - \bar{\beta}_{0\pm})$, $\sigma^2 = \kappa^2 + \delta_+^2$, $\bar{\alpha}_\pm = (\alpha_+ \pm \alpha_-)/2$, $\bar{\beta}_\pm = (\beta_+ \pm \beta_-)/2$, $\alpha_\pm$ and $\beta_\pm$ are the loss and propagation constants for forward- and backward-propagating waves and L is the total length. The propagation constants are such that $\beta_\pm = \omega n_\pm / c$, where $n_\pm$ is the phase refractive index of the unperturbed waves. The lateral mode variation is taken into account by the coupling coefficient (this is in fact how the problem is reduced to be one-dimensional) [21, 25, 22]. Notice that propagation losses of any kind (e.g. material absorption and out-of-plane radiation, either intrinsic or caused by hole imperfections in PC guides) can be phenomenologically modelled by the loss parameter. The curves shown in Fig. 3.16, obtained from Eqs. (3.7) and (3.8) with $\beta_\pm = \beta$,$\alpha_\pm = 0$, $\delta_\pm = \delta$, reveal the character of the transmission and reflection transfer functions for lossless band-edge propagation. The gray-shaded region corresponds to the photonic band-gap. The resonances observed in all curves are due to the finiteness of the periodic medium [28]; it is apparent that a maximum group delay is obtained at the first transmission resonance just outside of the band-gap.

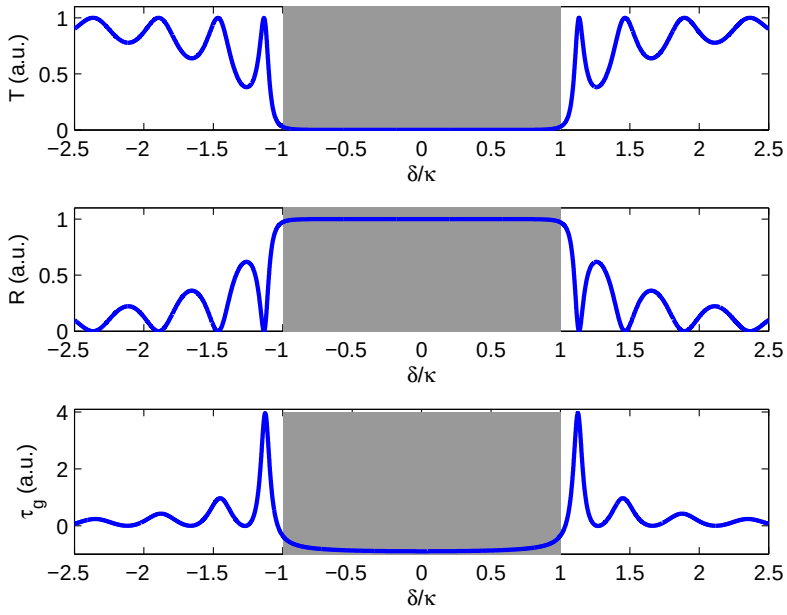

Figure 3.16: Typical transmission, reflection and transmission and group delay characteristics for CMT filter.

The many details of the above filter characteristics have been discussed at length in various publications[12, 29, 13, 28, 26]. The following section covers some of its important aspects.

3.4.1 Pertinent Filter Characteristics

It is convenient to initiate the investigation considering the case when propagation losses are null ($\alpha_{\pm} = 0$). The introduction of losses is detrimental to the maximum group delay, as well as to the sharpness of resonances in the amplitude responses, and thus the lossless case constitutes a best-case. The effect of losses will be treated in a later section.

Transmission

From the preceding discussion, it is expected that the bandwidth of the first resonance outside the gap and the maximum achievable group delay be intimately related to each other. This can be easily realized by examining Eq. 3.7 in the vicinity of $\sigma L = \pi$. The maximum group delay, obtained exactly at this point, is given by

$$\tau_g(\sigma L = \pi) = \eta L \left[2 + \left(\frac{K}{\pi} \right)^2 \right], \tag{3.9}$$

where $\eta = \frac{(n_+ + n_-)}{2c}$ and $K = \kappa L$. At the same time, expanding Eq.3.7 around the first maximum yields:

$$|t(\sigma L \approx \pi)|^2 \approx \frac{1}{1 + \frac{(\omega - \omega_0)^2}{\left[\pi \Big/ \eta K L \sqrt{1 + \left(\frac{K}{\pi}\right)^2} \right]^2}} \tag{3.10}$$

The maximum group delay is seen to increase with $\eta\kappa^2 L^3$, while the bandwidth increases with $(\eta\kappa^2 L^3)^{-1}$. It is important to point out the dependence of both on the phase indices $n_\pm$. These can be quite large for high-order modes close to $k = 0$, as is the case of the 4th-order of Fig. 3.13. The availability of such slow modes is a clear asset offered by PC waveguides. Another important advantage is the large achievable coupling coefficients [11, 27], due to both channel narrowness and large index discontinuities.

Defining BW_{3dB} to be the 3-dB resonance full-width, the following fundamental result is seen to be valid:

$$\lim_{\kappa L \to \infty} BW_{3dB} \times \tau_{g,max} = 2. \tag{3.11}$$

This means that large delays cannot be achieved with large bandwidths; an alternative interpretation is that a pulse will only experience a large delay relative to its width if its spectrum is considerably wider than the filter resonance, distortion thus being unavoidable. This result can be confirmed from Fig. 3.17, where the product in Eq. 3.11 is plotted as a function of κL for BW_{3dB} and τ_{max} obtained from Eq. 3.7, with no approximations. Curves for the 0.7 and 0.9-transmission bandwidths are also shown.

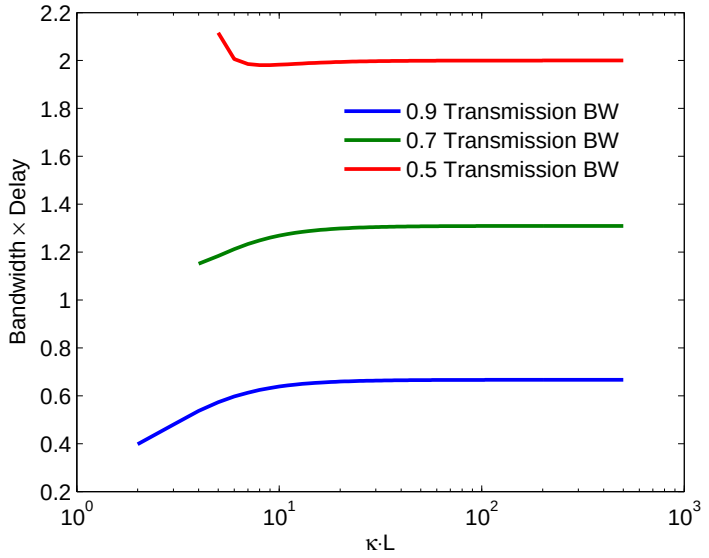

Figure 3.17: Bandwidth-maximum-delay product for the CMT filter as a function of κL. Bandwidths considered were taken at 50%, 70% and 90% of the peak transmissivity.

The fact that GVD has opposite signs on opposite sides of the band-gap can be observed in Fig. 3.18, obtained by taking the derivative of τ_g from Fig. 3.16 with respect to ω. The curve is an odd function of δ that changes sign many times along the frequency axis. Notice that the first zero-crossings outside the band-gap

region correspond to the group delay maxima in Fig. 3.16. In addition, high-order dispersion is not negligible [26].

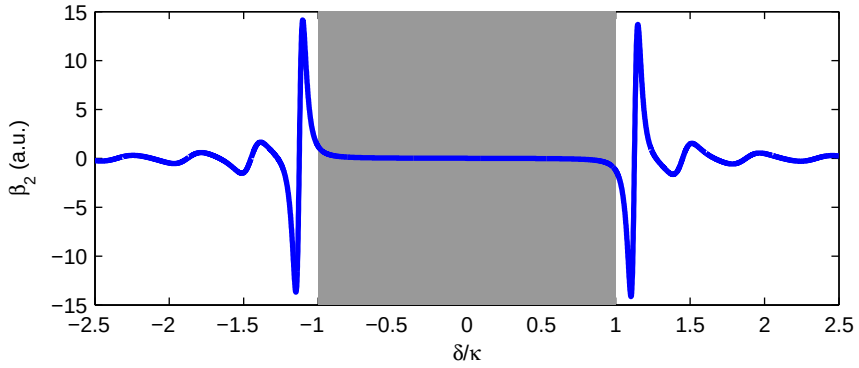

Figure 3.18: GVD coefficient $\beta_2 = d\tau_g/d\omega$ for corresponding to Fig. 3.16. The gray rectangle indicates the band-gap.

Varying the grating period along its length (chirping) and smoothing the coupling coefficient transitions at the grating input and output (apodization) can be used to reduce band-edge resonances; these schemes are in fact widely used in FBGs [30]. Less prominent transmission resonances mean at the same time reduced band-edge reflectivity lobes, as well as lower group delay and dispersion. Clearly, a compromise must be achieved between these filter characteristics. In general, however, low band-edge reflectivity levels, pass-band ripple and dispersion are desired, which are only achieved together with a lower maximum group delay.

Reflectivity

Effectively, a PC waveguide is a distributed-feedback mirror with a (potentially) very large coupling coefficient defined by a narrow channel width and large index discontinuities. It offers, as a result, extremely high reflectivities over very

wide bandwidths for a very small number of periods, or total length. The bandwidth prospect can be inferred from the following expression for the band-gap width, obtained by setting $\delta_+ = \kappa$:

$$\Delta_\pm = \frac{a}{2\pi} \cdot \frac{4\kappa}{n_+ + n_-}. \tag{3.12}$$

The reflectivity consideration can be understood from Eq. 3.8 calculated at the middle of the band-gap,

$$|r(\delta_+ = 0)|^2 = |\tanh(\kappa \cdot L)|^2, \tag{3.13}$$

which tends quickly to 1 as $\kappa \cdot L$ increases. A typical reflectivity spectrum such as in Fig. 3.16 presents a reasonable reflection level even outside of the band-gap, with a series of local reflectivity maxima wherever transmission minima are found.

In photonic integrated circuits with internal sources [31], even small reflected waves in the optical path may cause broadening of the internal laser linewidth, an effect that might lead to performance degradation in systems applications. This constitutes a strong objection to the use of PC waveguides in this context, unless a mechanism to mitigate the distributed-feedback reflected signal is available. One possible alternative when butt-coupling ridge and PC waveguides would be the employment of structures in which backward-propagating modes are of higher order. Mode filters based on waveguide tapering or even Multimode Interference filters [32] could then be used to reduce back-reflected waves to acceptable levels. Experimental evidence showing good prospects for this technique will be explained in Chapter 6.

Effect of Propagation Losses

The deterioration of the maximum group velocity at the band-edges due to propagation losses is a counter-intuitive effect that can nevertheless be linked to the concomitant sharpness degradation of the amplitude-response resonances. This effect is illustrated in Fig. 3.19, where the transmissivity and group delay for a CMT filter with $\beta_{\pm} = \beta$, $\alpha_{\pm} = \alpha$, $\delta_{\pm} = \delta$ and increasing values of $\alpha \cdot L$ are plotted. Enhanced band-edge group delay is a result of wave interference at the waveguide output provided by the distributed-feedback mechanism. The way in which individual wave components of an optical signal are delayed and attenuated is intimately related, given that the system is causal [1]. It is apparent that the introduction of losses causes a less effective wave interference, noted from the smaller amplitude of the band-edge resonances. The connection between amplitude and phase is such that reduced delays are required for the satisfaction the causality condition.

Notice that the transmission stop-band edge slopes also become less sharp with either forward or backward propagation losses. In general, however, higher-order modes tend to have considerably higher losses and thus have a larger influence these slopes.

At the same time, the maximum values of transmissivity and reflectivity change in particular ways depending on $\alpha_{\pm}$. Far away from the bandgap ($|\delta_{+}|^2 >> \kappa^2$), no mode-coupling takes place and as a result $|t|^2 \approx \exp(-\alpha_{+}L)$; the reflectivity

[1] From a digital filter theory point of view, the transfer function 3.7 describes a Minimum Phase Filter (MPF), the amplitude and phase of which are uniquely related and form a Hilbert Transform pair [29, 13].

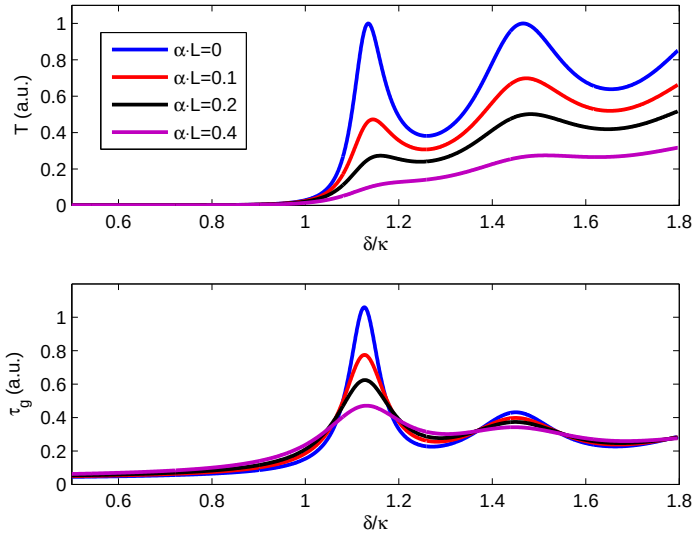

Figure 3.19: Power transmission and group delay curves for varying values of propagation losses.

at the gap center, on the other hand, is

$$|r_{max}|^2 \approx \frac{\kappa \cdot \sinh(\sigma L)}{\bar{\alpha}_+ \cosh(\sigma L) + \sigma \sinh(\sigma L)}, \tag{3.14}$$

with $\sigma^2 = \kappa^2 + \bar{\alpha}_+^2$, clearly depending on $\bar{\alpha}_+$, the average attenuation constant between the forward- and backward-propagating waves.

Propagation losses have thus a significant influence on both transmission and reflection filter characteristics.

3.4.2 Comparison with FDTD

The applicability of the CMT equations for modeling of band-edge propagation has been demonstrated in many experimental articles in the literature [11]. In order to illustrate the accuracy of the CMT approximation, a comparison is next presented between FDTD simulation results and those obtained from Eq. 3.7,

the test consisting simply of launching a 1-ps pulse through the 48-period $W3^{(K)}$ waveguide described in Section 3.3.

The initial step consists in finding appropriate values for the parameters κ and $n_{\pm}$. Following the procedure used in [27], the phase indices $n_{\pm}$ can be taken to be the slopes of the zero- and 4th-order mode bands, taken far enough from the anti-crossing that mode-coupling is minimal, however close enough that no interaction with other bands occurs or band-edges are reached. Under these regimes, the branches are roughly linear, and the Bloch-mode group velocities are related to the phase indices by $v_{g\pm} = c/n_{\pm}$. The coupling coefficients can be obtained from the band-gap width $\Delta_{\pm}$ given by Eq. 3.12.

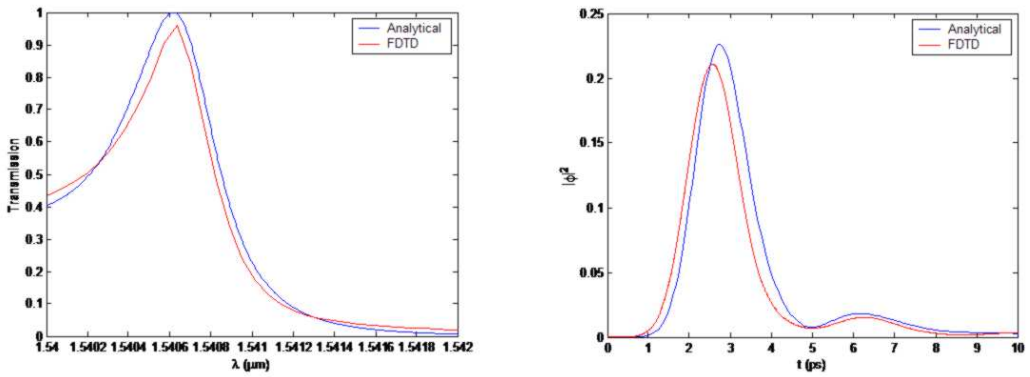

(a) (b)

Figure 3.20: (a) Power transmission spectra obtained from FDTD and CMT. (b) Output pulse envelopes obtained from FDTD and CMT under similar excitation conditions.

Following these guidelines, the band structure in Fig. 3.13 yields $n_{+} \approx 3.4$, $n_{-} \approx 29.0$ and $\kappa \approx 27.95 cm^{-1}$. The total guide length was $L \approx 20 \mu m$ and losses are considered to be null. Figure 3.20(a) shows a detail of the amplitude-squared FDTD- and CMT-calculated transfer functions. The feature displayed

is the first resonance outside of the band-gap on one of the band-edges, where group delay is expected to be maximum; its 3-dB full-width is $\approx 0.5nm$. The matching between the two curves is quite good. Output-pulse envelopes from the

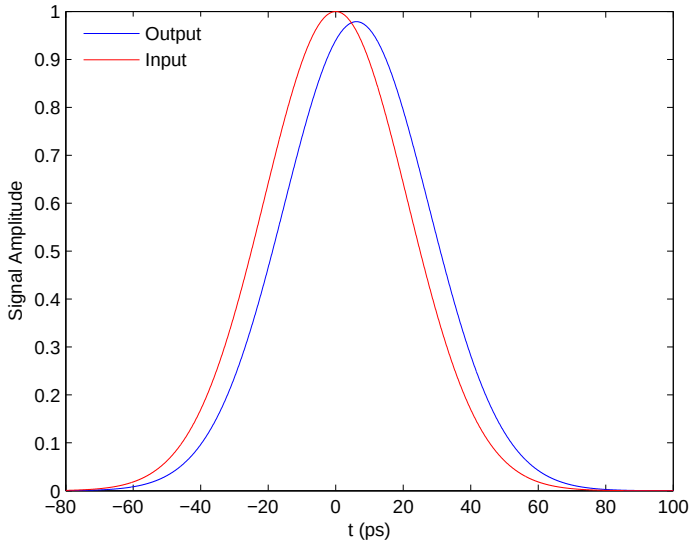

Figure 3.21: Input, 50ps pulse envelope and the corresponding output pulse. The delay between the two is ≈6ps. Curves were obtained from Eq. 3.7.

two methods are shown in Fig. 3.20(b). Input pulses were Gaussian-shaped, with 1ps FWHM, centered at the group-delay maximizing wavelength. Pulses in both cases experienced a delay of ≈2.5ps and suffered very similar distortions. The large distortion observed is mostly due to the very large (≈2nm FWHM) pulse spectral width, as compared to the filter resonance width. A 50-ps-FWHM input pulse, having a much narrower (≈ 0.04nm FWHM) spectrum, is delayed by roughly 6ps, considerably more than in the previous case, suffering much less distortion, as seen in Fig. 3.21. Notice that the experienced delay is very small compared to the pulse FWHM, despite being almost twice that of the 1-ps pulse case. The maximum delays and corresponding transmission bandwidths achievable with the

present waveguide as a function of its length L (i.e., number of crystal periods) are shown in Figures 5.16 and 3.22(b), obtained from the CMT transmission equation. The bandwidth is set to correspond to 90% transmission. The achievable delay at $L \approx 50 \cdot a$ is close to 6ps, as obtained for the narrow-bandwidth pulse above. The bandwidth is seen to decrease dramatically with length, while the maximum delay increases in a related way.

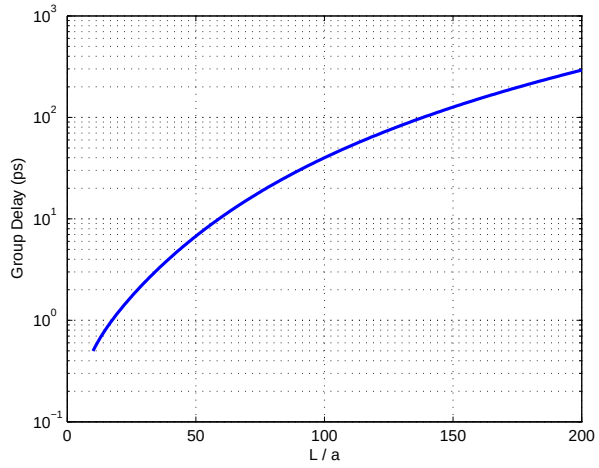

(a)

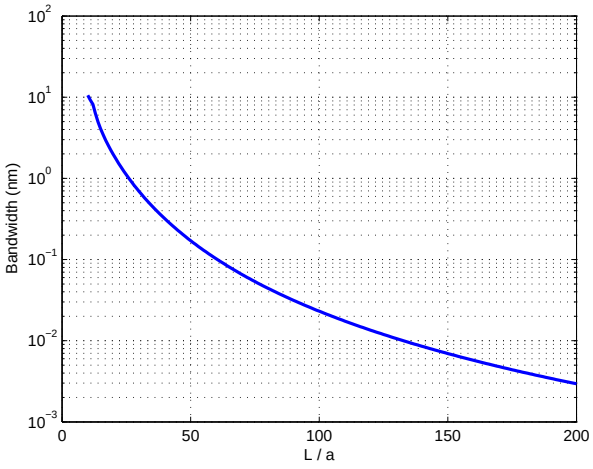

(b)

Figure 3.22: (a) Group delay as function of length. (b) Transmission bandwidth as function of length.

3.5 Summary and Conclusions

In this chapter, relevant theoretical aspects of PC waveguides were covered in detail. The assessment was done based on the analysis of PC waveguide band-structures calculated with the PWE method described in Chapter 2, Finite-Difference Time-Domain (FDTD) simulations and analytic Coupled-Mode Theory (CMT). These three methods of analysis yield three different, almost complementary points of view about propagation in PC structures.

An important notion to retain is the fact that the bulk crystal forming the PC waveguide walls in general presents an omnidirectional band-gap for a given polarization. Creating a linear defect in the bulk crystal (i.e. defining a line-defect waveguide) causes a series of defect-confined modes to appear within the bulk crystal band-gap frequency range. These modes are confined in the defect either due to the band-gap (*crystal-guided modes*) or by total-internal reflection (*index-guided modes*). All band-structures presented in this chapter include a color-scale relative to the field confinement in the defect region. This information is usually absent in most PC waveguide articles in the literature, although it constitutes a very good method for discerning defect-confined and unbound crystal modes.

Defect-confined modes can be categorized, as in regular waveguides, according to the number of zero-crossings experienced by the main field component along the waveguide cross-section. In general, many bands of modes of different orders exist within the bulk crystal band-gap frequency range. Through FDTD simulations, it is shown in the text that preferential excitation of modes of specific orders can be

realized by incidence of standard slab-waveguide modes of corresponding orders at the PC guide input.

The longitudinal waveguide periodicity causes some of the bands to anti-cross, thereby creating small band-gaps for the bands involved. The more interesting propagation characteristics of PC guides are found close to such band-gaps: slow and highly dispersive propagation, which so far seems to be the strongest asset offered by line-defect waveguides, specially considering the high losses found in deeply etched crystals.

Generalized CMT equations for coupling of modes of different orders were theoretically investigated for modelling the propagation around stop-bands formed at anti-crossings of Bloch mode bands. The generalized equations were shown produce very similar results to those obtained from exact FDTD simulations, evidencing the validity of the analytical approximation. The physical mechanism described by CMT is the coupling of counter-propagating one-dimensional waves caused by a periodic perturbation of the propagation medium. The study of the analytical CMT expression is very useful since it leads to a clear understanding of the achievable filter transfer functions.

An assessment of the various parameters influencing the PC waveguide transfer functions was carried out, assuming the validity of the analytical model. The following conclusions were reached regarding band-edge propagation in PC waveguides: the transmission and reflection transfer functions of a finite PC guide at the edges of a band-anti-crossing stop-band present a series of Fabry-Pérot-like resonances related to the finiteness of the structure. A maximum transmission

group delay is found at the first transmission maximum outside of the band-gap; the maximum delay is larger the narrower the bandwidth of the transmission peak, such that fundamentally large delays can never be achieved with large bandwidths. Additionally, large propagation losses are detrimental of the maximum achievable group delay, apart from the power transmission level. In summary, the propagation characteristics close to defect-confined mode band-edges offer limited applicability in terms of integrated delay elements, since bandwidth will always be limited for large group delays. The large band-edge dispersion observed on the other hand is very promising for pulse-shaping applications.

Finally, it must be pointed out that, even though all explanations are related to propagation in a multimode three-line-defect waveguide in a triangular lattice, the phenomena described are common to all types of line-defect guides.

References

[1] A. Mekis, J. C. Chen, I. Kurland, S. Fan, P. R. Villeneuve, and J. D. Joannopoulos, "High transmission through sharp bends in photonic crystal waveguides," *Phys. Rev. Lett.*, vol. 77, p. 3787, 1996.

[2] A. Chutinan and S. Noda, "Waveguides and waveguide bends in two-dimensional photonic crystal slabs," *Phys. Rev. B*, vol. 62, pp. 4488–4492, 2000.

[3] H. Benisty, C. Weisbuch, M. Agio, M. Kafesaki, C. M. Soukoulis, M. Qiu, M. Swillo, A. Karlsson, B. Jaskorzynska, A. Talneau, J. Moosburger, M. Kamp, A. Forchel, R. Ferrini, R. Houdr, and U. Oersterle, "Models and measurements for the transmission of submicron-width waveguide bends defined in 2D photonic crystals," *IEEE J. Quantum Electron.*, vol. 38, pp. 770–785, 2002.

[4] Y. A. Vlasov and S. J. McNab, "Waveguiding in silicon-on-insulator photonic crystal and single-mode strip waveguides," in *IEEE LEOS Annual Meeting Conference Proceedings*, pp. 809–810, 2004.

[5] H. Benisty, P. Lalanne, S. Olivier, M. Rattier, C. Weisbuch, C. J. M. Smith, T. F. Krauss, C. Jouanin, and D. Cassagne, "Finite-depth and intrinsic losses in vertically etched two-dimensional photonic crystals," *Opt. Quantum Elec.*, vol. 34, pp. 205–215, 2002.

[6] S. J. McNab, N. Moll, and Y. A. Vlasov, "Ultra-low loss photonic integrated circuit with membrane-type photonic crystal waveguides," *Opt. Express*, vol. 11, pp. 2927–2939, 2003.

[7] M. A. P. S. Akiyama and, P. T. Rakich, K. Wada, J. Michel, H. A. Haus, E. P. Ippen, and L. C. Kimmerling, "Air trench bends and splitters for dense optical integration in low index contrast," *J. Lightwave Technol.*, vol. 23, pp. 2771–2777, July 2005.

[8] J. Yamauchi, M. Sekiguchi, O. Uchiyama, J. Shibayama, and H. Nakano, "Modified finite-difference formula for the analysis of semivectorial modes in step-index optical waveguides," *Photon. Technol. Lett.*, vol. 9, p. 961, 1997.

[9] H. Gersen, T. J. Karle, R. J. P. Engelen, W. Bogaerts, J. P. Korterik, N. F. van Hulst, T. F. Krauss, and L. Kuipers, "Real-space observation of ultraslow light in photonic crystal waveguides," *Phys. Rev. Lett.*, vol. 94, pp. 073903:1–4, 2005.

[10] M. Davanço and D. J. Blumenthal, "Exploring slow and dispersive propagation in 2D line-defect photonic crystal waveguides," *2003 IEEE LEOS Annual Meeting Conference Proceedings*, pp. 216–217, 2003.

[11] M. Davanço, A. Xing, J. Raring, E. L. Hu, and D. J. Blumenthal, "Detailed characterization of slow and dispersive propagation near a mini-stop-band of an InP photonic crystal waveguide," *Opt. Express*, vol. 13, pp. 4931–4938, 2005.

[12] N. M. Litchinitser, B. J. Eggleton, and D. P. Patterson, "Fiber bragg gratings for dispersion compensation in transmission: Theoretical model and design criteria for nearly ideal pulse recompression," *J. Lightwave Technol.*, vol. 15, pp. 1303–1313, August 1997.

[13] C. K. Madsen and J. H. Zhao, *Optical Filter Design and Analysis: A Signal Processing Approach*. New York: Wiley-Interscience, 1999.

[14] J. D. Joannopoulos, R. D. Meade, and J. N. Winn, *Photonic Crystals: Molding the Flow of Light*. Princeton, N.J.: Princeton, 1995.

[15] S. G. Johnson and J. D. Joannopoulos, "Block-iterative frequency-domain methods for Maxwell's equations in a planewave basis," *Opt. Express*, vol. 8, no. 3, pp. 173–190, 2001.

[16] M. Qiu, "Effective index method for heterostructure-slab-waveguide-based two-dimensional photonic crystals," *App. Phys. Lett.*, vol. 81, pp. 1163–1165, 2002.

[17] M. Qiu and S. He, "Guided modes in a two-dimensional metallic photonic crystal waveguide," *Physics Lett. A*, vol. 266, pp. 425–429, February 2000.

[18] M. Qiu, K. Azizi, A. Karlsson, M. Swillo, and B. Jaskorzynska, "Numerical studies of mode gaps and coupling efficiency for line-defect waveguides in two-dimensional photonic crystals," *Phys. Rev. B*, vol. 64, pp. 155113:1–5, 2000.

[19] H. Benisty, "Modal analysis of optical guides with two-dimensional photonic band-gap boundaries," *Jour. App. Phys.*, vol. 79, pp. 7483–7492, 1996.

[20] H. Kroemer, *Quantum Mechanics: For Engineering, Materials Science and Applied Physics*. Englewood Cliffs, N.J.: Prentice Hall, 1994.

[21] L. A. Coldren and S. W. Corzine, *Diode Lasers and Photonic Integrated Circuits*. New York: Wiley-Interscience, 1999.

[22] P. Yeh, *Optical Waves in Layered Media*. New York: Wiley-Interscience, 1988.

[23] S. Olivier, H. Benisty, C. Smith, M. Rattier, C. Weisbuch, and T. F. Krauss, "Transmission properties of two-dimensional photonic crystal channel waveguides," *Opt. Quantum Electron.*, vol. 34, pp. 171–181, 2002.

[24] A. Yariv, *Optical Electronics*. Fort Worth: Saunders College Printing, 1991.

[25] A. Adibi, Y. Xu, R. K. Lee, M. Loncar, A. Yariv, and A. Scherer, "Role of distributed bragg reflection in photonic-crystal optical waveguides," *Phys. Rev. B*, vol. 64, p. 041102, 2001.

[26] N. M. Litchinitser, B. J. Eggleton, and G. P. Agrawal, "Dispersion of cascaded fiber gratings in WDM lightwave systems," *J. Lightwave Technol.*, vol. 16, pp. 1523–1529, August 1998.

[27] S. Olivier, H. Benisty, C. Weisbuch, C. Smith, T. F. Krauss, and R. Houdré, "Coupled-mode theory and propagation losses in photonic crystal waveguides," *Opt. Express*, vol. 11, p. 1490, 2003.

[28] J. M. Bendickson, J. P. Dowling, and M. Scalora, "Analytic expressions for the electromagnetic mode density in finite, one-dimensional photonic band-gap structures," *Phys. Rev. E*, vol. 53, pp. 4107–4121, 1994.

[29] G. Lenz, B. J. Eggleton, C. K. Madsen, and R. E. Slusher, "Optical delay lines based on optical filters," *J. Quantum Electron.*, vol. 37, pp. 525–532, April 2001.

[30] R. Kashyap, *Fiber Bragg Gratings*. San Diego, CA: Academic Press, 1999.

[31] M. L. Mašanović, V. Lal, J. A. Summers, J. S. Barton, E. J. Skogen, L. G. Rau, L. A. Coldren, and D. J. Blumenthal, "Widely-tunable monolithically-integrated all-optical wavelength converters in InP," *J. Lightwave Technol.*, vol. 23, pp. 1350–63, 2005.

[32] C. Aramburu, C. Vázquez, M. Galarza, M. López-Amo, and J. M. S. Pena, "Mode filter using multimode interference principles: Design and tolerance analysis for accessing waveguides supporting two guided modes," *Microw. Opt. Tech. Lett.*, vol. 26, no. 2, p. 140, 2000.

Chapter 4

Fabrication Technique

4.1 Introduction

In this chapter the process used for the fabrication of experimental test devices is explained in detail. One of the main goals of this investigation was the development of a fabrication platform that could allow the incorporation of photonic crystals (PCs) to Photonic Integrated Circuits (PICs) based on a mature, pre-existing platform [1]. PICs based on this platform were fabricated on epitaxially-grown wafers encompassing a weak vertical confinement InP/InGaAsP slab waveguide with quantum-wells that topped the quaternary guiding layer. Quantum wells could nevertheless be selectively eliminated from specific wafer regions, before a top InP regrowth step. Weakly confining, electrically pumped waveguides etched on the top InP layer defined the different functional components of the circuit, such as laser gain and phase regions, optical amplification and detection. An example of a complex PIC incorporating a PC would be an interferometric wavelength converter realized with regular ridge waveguides and including an internal

source, as described in [1], which would include an extremely compact, passive PC at its output for elimination of the input signal.

Starting from the established PIC fabrication process, compatible steps for PC incorporation were added based on a previously developed process used for the realization of membrane-type PCs [2]. This process involved the definition of PC patterns on top of pre-existing etched InP mesas; precise alignment between PC patterns and surrounding structures was ensured with electron-beam lithography alignment techniques. Slight modifications to both processes had to be introduced in order to maintain compatibility between each fabrication step. A detailed description of the process flow is given in Section 4.2

The technique used for the definition of the sub-micrometer-scale PC features was Electron-Beam Lithography (EBL). Details of the utilization of this technique, including proximity-effect corrections, are explained in Section 4.3.

One of the most difficult tasks faced in the the process development consisted in finding an etching recipe for the very deep ($> 2\mu$m), high aspect-ratio holes required. Etching in an Inductively-Coupled Plasma (ICP) etching system with chlorine-based chemistries was investigated for this purpose, finally yielding sufficiently deep holes with acceptable sidewall roughness and tilt angles. Details of this investigation are exposed in Section 4.4.

4.2 General Fabrication Steps

The fabrication process reported here is a novel form of integration of deeply-etched PC with standard photonic integrated circuit structures [3]. It is based on the fabrication platform described in [1], with added steps for the inclusion of the photonic crystals adapted from the process described in [2].

Epitaxial Structure

A schematic of the epitaxial structure used is shown in Fig. 4.1. The devices were processed on an MOCVD-grown wafer encompassing an n-doped InP substrate, a 1.37Q, 300-nm-thick intrinsic InGaAsP guiding layer, a 1-μm, p-doped InP cladding layer, a 100-nm layer of highly p-doped InGaAs for the formation of ohmic contacts and finally a 50-nm InP cap layer. Notice that a p-i-n junction is formed between the top cladding and the n-doped substrate.

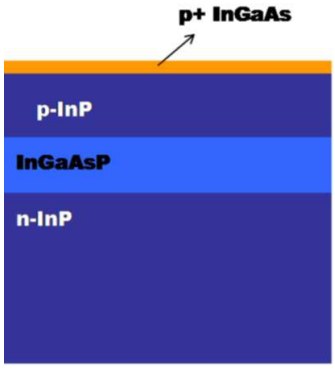

Figure 4.1: Wafer epitaxial structure.

This epitaxial structure is very similar to that used in [1], except that the top cladding layer is 1μm thinner. The upper cladding layer thickness reflects a compromise between achievable etched hole depth and losses at the highly-conductive

InGaAs layer. It was desired to minimize the interaction of the waveguide mode's evanescent tail with the top InGaAs layer and highly p-doped InP; this demanded a thicker cladding. On the other hand, at the time of the processing the concern existed that the etching technique would not be sufficient for the achievement of hole depths of more than 2μm. A 1μm cladding thus seemed to constitute a good compromise, even if larger propagation losses were expected. It must be pointed out that the current InP hole-etching recipe allow the formation of holes more than 3μm deep and can in principle be tuned for even higher aspect-ratios.

Waveguide definition

Ridge waveguides and mesa patterns were defined initially on a PECVD-deposited SiN mask layer by contact photolithography. The pattern was transferred to the SiN mask by Reactive Ion Etching (RIE) in a CF_4:O_2 plasma. Next they were transferred into the upper cladding layer by RIE using a Methane-Hydrogen-Argon (MHA) mixture, followed by a 1:3 HCl:H_3PO_4 wet-etching step. The dry-etch step is timed so that approximately 200nm of InP is left in the unprotected regions.

Wet-etching in an HCl:H_3PO_4 1:3 solution is realized in order to provide smoother waveguide sidewalls, so that propagation losses can be reduced. The etching is highly anisotropic; ridge waveguides defined on the sample to be parallel to the [011] InP crystal plane result with a slight undercut as depicted in Fig. 5.2(b), with $\approx 4^\circ$-tilted sidewalls.

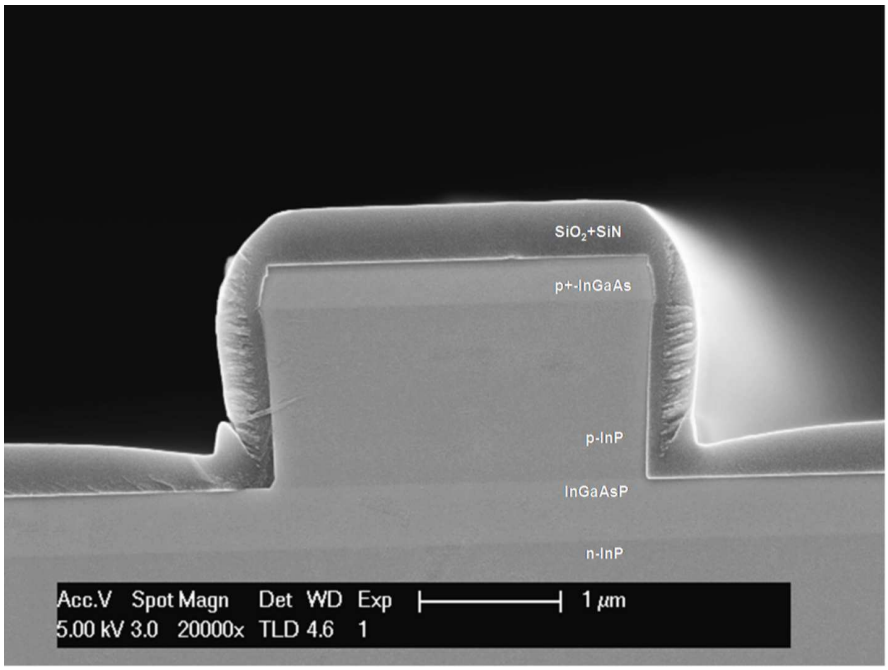

Figure 4.2: Cross-section of ridge waveguide.

Inasmuch as this does not cause serious problems in the waveguiding characteristics, Electron-Beam Lithography (EBL) alignment markers present on the sample can be sufficiently altered to cause problems in the photonic crystal lithography step. These markers consist of 'L-' or cross-shaped ridges of width 3μm and length 20μm and are used as references for the location and alignment to the mesas on top of which PC patterns are to be exposed. Fig. 4.3 shows one such marker after the wet-etch. To circumvent this problem, markers are protected with a thick ($\approx$3μm) layer of AZ-4330 photoresist prior to the wet-etch. Acid attack is thereby effectively avoided.

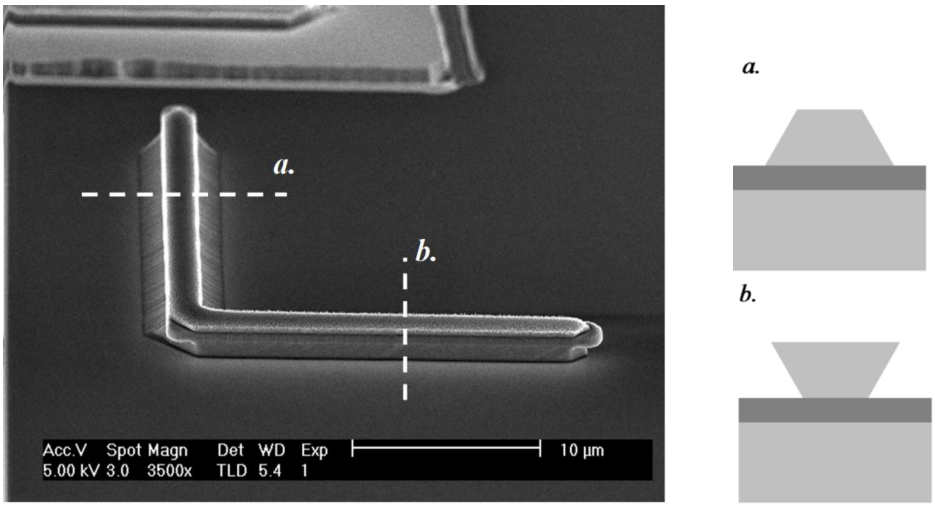

Figure 4.3: SEM of e-beam write direct-write alignment mark and schematic of ridge cross-sections in two perpendicular directions.

SiN and SiO_2 Deposition

After ridges have been defined, a 100nm layer of SiN is deposited on the sample to provide isolation for electrical contacts. A lithography step follows in which mesa-tops are cleared of the SiN.

A 400-450nm layer of SiO_2 is deposited, which will serve as a hard etch-mask for the PC patterns. The large thickness of this layer is necessary due to the highly agressive InP dry-etch step, especially since very deep holes are required.

Sample Planarization

At this point in the process flow, the sample surface is no longer planar, having a 1μm depth variation. In order to ensure both electron-beam resist uniformity and full coverage of all structures on its surface, the sample is planarized with PMGI. The procedure is as follows: PMGI SF-11 is thrice spun at 4000 RPM and baked on a hot plate at 200°C. The sample is next baked in a convection oven at

300°C in an enclosed aluminum boat for 15 minutes. In general, the PMGI surface presents variations of the order of 100nm after this procedure. Dry-etching in an oxygen plasma follows until mesa surfaces are once again exposed. The ZEP-520A photoresist is next spun on the surface prior to the electron-beam lithography. Notice that the tolerance in the PMGI O_2 plasma etch can become very strict for thinner e-beam resists. In the present case, a resist thickness of 500nm was chosen, which permitted the sample surface to vary within 200nm without serious implications.

This planarization step was adapted from that developed by Aimin Xing for fabrication of membrane-type PC on top of InP mesas, detailed in [2]. Very precise (better than 100nm) alignment between PC patterns and etched waveguides was ensured by the EBL direct-write alignment feature.

Photonic Crystal Lithography and Etching

Electron-beam lithography follows the previous step to define PC patterns on top of the mesas. As mentioned above, alignment marks were used so that the patterns could be aligned to the mesas with a tolerance of less than 100nm. After development, the patterns are transferred to the SiO_2 mask with a CHF_3 plasma in a Panasonic E640 Inductively-Coupled Plasma (ICP) etcher.

The sample is next etched in a Unaxis Versalock ICP etcher, using a Cl_2:Ar 1:5 chemistry at 1.5mT and 200°C. This etch was long enough to yield holes extending through the upper cladding and waveguide layers, then about 1μm into the substrate.

Electrical Contacts

A semi-self-aligned resist etch-back technique was used to create openings for contacts on the remaining SiO_2 and SiN layers on selected, lithographically-defined portions of the ridge waveguides. This step is as follows: PMGI is spun and planarized on the surface, followed by spinning of AZ4110 photoresist. Optical lithography is used to define openings in the latter, on top of selected waveguide regions. The AZ400K developer used does not attack the underlying PMGI layer. Dry etching with oxygen plasma is next used to etch-back the exposed PMGI regions until only the waveguide tops are exposed. The SiO_2 and SiN on top of the guides are finally etched in a CHF_3 plasma.

Following these steps, metallic contacts were defined with contact photolithography, using a dual-photoresist-layer scheme: PMGI SF-15 (resulting in a $\approx 3\mu$m thickness at 4000RPM spin speed) was first spun on the wafer surface and baked at $200°C$ for 2 minutes and deep-UV exposed for 100 seconds. The latter pre-exposure step was to ensure the formation of a PMGI undercut. AZ4110 photoresist was next spun on the surface at 4000RPM ($\approx 1\mu$m thickness), soft baked, exposed and developed in AZ400K developer, which did not attack the PMGI layer. UV-exposure of PMGI for 300 seconds followed, and development in SAL-101 was carried out until the polymer was fully developed. This process in general required repetition of the UV-exposure, development and inspection step to ensure a good development and undercut formation. Lithography was followed by 200/400/5000Å Ti/Pt/Au e-beam evaporation at a $\approx 45°$ angle for sidewall cov-

erage. The sample was subsequently thinned down and metallization of the backside with 200/400/5000Å Ti/Pt/Au was performed before cleaving. A schematic diagram of the fabricated structures is shown in Fig 4.4(a) and an optical microscope image is shown in Fig 4.4(b)

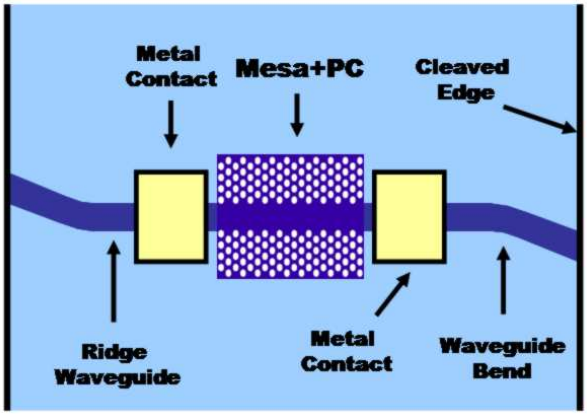

(a)

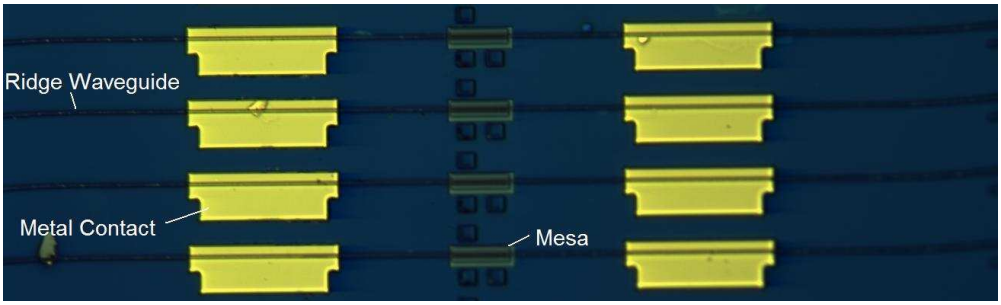

(b)

Figure 4.4: (a)Top-view schematic of fabricated devices. (b) Top-view optical microscope image of finalized devices.

4.3 Electron-Beam Lithography

Electron-beam lithography was realized using a JEOL JBX-5DII(U) system. The machine was operated at a 50kV voltage in high-resolution mode, with a beam current of 95pA. This offered a beam spot-size of ≈10nm and a minimum

step-size of 2.5nm. The maximum writable field (without stage movement) was $80\times80\mu m^2$. Larger field areas can be written, however field-stitching errors might occur.

The system offers a direct-alignment feature that uses on-chip reference marks for precise pattern location. Global reference marks are used for overall wafer rotation corrections, and are in general widely spaced. Chip reference marks located within an $80\times80\mu m^2$ area surrounding the pattern-write regions are used for precise pattern alignment. In principle, three chip marks can be used for local rotation and gain corrections, yielding an alignment tolerance of better than 50nm. In the present case however only one chip mark was used, which yielded a tolerance of better than 100nm. Chip-mark detection is realized previously to each exposure. In the present work, global chip marks were 90° crosses composed of $3\times50\mu m^2$ ridges etched on the InP surface. Chip marks were L-shaped, formed by $3\times20\mu m^2$ ridges.

Due to the 2.5nm step-size limitation, circular patterns were approximated as polygons whose vertices fell on a grid defined accordingly.

The lithography was realized with ≈500nm ZEP520A photoresist. This is a high-resolution positive resist that is developed in 100% amyl acetate, followed by methyl-isobutyl-ketone and isopropanol dips. The thickness was chosen based on the etch selectivity of the long SiO_2 mask etching step.

4.3.1 Exposure Dose Calibration

Lithography calibration was carried out initially on plain InP samples covered with a 450nm-thick layer of SiO_2. The oxide was deposited using high-density Inductively Coupled Plasma (ICP) Plasma Enhanced Chemical Vapor Deposition (PECVD) in a Unaxis VLR system.

The calibration process was as follows: PC patterns were initially exposed with various current doses on the sample surface. The resist was developed after exposure, followed by etching of the SiO_2 mask. Patterns on the hard SiO_2 mask were next transferred to the semiconductor and the mask was subsequently removed with Hydrofluoric acid (HF). Inspection of the patterns was finally carried out with a Field Emission Scanning Electron Microscope (FE-SEM). This instrument was a Sirion FEI SEM, which offered a resolution of ≈2nm at an accelerating voltage of 5kV.

The dimensions of the PC pattern features were measured from SEM-produced images. For each pattern, hole diameter dimensions were normalized to the respective lattice constants, yielding reliable estimates for air filling fractions. Exposure doses were associated with corresponding filling fractions. Subsequent calibration runs were carried out with refined current dose modulations, based on the previous results, to yield the desired feature sizes.

Proximity Effect Correction

During electron-beam exposure of a particular region on the sample surface, scattered electrons tend to add to the total exposure dose of neighboring areas. This results in a non-uniform dose distribution that yields, upon development, to a distorted version of the desired pattern [4, 5]. The level of distortion clearly

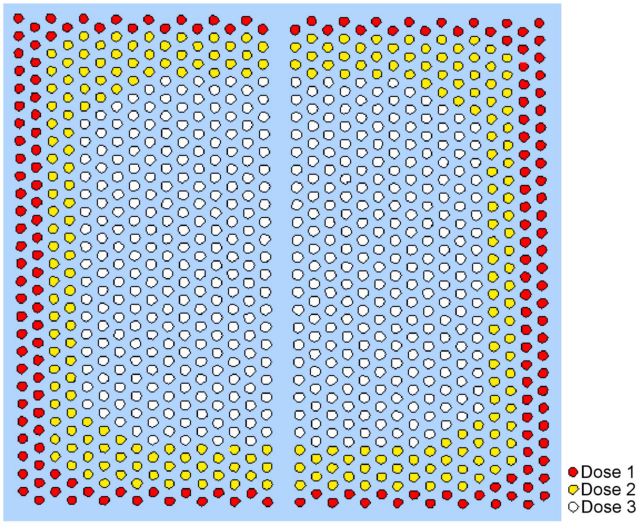

Figure 4.5: Dose map for proximity effect correction. Holes close close to the pattern edges tend to receive lesser effective doses, thus Dose 1 > Dose 2 > Dose 3.

depends on the proximity between the different exposed regions: closely-spaced shapes will be affected by each other's exposure doses. This effect is particularly detrimental to photonic crystal waveguides since a large hole-size non-uniformity may result: holes surrounded by many neighbors (i.e. at the waveguide center) will end up with much larger diameters than those at the pattern edges. As predicted in Chapter 3, even slight variations in hole size may cause very large band-structure frequency shifts and thus must be avoided. In order to circumvent this effect, a modulation of exposure doses assigned to holes in different region

of a pattern was realized. Figure 4.5 illustrates this procedure. The calibration

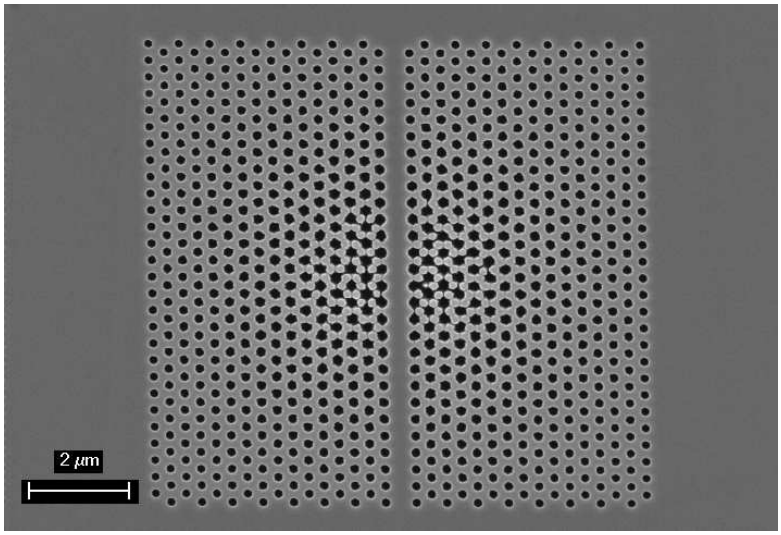

(a)

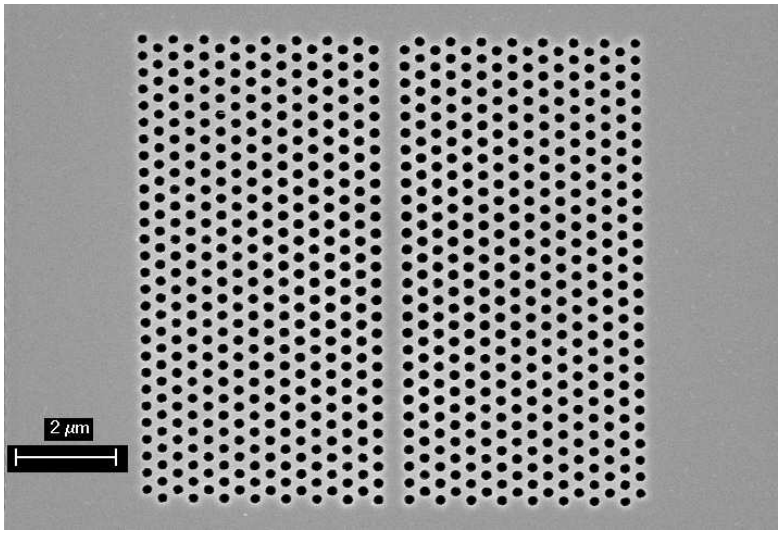

(b)

Figure 4.6: Top-view SEM images of photonic crystal patterns (a) without and (b) with proximity effect correction. In (a), holes in the center of the pattern have collapsed into each other.

of the dose modulation was carried out by exposing multiple copies of the same pattern with dose distributions departing slightly from the original, followed by development, etching and SEM inspection. This process yielded a hole-size uniformity of above 90% to be achieved. Figures 4.6(a) and 4.6(b) clearly show the

benefit of proximity effect correction. Modulation of individual hole-pattern sizes and doses also allowed the realization of PC waveguide sidewall tapers, as shown in Fig. 4.7.

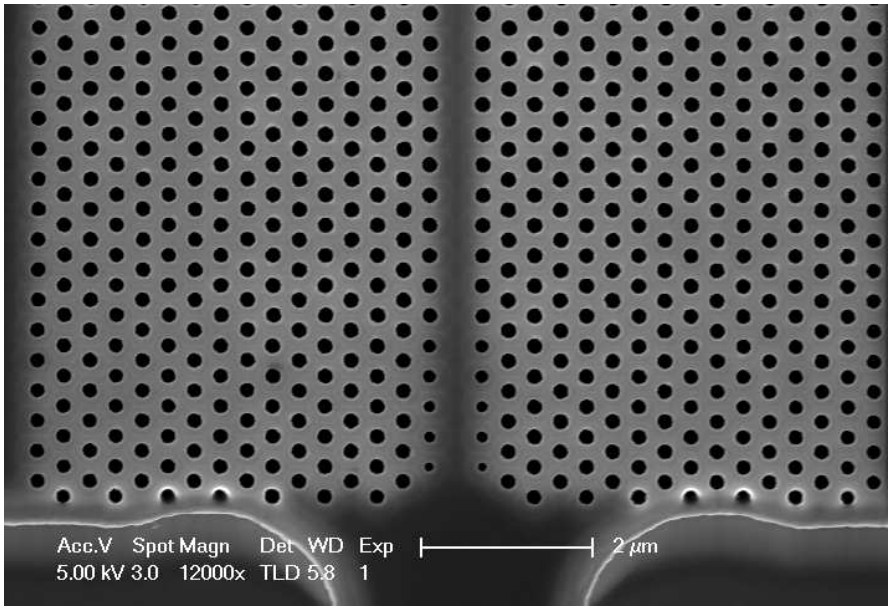

Figure 4.7: Tapered-wall photonic crystal waveguide created with modulation of both hole-pattern size and exposure dose.

The present approach to proximity-effect correction is somewhat rudimentary and incomplete, however it yields reasonable PC uniformity in a fast way. More involved and complete methods have been developed involving mathematical formulations of the proximity effect and dose-compensation algorithms [6, 7, 8]. The dose compensation in such cases is realized at each exposure point and is generally shape dependent, leading to a much higher level of fidelity and uniformity.

4.4 High Density Plasma Etching

Plasma-etching processes are expected to be mostly driven both by ion bombardment of the sample surface and chemical reactions with generated radicals. Control of the physical and chemical components of the etching process can under these circumstances be realized by the control of radical and ion concentrations available in the chamber. In simple gas-discharge plasma processes (for instance, reactive ion etching [5]), the concentrations of these two groups of chemical species are generally very small with respect to the gas volume, a characteristic which limits both the etching throughput and flexibility. In order to overcome these limitations, a few different techniques have been successfully developed for the generation of high density plasmas (i.e. with ion concentrations exceeding 10^{11}cm^{-3}) that could be tuned with many degrees of freedom, generally offering much improved etch-rates and feature quality. Added advantages are the possibility of operation of the plasma reactor at very low chamber pressures (<10mtorr) and low electrode DC biases. Two popular high-density plasma generation techniques are Electron-Cyclotron Resonance (ECR) and Inductively Coupled Plasma (ICP), both of which make use of transverse electric and magnetic fields in order to increase the amount of collisions experienced by charged particles in the plasma.

The first technique consists in using a static magnetic field and an alternating electric field set at the electron cyclotron resonance condition, such that electrons are set in very efficient circular motion within the plasma. In the second technique,

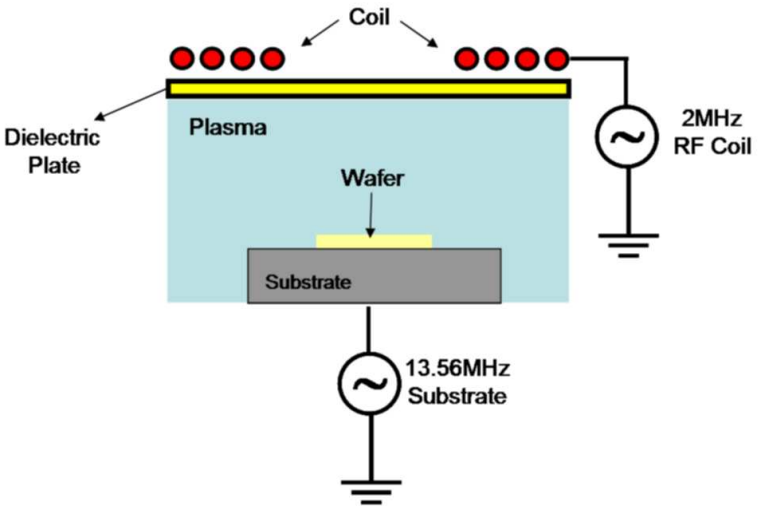

Figure 4.8: Schematic of Inductively Coupled Plasma (ICP) etching chamber.

the plasma is driven by a magnetic potential set up by a coil wound outside dielectric chamber walls. Coil and plasma are inductively coupled in a similar way as the two sides of an electrical transformer [9] so that part of the RF power applied to the coil is delivered to the plasma. A schematic of the reactor is shown in Fig. 4.8. Two independent power supplies are used in the system: a low frequency supply is used to generate a high-density plasma above the surface of the wafer; a high frequency supply provides wafer bias, driving ions towards the substrate. Considerable etch rates at low DC bias (i.e. low ion energies), resulting in low wafer damage are thereby obtained.

Two ICP etching systems available at the UCSB fabrication facilities were used to perform the photonic crystals dry etching steps for the present work. A Panasonic E640 system was used for etching of the thick, 450-nm SiO_2 etch-mask after the EBL step, with a CHF_3 plasma. A Unaxis Versalock system was next used for Cl_2-based etching of the InP. Both etches used very low pressures

to ensure sidewall straightness and sufficient etch-depth, as well as high plasma excitation.

4.4.1 SiO_2 Mask Etching

Etching of InP in a high-density Cl_2 plasma requires a hard mask for pattern definition. In the present case, a high-density, ICP PECVD-deposited film of SiO_2 was used for this purpose, which offered an appropriate degree of selectivity for deep hole etching in InP; moreover, the available deposition process was reliable and easy to use. The required film thickness was nevertheless considerably large ($\approx$450nm), thus use of a high-density plasma etching technique became necessary. The SiO_2 mask was etched in a CHF_3 plasma with a Panasonic E640 ICP etcher under the following conditions: 0.25 Pa chamber pressure, 900W ICP power, 200W RIE power and 40sscm CHF_3 flow. The etch-rate achieved was approached 2.5nm/s with a selectivity of $\approx$1.4. Sidewalls presented a 3-5° tilt, as depicted in Fig. 4.9. Notice in the picture that the InP substrate seems to be slightly etched; this is a result of sputtering by high-energy plasma particles. A good etch-time calibration is thus necessary to avoid excessive sputtering and sidewall roughness due to photoresist degradation. This recipe departed from a pre-existing version that yielded sidewall-angles between 4° and 5° at an etch-rate of 3.9nm/sec and a selectivity of 1.35, with 40sccm CHF_3 flow and 400W power. The faster etch-rate is due to the increased RIE power. This is also most likely the reason behind the rougher sidewalls observed in Fig. 4.10(a), as compared to the sidewalls obtained

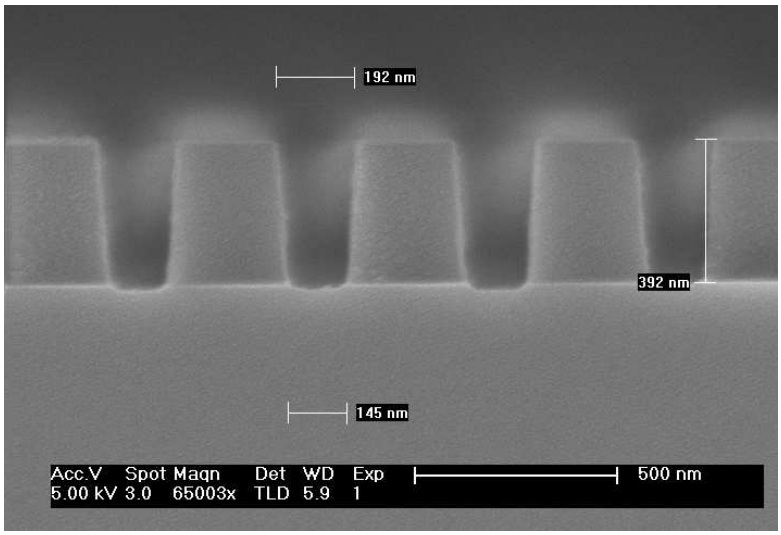

Figure 4.9: Cross-sectional SEM image of SiO_2 ridges etched with P=0.25Pa, P_{ICP}=900W, P_{RIE}=200W, Q_{CHF_3}=40sccm.

with the final recipe, shown in Fig. 4.10(b). Worse resist degradation was also observed, which might have had a significant contribution to sidewall roughness. The top-view SEM image of the etched holes shown in Fig. 4.11 illustrate the high sidewall smoothness provided by the etching recipe.

The 3°-5° SiO_2 mask sidewall angles caused InP-etched holes to be considerably smaller than the exposed patterns: for a 450-nm-thick mask layer, hole diameters were between 40nm and 80nm smaller at the InP surface than at the top SiO_2 mask surface.

4.4.2 InP Etching

The stringent PC hole depth requirement demanded the use of Chlorine chemistries for InP etching, which have been shown to produce large etch-rates and features with very high aspect-ratios [3], [10]. The introduction of different gaseous

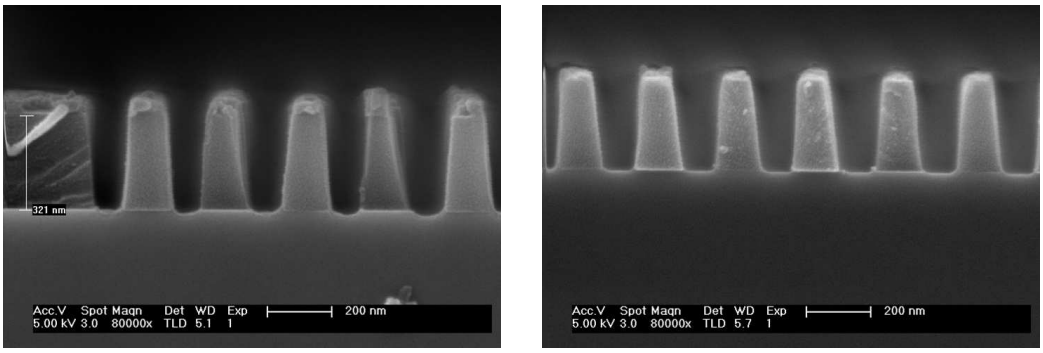

(a) (b)

Figure 4.10: Cross-sectional SEM image of SiO_2 ridges etched with (a)P=0.25Pa, P_{ICP}=900W, P_{RIE}=400W, Q_{CHF_3}=40sccm and (b) same conditions as in Fig. 4.9.

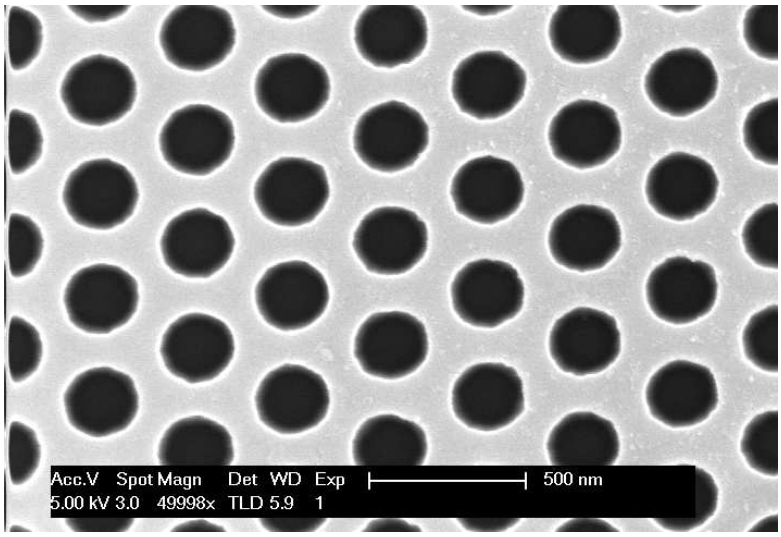

Figure 4.11: Top-view SEM image of etched holes with the recipe from Fig. 4.9.

species -such as Ar or N_2- permits better control over the balance of chemical and physical components of the etching process, which will reflect upon etch-rate and feature quality.

In general, high substrate temperatures ($\geq$200°) are necessary for the equalization of desorption rates of In- and P- reaction products in the Chlorine plasma [1].

[1]Indium compounds ($InCl_x$, x=1..3) are to be considerably less volatile then Phosphorus products (PCl_x x=1..5).

High temperatures are also required to avoid differential etching of InP and Ga-containing epi-layers. The etch-rates of InP and GaAs in Cl_2 have been shown to differ considerably at temperatures lower than 175° [11]. Another form of dealing with the differential desorption rates is by increasing the physical sputtering component of the etch process with high-energy ions. Desorption of $InCl_3$ can be enhanced by increased plasma densities, as described in [3].

Low pressures (<10mTorr) are in general required for the achievement of deeply etched high aspect-ratio holes. As holes deepen during the etch process, transport of reactive species into the cavities becomes less efficient, as well as the removal of reaction products; in addition, reaction products tend to be re-deposited on the hole sidewalls. These effects cause etch-rate reduction and in general result in holes with tilted sidewalls and limited depth, depending on the aspect-ratio [12]. It may be argued that the benefits of low pressure in high aspect-ratio feature etching are related to the larger mean-free-paths of the reactive species, which would result in a smaller spread in the incidence angle of radicals and ions upon the substrate. Low pressures however are also usually associated with an increased bias voltage build-up between plasma and substrate, which cause ions to strike the sample surface in with higher energies. This would constitute an equally important factor for the achievement of high aspect-ratios.

Two different chemistries were investigated for InP etching: a Cl_2:N_2 mixture and a Cl_2:Ar mixture. The former produced smooth sidewalls, however with a considerable tilt angle, which resulted in limited hole depth. The chemistry

produced rougher and irregular sidewalls, however extremely deep holes, with a much better selectivity than in the previous case.

Cl_2:N_2 Chemistry

Achievement of smooth sidewalls depends on the enhancement of $InCl_x$ etch-product desorption with respect to the desorption rate of PCl_x. The introduction of N_2 leads under specific conditions to a reduction in Cl radical density which limits the formation and desorption of PCl_x; non-volatile compounds such as $InCl_2$ and P are produced in this case [13].

Increased levels of N_2 in the mixture may additionally lead to reduced PCl_x formation due to the formation of non-volatile P_3N_5 [14]. A cross-sectional SEM image of $\approx$ 6-aspect-ratio PC holes etched at $200°C$ with a 12:28 Cl_2:N_2 mixture in an 8-mTorr-pressure environment with 500W ICP power and 200W RIE power are shown in Fig. 4.12. Extremely smooth sidewalls are achieved with this recipe, however with a limited hole depth of 2.0μm and a large tilt angle. These features are most likely related to the formation of non-volatile compounds. The top-view SEM image of the etched holes shown in Fig. 4.12(c) illustrate the high sidewall smoothness provided by the etching recipe.

Cl_2:Ar Chemistry

The introduction of argon in the etching mixture adds a considerably stronger physical etching component that allows achievement of holes with very high aspect-ratios in detriment of sidewall smoothness. In this case, an enhanced desorption

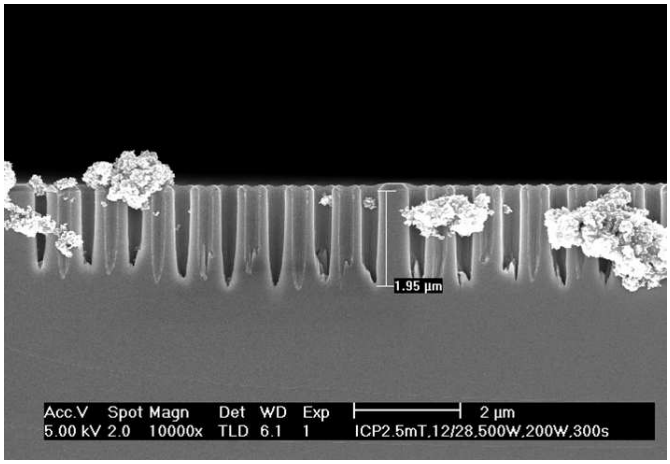

(a)

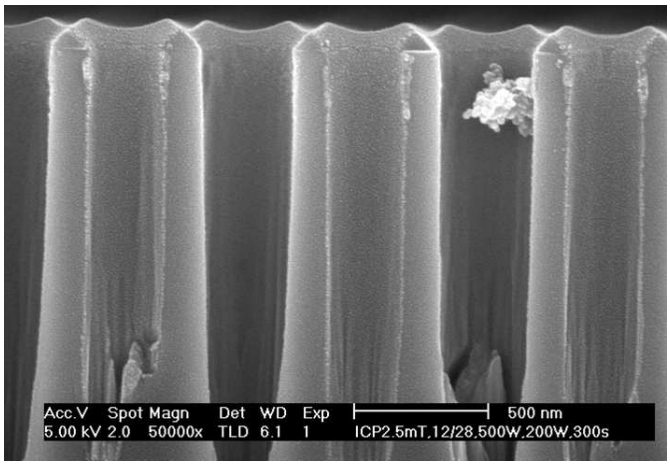

(b)

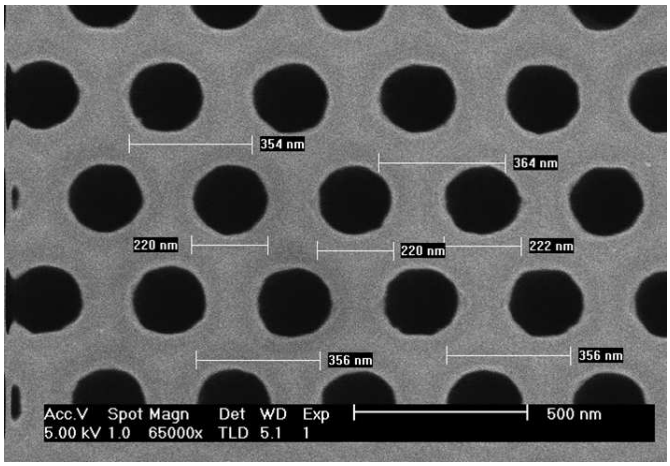

(c)

Figure 4.12: (a) Cross-sectional SEM of photonic crystal holes etched with P = 8mTorr, P_{ICP}=500W, P_{RIE}=200W, Cl_2:N_2 12:28sccm. (b) Detail of (a). (Pictures courtesy of Aimin Xing.) (c) Top-view SEM image of etched holes with the same recipe.

rate of low-volatility $InCl_3$ can be achieved with high substrate temperature, low pressure and high plasma density [3].

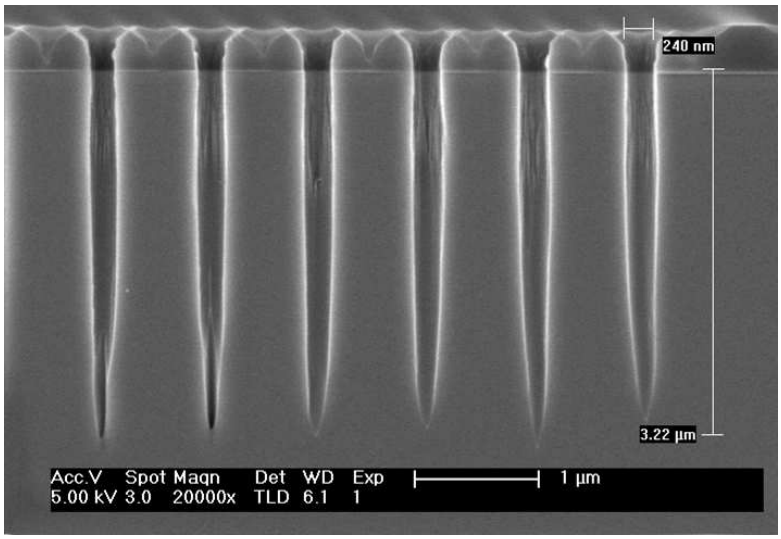

Figure 4.13: Cross-sectional SEM of PC holes etched in an InP substrate with a Cl_2:Ar 1:5 mixture at T=200°C, P=0.25Pa with P_{ICP}=900W, P_{RIE}=200W.

Figure 4.13 shows PC holes etched at $200°C$ with a 1:5 Cl_2:Ar mixture in an 1.5-mTorr-pressure environment with 900W ICP power and 200W RIE power. In order for the chamber pressure to be maintained at a stable position, the actual gas flows used were Q_{Cl_2}= sccm and Q_{Ar} = sccm. A 3.2μm hole depth with as aspect-ratio of ≈12 was achieved over an etching time of 160s; etch-rate and selectivity with respect to the SiO_2 mask were ≈20nm/sec and ≈ 10 respectively. Notice however the increased sidewall roughness and non-uniformity in comparison to the N_2-etched holes. This can also be observed from the top-view SEM of the etched holes shown in Fig. 4.14.

Despite the roughness and sidewall non-uniformity, the present recipe was used to etch holes with depth larger than 2μm, as required for the complete overlap of

the epi-structure fundamental slab mode. The profile of holes etched on epitaxial material can be seen in Fig 4.15. Notice that holes extend through top InGaAs, InP top-cladding, InGaAsP guiding layer and about 1μm into the substrate. The experimental results provided in Chapter 6 demonstrate that the incurred-upon hole imperfections were sufficiently small to yield clearly distinguishable photonic band-gap effects.

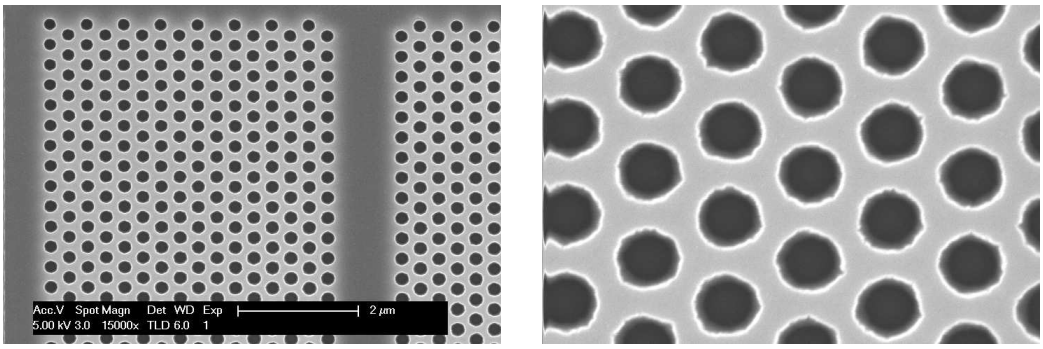

(a) (b)

Figure 4.14: (a) Top view of PC holes etched with the recipe from Fig. 4.13. (b) Detail of (a).

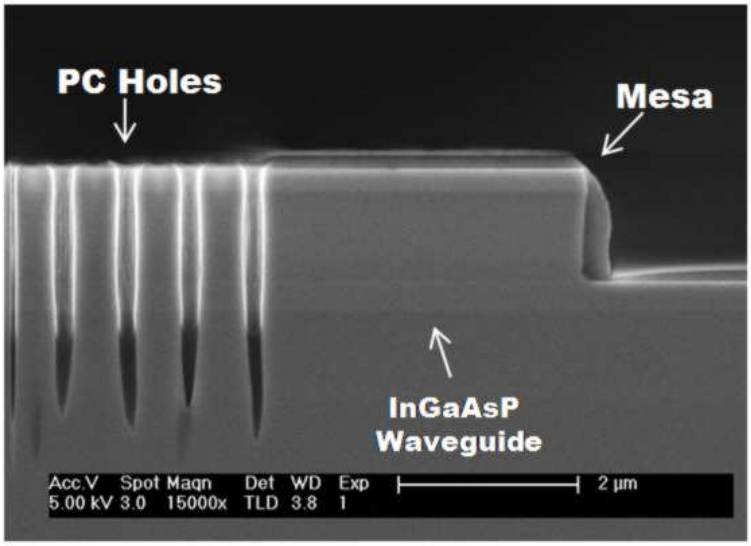

Figure 4.15: Cross-sectional SEM figures of PC holes etched on the epi-structure from Fig. 4.1 with the recipe from Fig. 4.13

4.5 Summary and Conclusions

A fabrication process was developed that allowed the incorporation of deeply etched Photonic Crystals in InP Photonic Integrated Circuits based on a pre-existing integration platform [1]. Fabricated structures include weakly confining ridge waveguides that can be electrically pumped and photonic crystals patterns composed of holes of more than 2μm deep.

Electron-beam lithography was used for the definition of PC patterns, with proximity-effect corrections to ensure low shape distortions.

High-density (inductively-coupled) plasma etching with two different chlorine mixtures was investigated to produce extremely high aspect-ratio holes with diameters of less than 200nm. A Cl_2:N_2 mixture was found to produce holes with very smooth sidewalls however with insufficient depth and considerable sidewall tilts. A Cl_2:Ar mixture was finally established that produced the desired hole depth, however with a higher level of sidewall roughness and non-uniformity. This recipe was used for deep hole etching of the final devices.

References

[1] M. L. Mašanović, V. Lal, J. A. Summers, J. S. Barton, E. J. Skogen, L. G. Rau, L. A. Coldren, and D. J. Blumenthal, "Widely-tunable monolithically-integrated all-optical wavelength converters in InP," *J. Lightwave Technol.*, vol. 23, pp. 1350–63, 2005.

[2] A. Xing, M. Davanço, D. J. Blumenthal, and E. L. Hu, "Fabrication of InP-based two-dimensional photonic crystal membrane," *J. Vac. Sci. Technol. B*, vol. 22, no. 8, pp. 70–73, 2004.

[3] T. D. Happ, A. Markard, M. Kamp, A. Forchel, S. Anand, J.-L. Gentner, and N. Bouadma, "Nanofabrication of two-dimensional photonic crystal mirrors for 1.5 mm short cavity lasers," *J. Vac. Sci. Technol. B*, vol. 19, pp. 2775–2778, Nov/Dec 2001.

[4] T. H. P. Chang, "Proximity effect in electron-beam lithography," *J. Vac. Sci. Technol. B*, vol. 12, pp. 1271–1275, Nov/Dec 1975.

[5] S. A. Campbell, *The science and engineering of microelectronic fabrication.* New York: Oxford University Press; 2nd edition (February 15, 2001), 2001.

[6] M. Parikh, "Corrections to proximity effects in electron beam lithography. i. theory," *Jour. App. Phys.*, vol. 50, no. 6, pp. 4371–4377, 1979.

[7] M. Parikh, "Corrections to proximity effects in electron beam lithography. ii. implementation," *Jour. App. Phys.*, vol. 50, no. 6, pp. 4378–4382, 1979.

[8] M. Parikh, "Corrections to proximity effects in electron beam lithography. iii. experiments," *Jour. App. Phys.*, vol. 50, no. 6, pp. 4383–4387, 1979.

[9] R. Piejak, V. Godyak, and B. Alexandrovich, "A simple analysis of an inductive rf discharge," *Plasma Sources Sci. Technol.*, vol. 1, pp. 179–186, 1992.

[10] J. Mossburger, M. Kamp, A. Forchel, R. Ferrini, D. Leuenberger, R. Houdré, S. Anand, and J. Berggren, "Nanofabrication of high quality photonic crystals for integrated optics circuits," *Nanotechnology*, vol. 13, pp. 341–345, 2002.

[11] D. G. Lishan and E. L. Hu, "Cl_2 and HCl radical beam etching of GaAs and InP," *Appl. Phys. Lett.*, vol. 56, pp. 1667–1669, April 1990.

[12] E. W. Berg and S. W. Pang, "Low-pressure etching of nanostructures and via holes using an inductively coupled plasma system," *J. Electrochem. Soc.*, vol. 146, no. 2, pp. 775–779, 1999.

[13] J. Lin, A. Leven, N. WQeimann, Y. Yang, R. K. Kopf, R. Reyes, Y. K. Chen, and F. Choa, "Smooth and vertical-sidewall InP etching using cl_2/n_2 inductively coupled plasma," *J. Vac. Sci. Technol. B*, vol. 22, pp. 510–512, Mar/Apr 2004.

[14] S. Miyakuni, R. Hattori, K. Sato, and O. Ishihara, "Low ion energy electron cyclotron resonance etching of InP using a cl_2/n_2 mixture," *J. Appl. Phys*, vol. 78, pp. 5734–5738, November 1995.

Chapter 5

Photonic Crystal Characterization Technique

5.1 Introduction

This chapter describes the experimental techniques used to characterize the passive deeply etched photonic crystal structures presented in this work. A description of test devices fabricated for passive testing is given initially. Next, modal analysis of the slab waveguide formed by the epitaxial wafer is carried out, followed by modal analysis of the access ridge waveguides. Theoretical and practical aspects of the measurement technique are then detailed, which makes extensive use of Müller matrices. Finally, an important aspect of fiber-to-waveguide coupling is analyzed regarding multi-mode propagation in the access waveguides of the test structures.

5.2 Test Devices

Based on the fabrication platform described in Chapter 4, a series of 20μm-wide mesas were realized with lengths of 10, 30 and 80μm , on top of which PC patterns were to be etched. The mesas were accessed via input and output 3-μm-wide weakly guiding ridge waveguides. These were flared to a width of 5μm close to the cleave-planes of the wafer and designed to meet the edges at a 7° angle, in order to suppress reflections into the fundamental mode at the semiconductor/air interface [1, 2]. The total length of the devices after final cleaving was expected to be between 1400μm and 1600μm. A schematic of the test-devices is shown in Fig. 5.1.

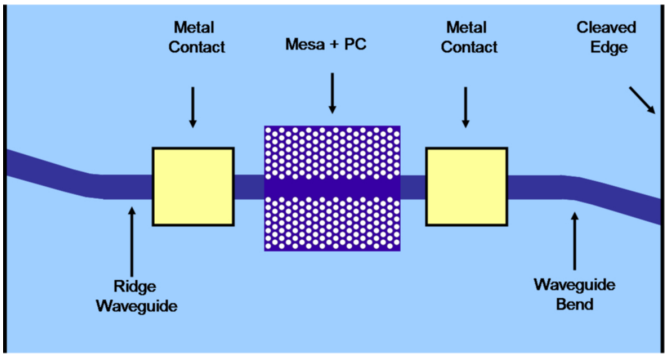

Figure 5.1: Schematic of the devices used for PC characterization.

As described in Chapter 4, the basic epitaxial structure of the devices encompassed an InP substrate, a 300-nm intrinsic InGaAsP guiding layer, a 1-μm InP cladding layer and a 100nm contact layer of highly p-doped InGaAs. A schematic of a ridge waveguide is shown in Fig. 5.2(a), next to a cross-section SEM image of a fabricated guide.

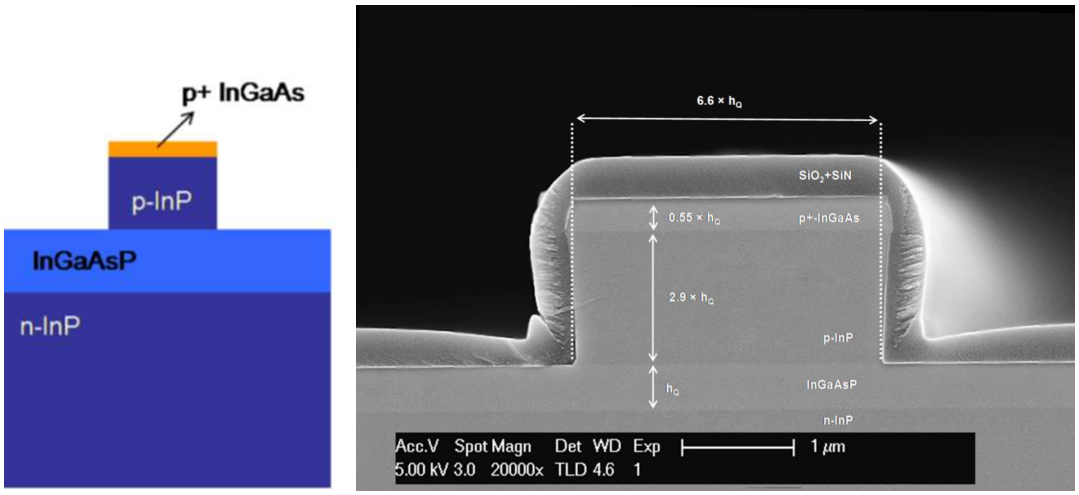

(a) (b)

Figure 5.2: (a) Cross-sectional schematic of ridge waveguide showing the epitaxial layers. (b) Cross-sectional SEM of an access ridge waveguide. All dimensions are relative to the slab waveguide thickness.

Electrical contacts were defined on the ridge waveguides such that guided light could be detected by measuring current from reverse-biased *p-i-n* junctions. This facilitated the coupling of ridge waveguides with lensed fibers during the testing process; optimal alignment is in fact achieved in little more than a minute, requiring no equipment other than a voltage source with a built-in amp meter.

5.2.1 Modal Analysis of Mesas and Access Waveguides

For subsequent design and analysis, modal analysis of the epi-structure and ridge waveguides is now carried out.

5.2.2 Slab Waveguide Modeling

The refractive index of the 1.37Q InGaAsP layer was considered to vary between 3.4 and 3.45 within the optical communications wavelength range. The refractive index of the InP regions was considered to be 3.17, and that of the InGaAs region 3.65 [3].

Based on SEM pictures of waveguide cross-sections (see for instance Fig. 5.2(b)), the actual quaternary layer thickness was estimated to be between $350nm$ and $370nm$; the thickness of the top InP cladding and the InGaAs layers were then all estimated based on this measure, as well as the ridge waveguide width. It must be pointed out that the thickness of the grown InGaAs layer turned out to be considerably larger than the initially desired $100nm$, which might have led to the existence of an additional undesired TE slab propagating mode, as detailed below.

A 1D Finite-Element Method was used to calculate modes of the multi-layer slab waveguide formed by the epi-structure, assuming zero losses in each layer. A schematic of the slab structure is shown in Fig. 5.3.

The slab waveguide offers two guided modes, one in which light is mostly confined in the quaternary layer (henceforth *quaternary* mode), another confined in the contact layer (henceforth *contact*-mode). The top cladding is thick enough that the contact layer has little effect on the quaternary mode effective index; on the other hand, the quaternary layer refractive index and thickness largely influences the conduction mode. Figures 5.4(a) and 5.4(b) show the indices of

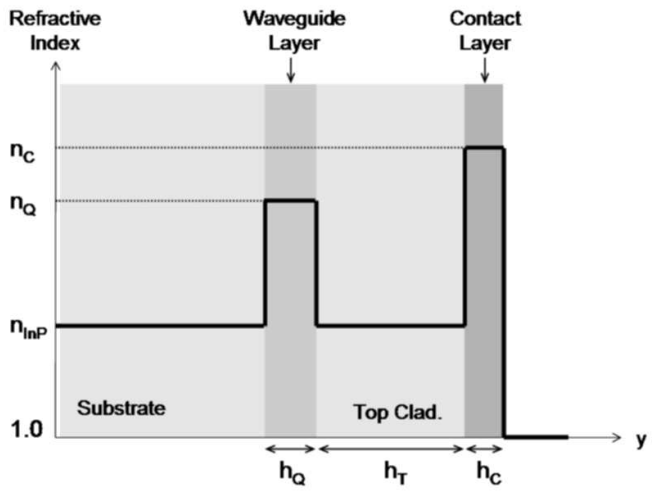

Figure 5.3: Schematic of slab waveguide formed by the epitaxial structure.

TE guided modes for the extremal values of the guiding-layer refractive index and thickness (n_Q and h_Q respectively) as functions of wavelength.

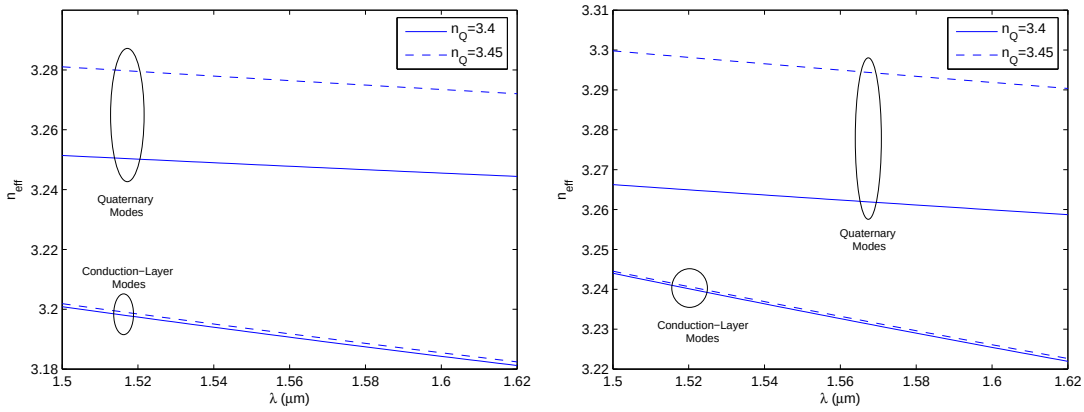

Figure 5.4: Effective refractive indices for quaternary- and contact-modes of the slab waveguide in Fig. 5.3 with (a) $h_Q = 0.3$ (b) $h_Q = 0.35$.

Given the uncertainty in the actual material parameters, the TE fundamental mode effective index is assumed in the next chapters to be between 3.25 and 3.3, based on range of values obtained. At the same time, the existence of a conduction-layer mode with effective indices between 3.17 and 3.23 is admissible.

It must be noted though that the contact layer and top cladding are highly p-doped, which will result in large losses for contact-modes. In practical terms, it is expected these not play an important role in the characteristics of the measured devices.

The electric-field amplitude of two TE quaternary modes calculated for the extremal values of h_q and n_q are shown in Fig. 5.5(a) and 5.5(b). It is apparent from Fig. 5.5(a) that if the confinement provided by the quaternary layer is low enough, the field presents a reasonable amplitude within the contact layer. Approximately 0.08% of the total power is contained in the contact region in the case depicted; nevertheless, this mode is expected to experience large propagation losses, given the high conductivity in the contact layer.

An overlap integral between the field and air holes extending down to positions y is also plotted in the figures. In both cases, the overlap is almost complete for $y < -1.1\mu m$. Considering the thickness of the top cladding and contact layer in the $h_Q = 0.35\mu$m case, the required hole depth would be $\approx 2.5\mu$m for complete overlap.

Similar calculations for TM polarization resulted in a fundamental (quaternary) mode effective index between 3.25 and 3.28. No TM contact-modes were found.

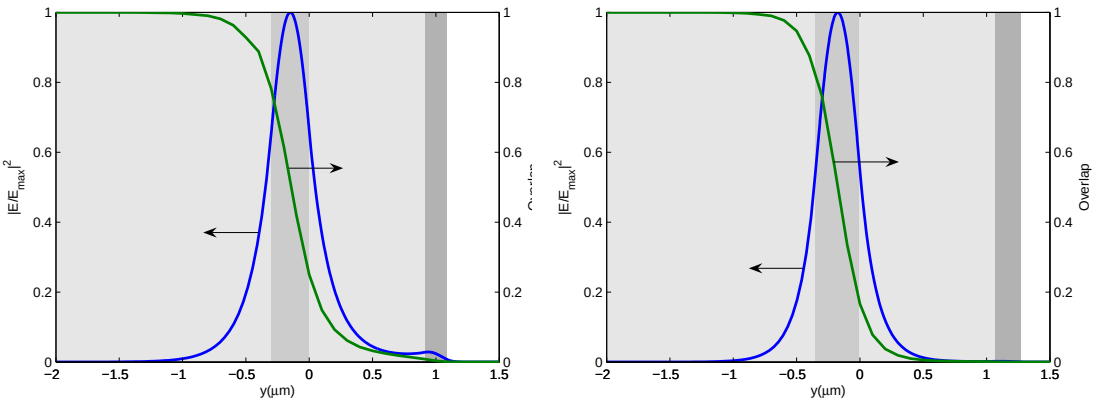

(a) (b)

Figure 5.5: Electric field amplitude-square for fundamental TE modes of slabs with (a)$h_Q = 0.30$,$n_Q = 3.4$; (b)$h_Q = 0.35$,$n_Q = 3.45$. The shaded regions correspond to the different slab layers.

5.2.3 Ridge Waveguide Modeling

Modal calculations based on a semi-vectorial 2D Beam-Propagation Method (RSoft Beamprop) were carried out considering the maximum and minimum estimated values of quaternary refractive index and thickness. The method generated quasi-TE and quasi-TM solutions of the eigenvalue equation for the major components of the electric and magnetic field in each case.

Once again, the relative dimensions of the top cladding and InGaAs layer, as well as the waveguide width with respect to the quaternary layer were obtained from SEM images. The simulated structure resembled that shown in Fig. 5.2(a), considering h_Q and h_C to be the thicknesses of InGaAsP and InGaAs layers respectively and $3.40 \leq n_Q \leq 3.45$ the quaternary refractive index. The waveguide carries 2 quaternary TE modes, examples of which are depicted in Fig. 5.6(a) and 5.6(b). No contact modes were found. Effective index curves for the two

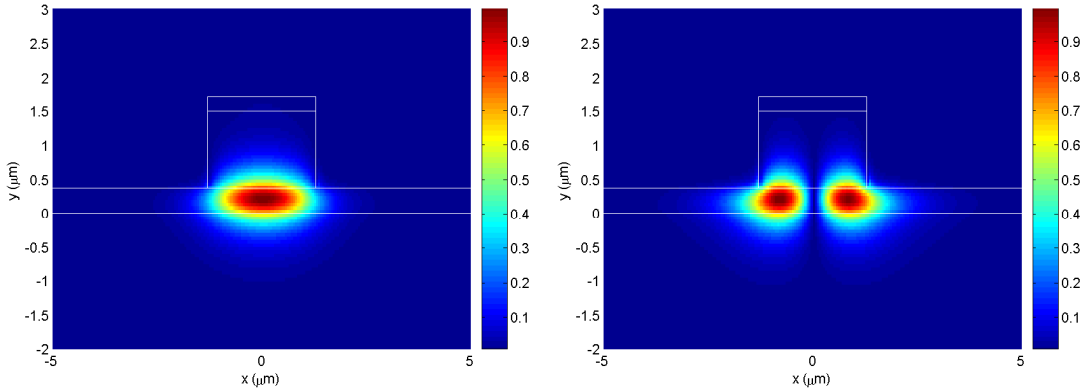

(a) (b)

Figure 5.6: Fundamental (a) and first-order TE mode field profiles (E_x component) for waveguide with $h_Q = 0.35$, $n_Q = 3.45$.

waveguide modes are plotted in Figs. 5.7(a) and 5.7(b) for extremal values of n_Q and h_Q. Given the uncertainty in the actual wafer parameters, the zero-order mode effective index is henceforth considered to be 3.246< $n_{TE,00}$ <3.30, and the second-order index 3.215< $n_{TE,01}$ <3.274. Similar calculations were used to obtain 3.237< $n_{TM_{00}}$ <3.284 and 3.20< $n_{TM_{01}}$ <3.26 for TM modes.

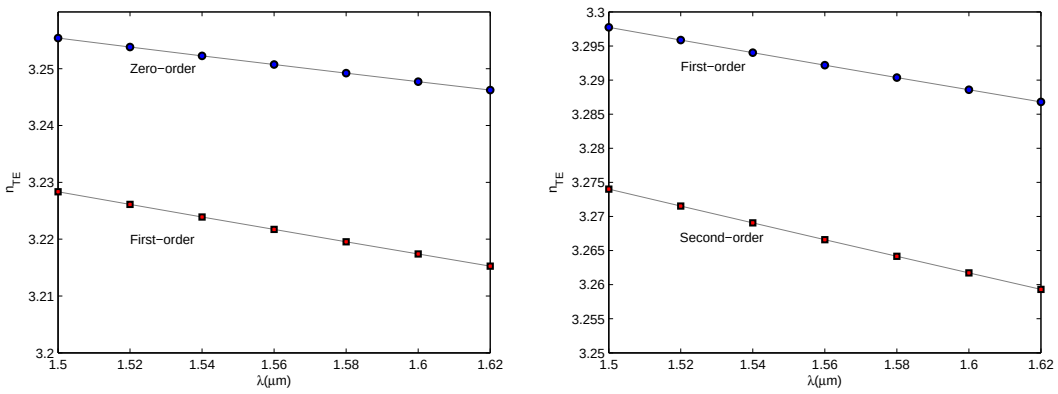

(a) (b)

Figure 5.7: Effective refractive indices for the slab waveguide in Fig. 5.3 with (a) $n_Q = 3.4$ and $h_Q = 0.3$ (b) $n_Q = 3.45$ and $h_Q = 0.35$.

5.2.4 Facet Reflectivity

Angled facets have long been employed in Traveling-Wave Semiconductor Optical Amplifiers (TW-SOA) to reduce the modal reflectivity at the semiconductor-air interfaces [1, 2]. In general, this technique is used in conjunction with Anti-Reflection (AR) coatings to yield reflectivities below 10^{-4}. It has been shown, though, that properly angled and tapered uncoated facets may yield reflectivity levels below 10^{-3}[2]. In the present work, no AR coatings were used.

An analytical expression for the effective reflectivity at a tilted facet is, considering the waveguide mode to closely resemble a Gaussian [1],

$$R_{ang}(\theta) = R_f(\theta) \exp\left[-\left(\frac{2\pi n_2 w_{full}\theta}{\lambda_0}\right)\right] \tag{5.1}$$

where θ is the angle between the incidence direction and the facet normal and R_f is the Fresnel reflectivity between two media with indices n_1 and n_2,

$$R_f(\theta) = \frac{n_1\cos(\theta) - \sqrt{1 - n_1^2\sin^2(\theta)}}{n_1\cos(\theta) - \sqrt{1 - n_1^2\sin^2(\theta)}}. \tag{5.2}$$

The reflectivity tends to decrease with increasing θ, however coupling efficiency to optical fibers decreases at large angles due to far-field beam asymmetry[1]. Increasing the waveguide width also contributes to reducing the effective reflectivity, however this might lead to the existence of high-order modes. Optimal angles for waveguide widths between 3μm and 5μm lie between 7° and 10°.

FDTD simulations were realized to probe the dependence of facet angle and waveguide width on the modal reflectivity. The waveguides considered were 2D effective-index approximations of the ridge waveguides above, considering widths

of 3μm and 5μm. The simulation consisted of launching a zero-order mode into waveguides with facet angles varying between 0° and 12°. Perfectly Matched Layers (PML)[4] were used to absorb outgoing waves. The excitation was CW at $\lambda = 1.50\mu$m and lasted long enough so that the the total reflected power (averaged over one wave-period) reached steady-state. The reflected field at the waveguide input was saved and the modal power for zero-order and first-order modes was subsequently obtained, normalized to the total reflected power. Figures 5.8(a) and 5.8(b) show the zero- and first-order mode reflectivities for waveguides of widths 3μm and 5μm. As it appears, the zero-order-mode reflectivity reaches the -30dB level at a lower angle in the second case. The zero-order reflectivity into the first-order mode is considerable in the 3-μm case, reaching the -30dB level at $\theta > 8°$; the reflectivity is more favorable in the 5-μm case, especially considering that high-order modes tend to have larger propagation losses.

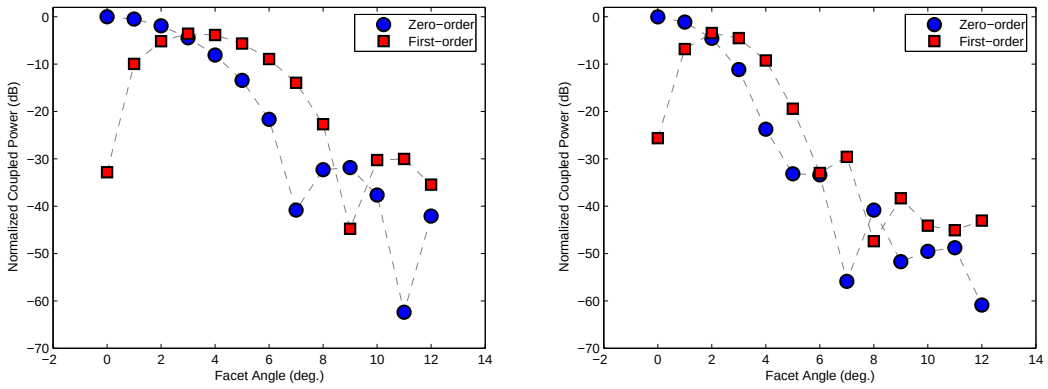

(a) (b)

Figure 5.8: Modal reflectivity for the fundamental and first-order modes for waveguide widths of (a) 5 μm (b) 3 μm.

Overall, it appears that a wider waveguide presents advantages in terms of facet reflectivity, with respect to both zero- and first-order modes. As such, a tapered-waveguide scheme was adopted in the design of the present test-structures, such that access waveguides would be tapered from 3μm to 5μm close to the cleave planes of the samples. The facet angle was chosen to be 7°. With this, it was expected that low facet reflectivities would be achieved, while maintaining a lower number of bound modes elsewhere away from the facets.

It must be noted that, given the 7° facet angle, the output beam was expected from Snell's law to exit the device at an angle of roughly 23° with respect to the facet. This means that in the experimental procedure, lensed fibers were tilted by this angle with respect to the sample facet so that coupling could be maximized.

5.3 Measurement Setup

An Agilent 81910 All-Parameter Analyzer was used to characterize the devices. The measurement system consists of a tunable, low-noise laser source together with a polarization controller and a set of high-speed photodiodes[5]. A schematic of the 81910 is presented in Fig. 5.9. A polarization controller after the tunable laser allows the instrument to record the polarization state being fed to the instrument. The polarization splitters allow for polarization-sensitive detection. Müller or Jones Matrices can be obtained using standard algorithms by making use of these features [6, 7].

The optical paths inside the instrument form Mach-Zehnder interferometers (either in transmission or reflection mode), including the device under test in one of the arms. This allows the instrument to obtain group delay measurements, based on a technique called swept-wavelength interferometry [5]. In addition, it is possible to obtain the *absolute* phase term for Jones Matrices [8].

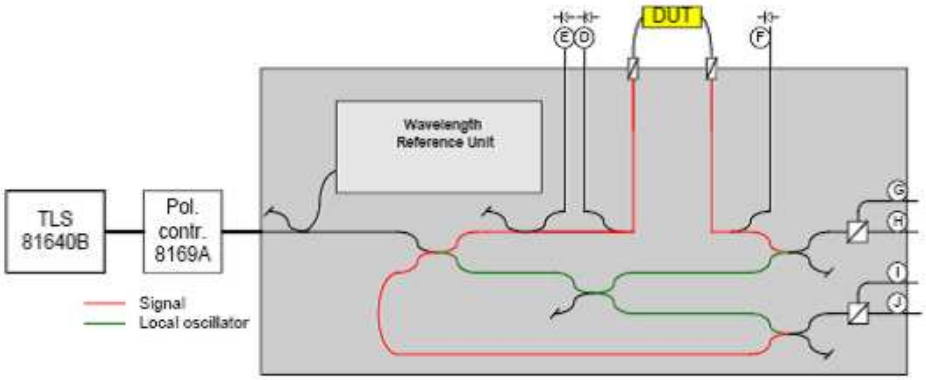

Figure 5.9: Schematic of the measurement instrument.

Coupling to the fabricated devices was done by aligning lensed fibers to the input and output waveguides; electrical contacts were biased at -2V with a Keithley 2400LV sourcemeter, and the photocurrents produced by a 0.8-mW optical signal at 1520nm were on the order of 15 A. At each measurement, after the alignment was optimized, the bias voltage was set to zero so light would suffer no extra absorption in the waveguide.

The measurement setup was built such that the sample could be rotated around its normal direction, thus allowing the beam incidence angle to be tuned, as depicted in Fig. 5.10.

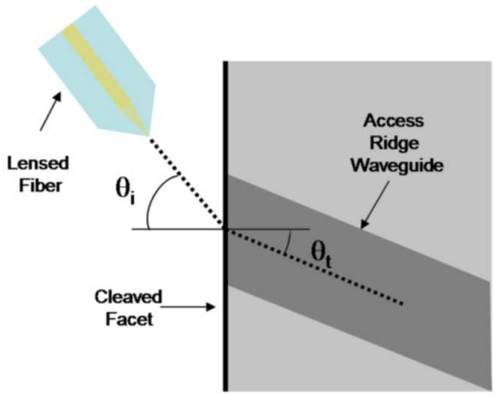

Figure 5.10: Schematic of fiber alignment to the cleaved facet.

5.4 The Müller Matrix Method

Müller matrices fully characterize polarization-dependent transmission through an optical system at fixed wavelengths, relating input and output polarization states. Their use in the present work allowed for a straightforward discernment of TE- and TM-polarized wave transmission from a single measurement run. A detailed account of Müller matrices and their properties and applications can be found in [6], however rudiments of their utilization in the context of the present work are presented next.

Stokes Vectors

The power and state of polarization of an optical wave can be represented by a 4-element vector denominated a *Stokes vector*:

$$\mathbf{S} = \begin{bmatrix} S_0 & S_1 & S_2 & S_3 \end{bmatrix} \tag{5.3}$$

The S_0 component of a Stokes vector carries the wave intensity, while the remaining components are related to its polarization state. The S_1 component describes

linear horizontal ($S_1 > 0$) or vertical ($S_1 < 0$) polarization; the S_2 component describes linear $+45°$ ($S_2 > 0$) or $-45°$ ($S_2 < 0$) polarization; the S_3 component describes right-hand circular($S_3 > 0$) or left-hand circular ($S_3 < 0$) polarization. Any polarization state on the Poincaré sphere can be described in this fashion [6]. Notice that the total power can be partially unpolarized, such that in general

$$S_0^2 \leq \sum_{i=1}^{3} S_i^2, \tag{5.4}$$

the equality being valid when the wave is completely polarized.

Müller Matrix

The Müller matrix of an optical system relates two Stokes vectors describing waves incident and scattered therefrom in the following way:

$$\mathbf{S_{out}} = M \cdot \mathbf{S_{in}} \tag{5.5}$$

M is a 4×4 matrix whose elements can be obtained through a procedure involving polarization-discriminating measurements of wave intensities at the output of the system, upon incidence of waves of specific known polarization states [6, 7]. A procedure to obtain the essential components of the Müller matrix is shown in [7].

Principal States of Polarization

The maximum and minimum transmitted powers over all polarization states can be shown to be given by [6, 7]:

$$T_{max,min} = m_{11} \pm \sqrt{\sum_{i=2}^{4} m_{1i}^2} \tag{5.6}$$

The input States Of Polarization (SOP) at which maximum and minimum transmitted power are achieved are called the *Principal States of Polarization* (PSP) and can be extracted from the Müller matrix. Consider the unit-power PSP in the form $\mathbf{S} = [1 \quad s_{\pm,1} \quad s_{\pm,2} \quad s_{pm,3}]$. Then

$$s_{\pm,i} = \pm \frac{m_{1(i+1)}}{\sqrt{\sum_{j=3}^{4} m_{1(i+1)}^2}}, \tag{5.7}$$

where the subscripts + and − are related to the maximizing and minimizing cases respectively. The above relationship is derived in [7].

It is important to note that the 81910 produces one Müller matrix at each wavelength within its measurement span.

Polarization-resolved Measurement of Test Devices

In the class of devices studied in this work, wave propagation can be quite well described in terms of two complementary polarization states: TE and TM, as if the devices were truly two-dimensional [1]. In the first case, the electric field only has components on the plane of the wafer (and no components in the propagation direction), the same being valid for the magnetic field in the latter case.

Consider the measurement of the transmission characteristics of one of the test structures described in Section 5.2. Under special conditions, the PSPs of the device can be shown to closely coincide with its TE- or TM polarizations. These conditions are exposed next.

[1] In reality, these quasi-2D structures support hybrid vector modes with very small longitudinal electric or magnetic field components. Nevertheless, quasi-TE and TM modes can be safely identified with pure two-dimensional TE or TM modes [3].

The PDL of an optical system is defined as $10\log(I_{max}/I_{min})$, where I_{max} and I_{min} are the maximum and minimum measured intensities with respect to the input polarization. The output electric field for a given device at a fixed wavelength in Jones Matrix notation is:

$$\mathbf{E}_{out} = \begin{bmatrix} j_{TE} & 0 \\ 0 & j_{TM} \end{bmatrix} \cdot \begin{bmatrix} \cos(\theta) \cdot \exp(+i\phi/2) \\ \sin(\theta) \cdot \exp(-i\phi/2). \end{bmatrix} \tag{5.8}$$

In Eq. 5.8, the first and second elements in the Jones vectors correspond respectively to the TE and TM polarizations of the device; the angles $0 \leq \theta \leq \pi/2$ and ϕ determine the relative amplitude and phase of the two components. The power at the output is proportional to

$$|\mathbf{E}_{out}|^2 = |j_{TE}|^2 \cdot \left[\cos^2(\theta) + \left| \frac{j_{TM}}{j_{TE}} \right|^2 \cdot \sin^2(\theta) + \frac{\Re\{j_{TE} j_{TM}\}}{|j_{TE}|^2} \cdot \cos(\phi) \cdot \sin(2\theta) \right] \tag{5.9}$$

For very small $|j_{TM}/j_{TE}|$, the second term inside the brackets can be ignored, leaving an expression that can be maximized or minimized when θ satisfies

$$\tan(2\theta) = 2\frac{\Re\{j_{TE} j_{TM}\}}{|j_{TE}|^2} \cdot \cos(\phi) \leq 2\left| \frac{j_{TM}}{j_{TE}} \right|. \tag{5.10}$$

Since $|j_{TM}/j_{TE}|$ is small, the maximum and minimum output powers will be found respectively at $\theta \approx 0$ and $\theta \approx \pi/2$, corresponding approximately to purely TE- and TM-polarized vectors.

In summary, the PSPs of a test device will be aligned with its TE or TM polarizations whenever a large PDL is observed. In general, the tested devices show a considerable degree of PDL variation along the full measurement wavelength

span; large PDL is most times observed within specific wavelength ranges only. Nevertheless, TE- or TM- transmission curves for the entire wavelength span can be obtained once the the assumption is made that the SOP at the tunable source output [2] are wavelength-independent and so is the degree of polarization rotation along the fibers connecting instrument and device. In this case, the PSPs at a high-PDL wavelength can be obtained and re-applied to the Müller matrices at all other wavelengths to yield TE and TM transmitted powers.

To verify the validity of this assumption, the power transmission spectra for a single-line-defect photonic crystal waveguide was analyzed using the technique described above. The waveguide displayed a photonic band-gap for TE modes for wavelengths above $\lambda \approx 1.6$ and no TM-mode band-gap. Figure 5.11 shows the obtained maximum and minimum power transmission curves T_{max} and T_{min}, the PDL and the vector components of the maximizing PSP, $s_{+,i}$, $i = 1, 2, 3$. The PDL reaches values above 20dB for $\lambda \gtrsim 1.6\mu$m, where the TE band-gap is found. The T_{max} and T_{min} curves meet at $\lambda_0 \approx 1.587\mu$m, where PDL$(\lambda_0) \approx 0$. Notice that the maximizing PSP remains roughly constant everywhere except in the vicinity of λ_0; also, it appears to change abruptly from one state to another at this point. At shorter wavelengths than λ_0, the TE polarization maximizes transmission; at longer wavelengths, the TM polarization does. It is apparent the SOP of the tunable laser output is independent of wavelength and so is the polarization rotation experienced though the fiber path connecting the instrument to the devices. Of course, the fiber paths should be kept fixed in position as much

[2] Actually, at the output of the polarization controller that follows the tunable source.

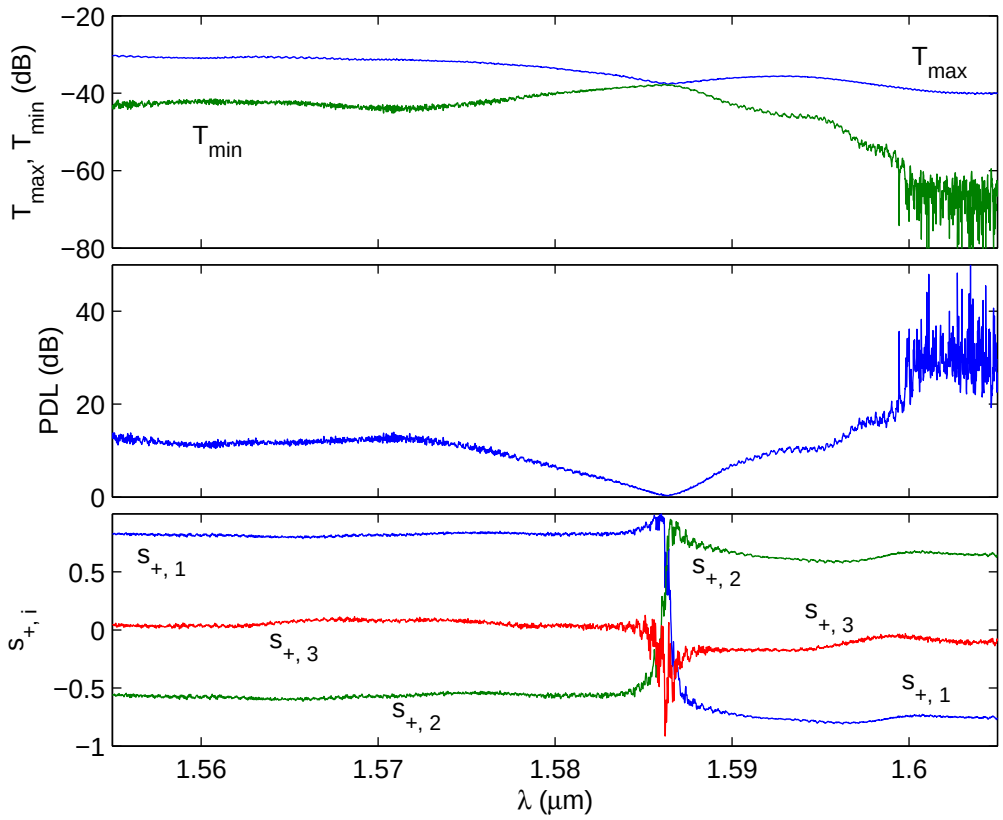

Figure 5.11: Power transmission, PDL and power-maximizing PSP vector components for a single-line-defect PC waveguide.

as possible during each set of measurements, so that approximately the same states of polarization are being launched each time.

Applying the PSP at $\lambda = 1.62\mu$m to the Müller matrices at all other wavelengths produces the TE and TM curves shown in Fig. 5.12(a). The same done with a PSP at $\lambda = 1.5$ yields the curves in Fig. 5.12(b). Notice that the two sets of curves are very similar, despite the fact the PDL in the first case was 10dB higher than in the second. The difference between the two cases in fact remained below 10% except in the bandgap region for TE modes, where the amplitude becomes extremely low. This seems to indicate that PDL$\gtrsim$ 10dB still generates acceptable curves.

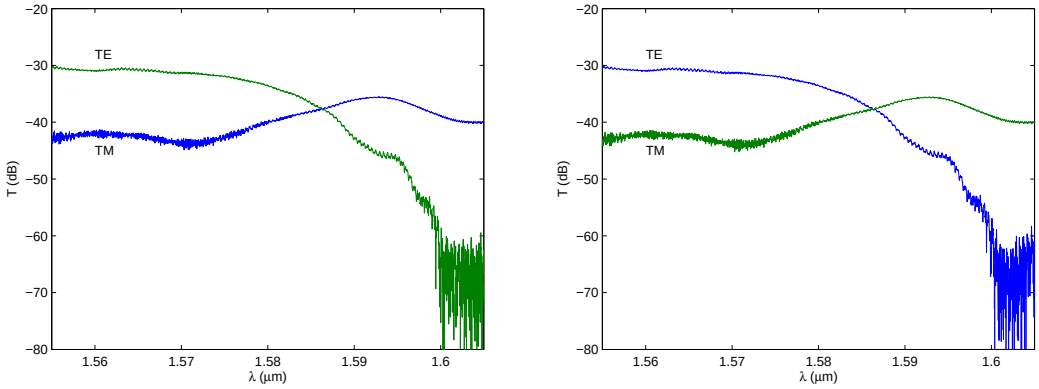

(a) (b)

Figure 5.12: TE and TM power transmission for the single-line-defect waveguide using respectively (a) maximizing and the minimizing PSP at $\lambda = 1.62\mu$m and (b) minimizing and maximizing PSP at $\lambda = 1.50\mu$m.

5.5 Jones Matrices

Jones matrices provide an alternative way of describing polarization-related phenomena, being closely related to the Müller matrices. The SOP vectors in this case are complex and two-dimensional, as opposed to real and 4-dimensional in the previous case; a Jones matrix, as a result, is $2\times$ and complex. The Jones vector components relate to two reference (not necessarily perpendicular) axes [9], their relative magnitures and phases describing a particular SOP. Notice that this formulation does not allow for the description of unpolarized or partially polarized light.

The Jones matrix of an optical system can be obtained experimentally through a series of polarization-resolving measurements with specific exciting SOPs [8, 10,

11]. The resulting matrix is in the form

$$M = \beta \begin{bmatrix} k_1 k_4 & k_2 \\ k_4 & 1 \end{bmatrix}, \tag{5.11}$$

where k_1, k_2, k_4 are normalized quantities directly obtained from the measurements. The β term describes both absolute amplitude and phase of the system; determination of the absolute amplitude can be straightforwardly obtained from the k-parameters:

$$|\beta|^2 = \frac{T_1}{|k_4|^2(1+|k_1|^2)} = \frac{T_2}{1+|k_2|^2}, \tag{5.12}$$

where T_1 and T_2 are measured in the k-value determination steps [8]. Determination of the absolute phase is more involved, in general requiring an interferometric experiment whereby relative fringe displacements can be measured. In the 81910, this is in fact realized by analysis of fringe patterns from the built-in Mach-Zehnder interferometer.

Principal States of Polarization

The PSPs of an optical system can be computed from its Jones matrix in the following way. Let H be a 2×2 matrix and $\mathbf{s}$ a general Jones vector. Next define the inner product $(\mathbf{s}, \mathbf{s}) = \mathbf{s}^{*T} \cdot \mathbf{s}_2$ and consider $(\mathbf{s}, \mathbf{s}) = 1$. If H is Hermitian, it is straightforward to show that the quantity $f = (H\mathbf{s}, \mathbf{s})$, called the *field-of-values* of H, is bounded within the Real interval $\lambda_1 \leq f \leq \lambda_2$, where $\lambda_{1,2}$ are eigenvalues of H [3]. The transmitted power of a system described by a Jones matrix J can be

[3] Since H is hermitian, its eigenvalues are real.

expressed as

$$T = (J\mathbf{s}, J\mathbf{s}) = (J^{*T}J\mathbf{s}, \mathbf{s}). \tag{5.13}$$

The matrix $H = J^{*T}J$ is Hermitian. The transmission T above is the field-of-values of H; thus finding the maximal and minimal transmitted powers and their corresponding PSPs requires simply finding the eigenvalues and eigenvalues of H. What is more, its eigenvalues λ_i, $i = 1, 2$, correspond to the *singular values* of the Jones Matrix J [4] which can be proved to be invariant under unitary transformations [12]. This means that the polarization rotation introduced by anything (i.e. optical fibers) in the paths between source and system and system and detector do not alter the results, as far as maximum and minimum transmission are concerned.

Group Delay and Differential Group Delay

Consider the Jones vector $\mathbf{y}$ obtained from a unitary Jones vector $\hat{\mathbf{x}}$:

$$\mathbf{y}(\omega) = J(\omega)\hat{\mathbf{x}}(\omega) = y(\omega)e^{i\phi(\omega)}\hat{\mathbf{y}}(\omega), \tag{5.14}$$

The frequency dependence of the matrix and vectors has been made explicit. Differentiating this with respect to ω, the following expression is obtained:

$$\mathbf{y}_\omega = T_\omega\hat{\mathbf{x}} = \left(\frac{y_\omega}{y} + i\phi_\omega\right)\mathbf{y} + ye^{i\phi}\hat{\mathbf{y}}_\omega. \tag{5.15}$$

If $\mathbf{y}$ is an output PSP of the system [5], it can be shown to be invariant to first order with respect to ω [13]. As such, the second term on the right can be set

[4] The singular values σ_i of a matrix J are defined such that σ_i^2 is the i-th eigenvalue of $J^{*T}J$. In mathematical formulation, $\sigma_i^2 = \lambda_i\{J^{*T}J\}$.

[5] $\hat{\mathbf{x}}$ would then be an input PSP.

to zero. The term $\tau_g = \phi_\omega$ is the group delay of the PSP described by $\hat{\mathbf{y}}$. Since $\hat{\mathbf{x}} = J^{-1}\hat{\mathbf{y}}$ (considering J non-singular), from Eq. 5.15,

$$ye^{i\phi}\hat{\mathbf{y}}_\omega = 0 = \left[J_\omega J^{-1} - \left(\frac{y_\omega}{y} + i\tau_g\right)\right]. \tag{5.16}$$

Thus the imaginary parts of the eigenvalues of $J_\omega J^{-1}$ correspond to the group velocities of the two PSPs of the optical system. The PSPs can thus be identified with the fast and slow axes of the system, depending upon their respective group delays.

Group Delay (GD) is defined as $GD = (\tau_{g,max} + \tau_{g,min})/2$, while Differential Group Delay (DGD) is defined as $DGD = |\tau_{g,max} - \tau_{g,min}|$. The Polarization Mode Dispersion (PMD) of the system is a vectorial quantity obtained by multiplying the DGD to the (unitary) slow input PSP vector.

It must be noted that the two group delays can only be found independently if the absolute phase of the system is known. If this is not possible, GD and DGD can still be obtained from an approximation to Eq. 5.16, as described in [11].

5.6 Fiber-to-Waveguide Coupling

Due to the multi-mode nature of the ridge waveguides, power coupling into high-order modes can occur to significant levels upon excitation with a lensed fiber. This becomes an issue when tilted waveguide facets are employed such as described in section 5.2.4, since beam incidence at an $\approx 23^\circ$ angle with respect to the facet is required for optimal power collection. Departure from the optimal collection angle leads to coupling into the high-order mode. This can be shown

by a series of FDTD simulations based on the scheme in Fig. 5.13. The procedure consists of launching a Gaussian 7°-tilted semiconductor facet at varying angles and measuring the power coupled to individual waveguide modes. In the present case, the Gaussian beam waist was considered to be 5μm at a distance of 1μm from the center of the waveguide. This choice was made since the lensed fiber used in the experiments had been specified with a 5μm spot-size. The waveguide width was 5μm.

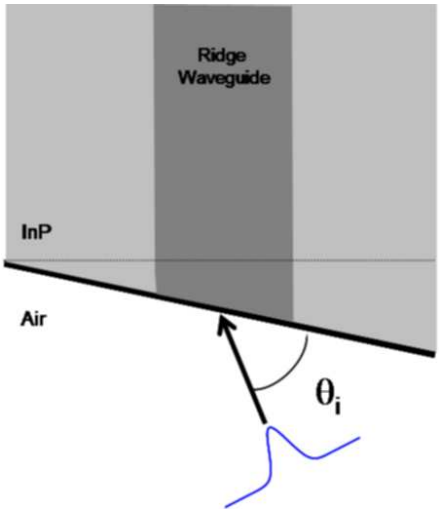

Figure 5.13: Schematic of simulated structure.

Figure 5.14 shows the power coupled to the fundamental and first-order modes with respect to the total power immediately inside the semiconductor medium. Clearly, the optimum incidence angle is 23°, where maximum power is coupled to the fundamental mode; at the same time, the second-order mode power is minimized, going close to -20dB. Within a ±3°, the fundamental mode power remains 10dB above that of the second-order mode.

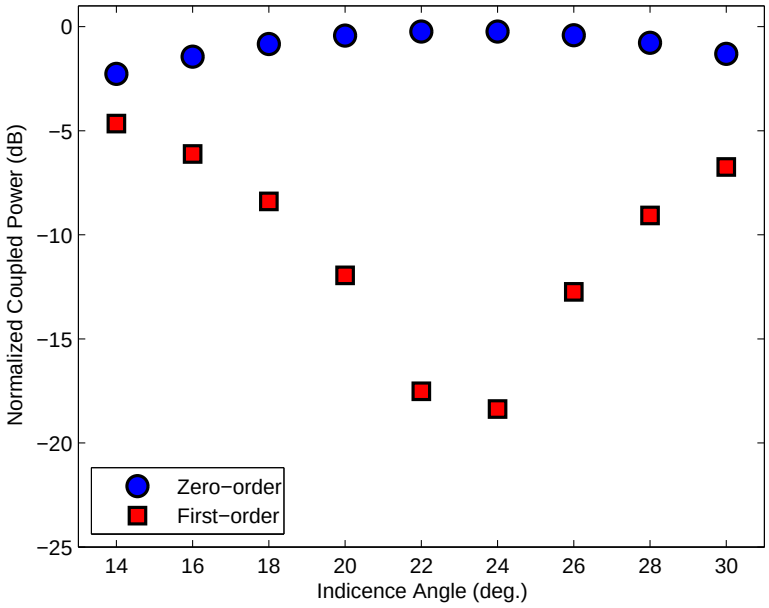

Figure 5.14: Power coupled to fundamental and first-order mode for varying incidence angles.

Experimental Verification

The amount of power coupled to the second-order mode can be estimated by analyzing fringes on the transmission power spectrum. Consider the excitation of a ridge waveguide of length L with a lensed fiber and the collection of the output beam by an identical fiber such that the ridge-to-fiber coupling can be assumed to be reciprocal for both modes. Two propagation modes will be excited in the ridge waveguide, sharing the total guided-light power. To first order, the field at the output of the guide can be described by [6]

$$E_{out} = a_1 \exp\left(-i\frac{\omega}{c}n_1 L\right) + a_2 \exp\left(-i\frac{\omega}{c}n_2 L\right), \tag{5.17}$$

[6] Assuming the collected power to be exclusively from the two guided modes.

where a_1 and a_2 are related to the transmission coefficients of the two modes. The optical power will be proportional to

$$|E_{out}|^2 = |a_1|^2 + |a_2|^2 + 2 \cdot \Re\{a_1 a_2\} \cos\left(\frac{\omega}{c}\Delta n \cdot L\right) \tag{5.18}$$

This function is periodic with respect to ω. The argument of the cosine can be expanded as $\phi \approx \phi(\omega_0) + \partial\phi(\omega_0)/\partial\omega\Delta\omega$, such that

$$\frac{\partial\phi}{\partial\omega} = \frac{L}{c} \cdot \Delta n_g, \tag{5.19}$$

with Δn_g the difference between the group indices of the two modes[7]. The group index difference can be obtained from the oscillation period by setting $\Delta\phi = \phi(\omega_1) - \phi(\omega_0) = 2\pi$ and using Eq. 5.19:

$$\Delta n_g = \frac{\lambda^2}{L \cdot \Delta\lambda}. \tag{5.20}$$

Here, $\Delta\lambda$ is the oscillation period in terms of wavelength, obtained from the relation $\Delta\omega = -2\pi c/\lambda^2 \cdot \Delta\lambda$.

Defining $x = a_2/a_1$, the following expression gives the field extinction[8]:

$$\left(\frac{E_{out,max}}{E_{out,min}}\right)^2 = \left(\frac{1+x}{1-x}\right)^2. \tag{5.21}$$

The extinction is larger for waves of compatible power levels. A plot of the extinction versus the factor x^2 is shown in Fig. 5.15. Notice that fringes with approximately 1dB extinction correspond to a secondary (weaker) signal 20dB below the main wave. The measurement setup was built such that the sample could be rotated around its normal direction, thus allowing the beam incidence angle to

[7]The group index is defined as $n_g = n + \omega\partial n/\partial\omega$.
[8]It is considered that $0 \leq x \leq 1$.

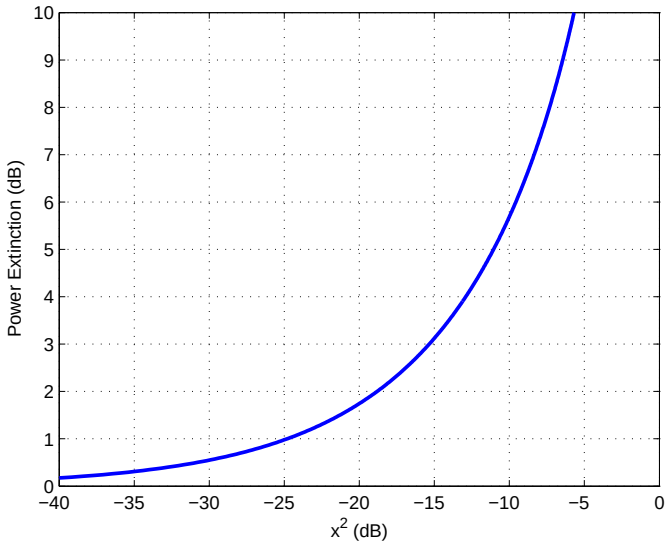

Figure 5.15: Power extinction due to the interference of two waves as a function of the relative power between the two.

be tuned, as depicted in Fig. 5.10. In practice, previously to the measurement of the PC structures, transmission spectra of a reference waveguide were obtained at various incidence angles, so that a sufficient tilt could be found that would reduce the power coupled to the high-order access waveguide mode to an acceptable level

.

Figure 5.16 shows representative transmitted power spectra obtained for 17° and 25° incidence. In the former case, large fringes are observed, with dips spaced by $\approx 66nm$. From Eq. 5.20, this corresponds to a group-index difference $0.024 < \Delta n_g < 0.026$, compatible with the phase-index difference between the two first waveguide modes. The oscillation amplitude is of approximately 6dB, corresponding to a ratio of ≈ -5dB between second- and first-order mode powers. In the 25° angle case, the transmission spectrum varies within a 1dB

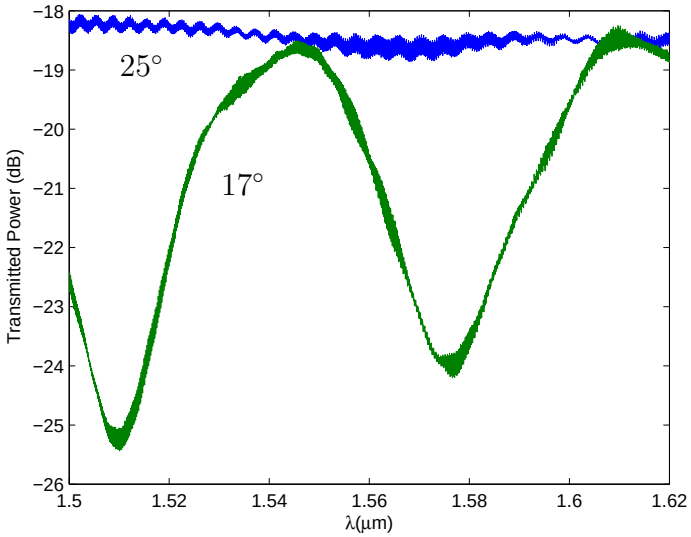

Figure 5.16: Ridge waveguide transmitted power for incidence angles of 17° and 25°.

interval, corresponding to a second-order mode power about 25dB lower than the first-order mode power.

5.7 Summary and Conclusions

The experimental technique used to characterize Photonic Crystal (PC) structures in the present work was described in detail in this chapter.

Standard test-structures were devised for the measurement of PC properties, consisting of mesas connected to access ridge waveguides: each mesa carried one particular PC pattern and light was inserted and extracted from the PCs through the access guides. The test-structures were general enough to allow various types of PC patterns to be defined and characterized. Coupling of light into and out of the test structures was realized through lensed fibers. The alignment procedure

was very simple and fast, not requiring any free-space optics, and offered a high level of repeatability.

A calculation of the bound modes of the slab waveguides formed at mesa regions was carried out considering sensible ranges for waveguide layer thicknesses and refractive indices. Later chapters confirm the validity of the refractive index ranges found in the present calculations. Modal calculations for the access ridge waveguides revealed that these present two laterally-bound modes. Given their multi-mode nature, special care is necessary for fiber-to-waveguide alignment, as explained in the text, so that most power may be coupled to the fundamental mode.

The measurement system, which included an Agilent 81910 All-Parameter Analyzer, allowed the characterization of test devices in terms of Müller and Jones matrices, which constitute very powerful tools for the analysis of quasi-2D PCs. Müller matrices yield, within one measurement run, information about the polarization-dependent behavior of the devices without the necessity of knowing the exact polarization state at its input and output; Jones matrices allow, additionally, the determination of the device phase response. In summary, the two matrices yield the complete device amplitude and phase responses, including polarization dependence, in a very accurate and simple way. Important aspects of Müller and Jones matrix analysis as applied to TE and TM polarization-resolved measurements, as well as Group Delay (GD) and Differential Group Delay (DGD) measurements were included in the text.

Finally, it is important to point out that, although the fabrication of the test-structures is quite involved, the present measurement technique allows for the accurate and complete measurement of polarization-dependent amplitude and phase transfer functions of PC structures in a very simple and accurate way.

References

[1] M. J. Connelly, *Semiconductor Optical Amplifiers*. Dordrecht, The Netherlands: Kluwer, 2002.

[2] C. E. Zah, R. Bhat, S. G. Menocal, N. Andreakis, F. Favire, C. Caneau, M. A. Koza, and T. P. Lee, "1.5μm GaInAsP angled-facet flared-waveguide traveling-wave laser amplifiers," *Photon. Tech. Lett.*, vol. 2, no. 1, 1990.

[3] L. A. Coldren and S. W. Corzine, *Diode Lasers and Photonic Integrated Circuits*. New York: Wiley-Interscience, 1999.

[4] A. Taflove, *Computational Electrodynamics - The finite-difference time-domain method, 2nd edition*. Norwood, Massachussets: Artech House, 2000.

[5] T. Jensen, E. Witzel, A. Paduch, P. Ziegler, E.U.Wagemann, and O. Funke, "A new method to determine loss, PDL, GD and DGD of passive optical components," *18th NFOEC, Dallas*, p. 14621470, 2002.

[6] E. Collett, *Polarized Light in Fiber Optics*. Lincroft, N.J.: The PolaWave Group, 2003.

[7] K. Yamaguchi, M. Kelly, G. Stolze, and D. Kobasevic, "Polarization-resolved measurements using Mueller matrix analysis," *Agilent Application Note 5989-1261EN*.

[8] R. C. Jones, "A new calculus for the treatment of optical systems. vi. experimental determination of the matrix," *J. Opt. Soc. Amer.*, vol. 37, pp. 110–112, 1947.

[9] A. Yariv, *Optical Electronics*. Fort Worth: Saunders College Printing, 1991.

[10] B. L. Heffner, "Accurate, automated measurement of differential group delay dispersion and principal state variation using jones matrix eigenanalysis," *Photon. Technol. Lett.*, vol. 5, pp. 814–817, July 1993.

[11] B. L. Heffner, "Automated measurement of polarization mode dispersion using jones matrix eigenanalysis," *Photon. Technol. Lett.*, vol. 4, pp. 1066–1068, September 1992.

[12] G. Strang, *Linear algebra and its applications*. Thomson, Brooks/Cole, 4th ed.

[13] C. D. Poole and R. E. Wagner, "Phenomenological approach to polarisation dispersion in long single-mode fibers," *Elect. Lett.*, vol. 11, no. 10, 1986.

Chapter 6

Experimental Results

In this chapter, the experimental characterization of four different PC structures is reported.

In the first section, a short (10μm) rectangular lattice of holes is investigated that provides a low-pass transmission transfer function with relatively low insertion loss and a 20dB stop-band extinction. Lattices with 7°-9° tilt angles are realized in an attempt to reduce back-reflections. This extremely compact filter structure could find application as a rejection filter for the entire L- optical communications band.

In Section 6.2, a three-line-defect waveguide realized in a triangular lattice (denominated $W3^{(M)}$) that presents a band-gap for TM polarization is characterized for power transmission and reflection, as well as transmission group delays. A small group delay enhancement is observed at the band-gap edges, together with very high group velocity dispersion over a bandwidth of about 1nm.

Section 6.3 deals with a series of asymmetric multi-mode line-defect waveguides offering transmission stop-bands that could be conveniently used for broadband notch filtering. Multi-mode propagation is shown to considerably affect the trans-

mission transfer function of shorter-length waveguides, in terms of stop-band extinction and pass-band distortion.

Finally, Section 6.4 presents the characterization of a single-mode, single-line defect PC waveguide in the Γ-K direction of a triangular lattice. Extremely short waveguide lengths are shown to produce a very large stop-band extinction and relatively high group delays.

6.1 Photonic Crystal Rectangular Lattice Filter

Extremely compact Photonic Crystal (PC) microcavity filters for optical communications have been proposed and demonstrated, with promising results [1] for employment in monolithic Photonic Integrated Circuits (PIC). The wide bandwidths achieved offer good prospects for applications in coarse DWM (CDWM) systems. One of the main difficulties however in introducing such structures in one of the paths of a PIC that includes an internal light source [2] is in reducing the power level of reflected waves that could be fed-back to the source thereby causing laser mode instability and linewidth deterioration [3].

In this section, a 10-μm-long, broadband PC grating filter with reduced back-reflection levels is demonstrated that could be used for rejection of entire optical-communications bands. The reflection-mitigation technique consists in tilting the grating with respect to the input waveguide by a few degrees, as illustrated in Fig. 6.1, thereby reducing the coupling back into the fundamental mode of the input waveguide. A similar scheme is widely used to reduce the facet reflectiv-

ity of traveling-wave semiconductor optical amplifiers [4, 5]. Each period of the present grating filter was formed by removal of three rows of holes from a bulk triangular lattice-of-holes PC in the Γ-M crystal direction as illustrated in Fig. 6.5. The resulting pattern is a rectangular array of holes, spaced by a in lateral di-

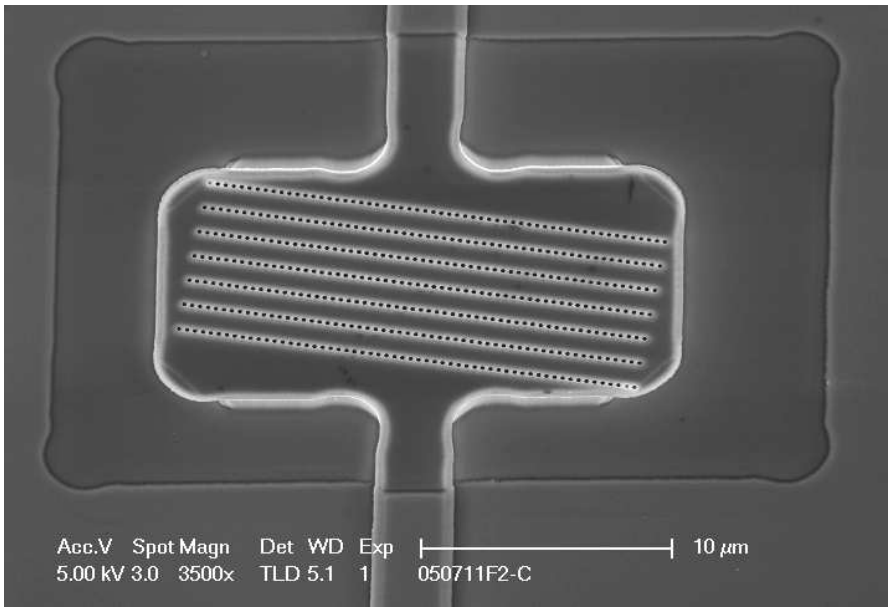

Figure 6.1: SEM image of fabricated PC pattern on top of $20\mu m \times 10\mu$m mesa.

rection and by $2\sqrt{3} \cdot a$ in the longitudinal direction, as illustrated in Figs. 6.2(a) and 6.2(b). This structure was chosen based on the assumption that the single rows of holes forming the grating mirrors would cause very low overall out-of-crystal-plane radiation losses as well as very little distortion to incident beams, resulting in more efficient wave interference and therefore better filter transfer functions. The original bulk PC has been shown to present a large ($> 80\%$) reflectivity in the band-gap region [6]. It is worth mentioning that the filter was designed having in mind a PIC based on weak-confinement waveguides [2], such that bound modes were expected to extend a couple of microns outside of the

guiding region. This required a laterally wide structure such as shown in Fig. 6.1; the same concept could nonetheless be applied to strong waveguides, as realized in [1].

At the time of the investigation, it was desired to use a partially fabricated wafer with test structures including 10-μm-long mesas. This limited the maximum number of periods to 6 so that gratings could fit within the mesa length.

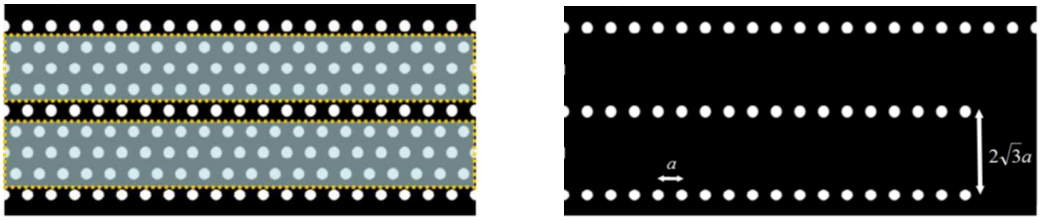

(a) (b)

Figure 6.2: (a) Bulk triangular lattice of holes PC. Holes within the dotted regions are suppressed to form the grating shown in(b).

6.1.1 Experimental Filter Characteristics

Sets of devices with four different tilt angles were fabricated with lattice constant $a = 300$nm. Each set encompassed four similar patterns with slightly varying filling fractions (estimated to be between $r/a = 0.22$ and $r/a = 0.26$ from SEM images). Figures 6.3(a) and 6.3(b) show transmitted and reflected power for devices with 0-degree tilt angle and various radii. The extinction is close to 20dB and the passband-edge is close to $\lambda = 1.54\mu$m. Notice the displacement of the passband edge toward shorter wavelengths with increasing hole radius, accompanied by displacement of the reflectivity dips. The latter correspond to resonances in the transmission pass-bands and result from a fairly efficient wave interference.

The transmission spectrum for a ridge waveguide is also plotted; comparison between this and the grating curves indicate an insertion loss of roughly 3dB at $\lambda = 1.50\mu$m. Given the repeatability of the pass-band power levels, this value is believed to be a good estimate of the insertion loss. Reflectivity maxima range

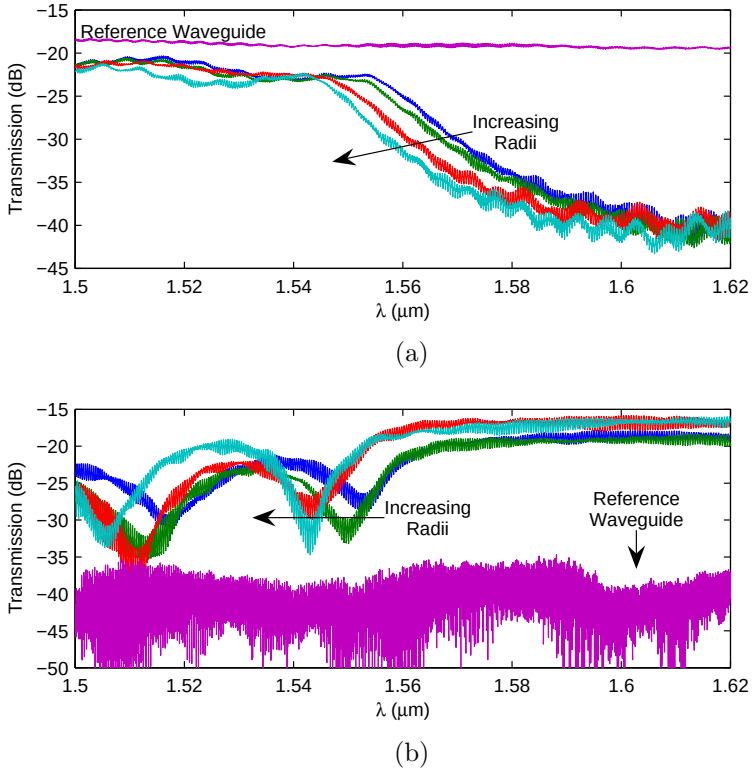

Figure 6.3: (a) Power rransmission for gratings with $a = 300$nm and varying r/a ratios. (b) Corresponding power reflection. Curves for a reference straight waveguide are also shown.

between -22 and -17dB, appearing at times to reach above the transmitted power level. This is due to a small difference in the fiber-to-waveguide coupling efficiencies between the two access waveguides. The reference waveguide reflectivity power level is reasonably high. This is most likely due to the finite modal reflec-

tivity at the semiconductor-air interfaces, as evidenced by the large $\approx$ 0.02-nm-period [1] Fabry-Pérot resonances.

Transmission and reflection curves of tilted gratings are shown in Figs. 6.4(a) and 6.4(b). One un-tilted grating curve is also shown for comparison, as well as one from a reference ridge waveguide. A moving-average filter was used to smooth the tilted-grating reflectivity curves, which had large 0.04-nm-period Fabry-Pérot resonances. In terms of power transmission, the stop-band is in total between 15dB and 20dB lower than the pass-band. The insertion loss at the pass-band seems to suffer little from the tilting, remaining below 5dB. Notice that the transmitted power within the stop-band tends to move up with increasing wavelengths. This is due to the existence of an additional pass-band at wavelengths above $\lambda = 1.55\mu$m, given that the transfer function is periodic in ω. It is apparent that the 9° curve presents the worst extinction, insertion loss and sharpness.

The reflectivity curves for tilted gratings do not present the same prominent features of the un-tilted case (i.e. reflectivity dips and side-lobes). The large (approximately 20dB) variation in transmitted power finds no corresponding variation in the reflected power characteristic, indicating an efficient suppression of the modal reflectivity. Reflected power levels remain between 13dB and 20dB below the un-tilted grating reflectivity and between 5 and 10dB above the reference waveguide level. It is apparent that the 7°-angle grating presents an overall higher reflectivity, while the 9° case seems to display the lowers power levels over a wider bandwidth.

[1] Corresponding to a length of $\approx$ 1.5mm.

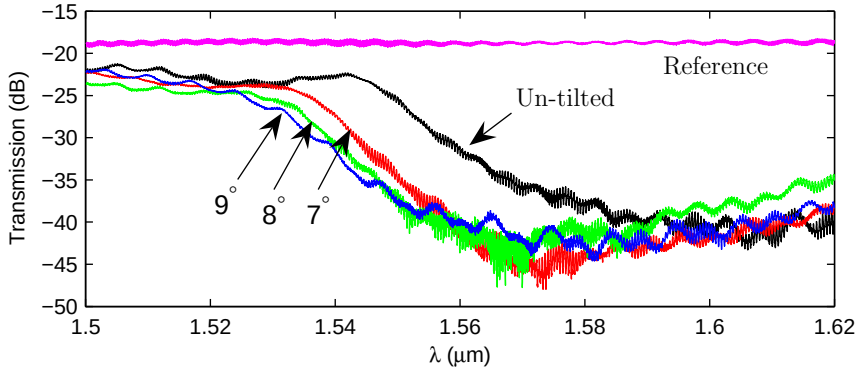

(a)

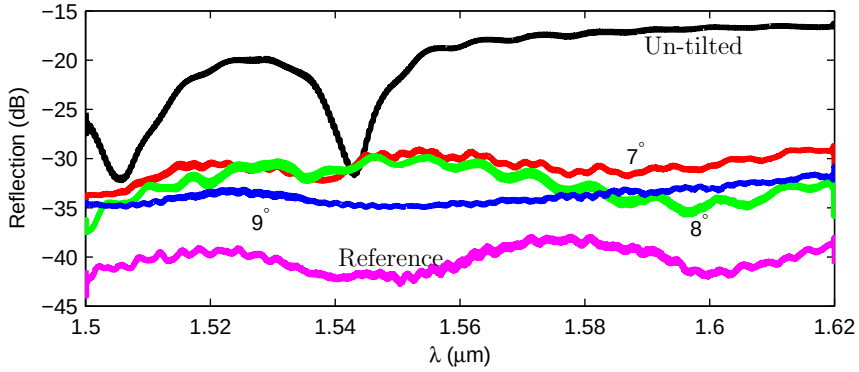

(b)

Figure 6.4: (a) Power transmission for gratings with a = 300nm and varying r/a ratios. (b) Corresponding power reflection. Curves for a reference straight waveguide are also shown.

Mesas are not expected to considerably affect the measured PC power transmission characteristics. Mesa lengths are sufficiently short for multimode interference effects to be negligible: the beat length between the two lowest order mesa modes is estimated to be larger than 1mm, since mesa widths are of 20μm [7]. Regarding mesa reflectivity, the effective index step between ridge waveguide and mesa can be estimated to be below 0.1, from which a maximum reflection coefficient of 0.01 can be estimated, or a reflectivity of 10^{-4}. The reflectivity of the reference ridge guide in Fig. 6.4(b) is of roughly 0.01 (≈-20dB, compared to the

grating reflectivity), considerably higher than that of the waveguide-mesa interface. As such, mesas are expected to contribute very little the measured filter reflectivity. This of course does not mean that future filter designs should not include changes to the waveguide-mesa interface for reduced reflectivity.

Figures 6.5(a) and 6.5(b) show respectively measured power transmission and reflection spectra for a mesa not containing any PC pattern and a reference, straight ridge waveguide. As expected, very little difference is observed between the two sets of curves.

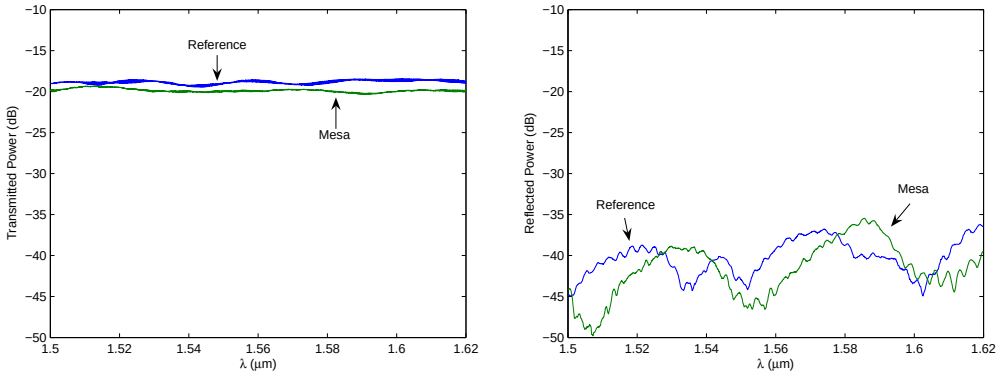

(a) (b)

Figure 6.5: Power transmission (a) and reflection(b) for a reference, straight ridge waveguide and a black 10-μm-long mesa.

6.1.2 Device Simulation

Finite-Differences Time-Domain (FDTD) simulations were realized in an attempt to explain the observed features. Simulated structures included the 10-μm mesas and small portions of both input and output waveguides such that reflections from the mesa-waveguide discontinuities could also be taken into account.

Refractive indices for the ridges and mesa and surrounding regions were those of first TM-mode effective indices calculated for the vertical epi-structure at the corresponding regions. Absorption losses and those caused by out-of-plane radiation were considered to be null.

Figure 6.6 shows transmitted and reflected power spectra for gratings with lattice constant $a = 300$nm, hole radius $r = 0.24a$ and four different tilt angles. Once again, the un-tilted grating transmission spectrum presents clear resonant peaks. The minimum transmitted power within the stop-band ($\lambda >$ 1.56μm) is approximately -20dB. The reflectivity is very large within this range, approaching -1dB. This is however drastically reduced for tilted gratings, for which it remains below -30dB in the 8° and 9° angle cases. The transmission stop-band extinction remains all the same close to -20dB. The passband-edge roll-off is roughly the same as for the case with no tilt, with power decreasing by roughly 15dB in 20nm. Due to a less efficient wave interference, the original pass-band resonances are subdued and transmission decreases monotonically to the -3dB point close to $\lambda = 1.54\mu$m; the insertion loss at the maximum transmission point at $\lambda = 1.50\mu$m is 1.5dB. Notice also the slow increase in transmitted power for larger pass-band wavelengths, a feature clearly observed in the experimental results.

It is important to point out that a light beam experiences diffraction within each grating period and is slighted distorted upon incidence at the holes. Part of the resulting output beam power will not couple to the output guide fundamental mode, adding to the insertion loss. At the same time, part of the incident power is carried by waves that travel laterally in the grating cavities, due to the lack of

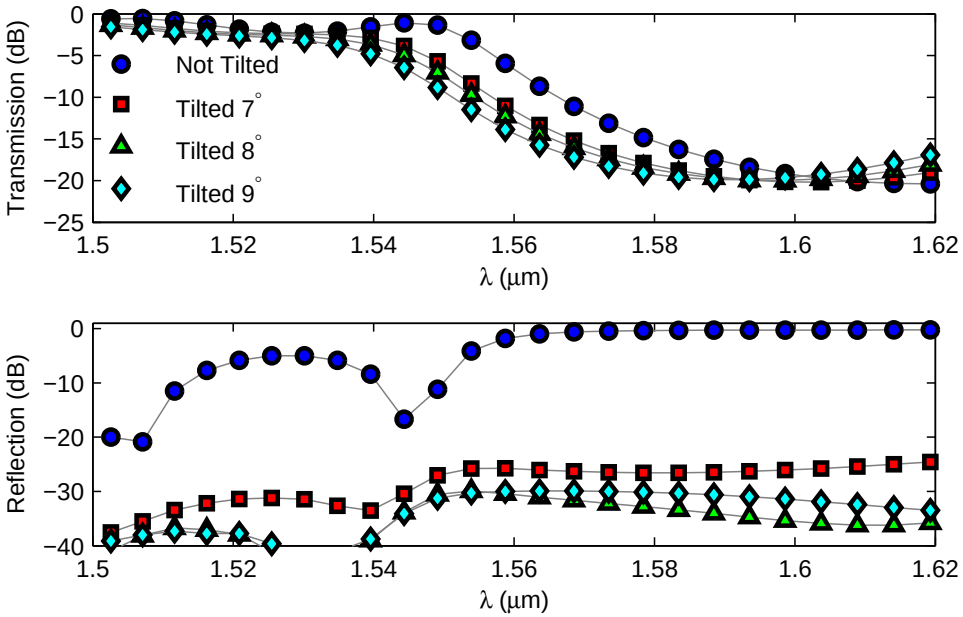

Figure 6.6: Finite-Differences Time-Domain simulation of gratings with $a = 300$nm, $r/a = 0.24$ and different tilt angles.

a lateral confinement mechanism. This can be clearly observed in Fig. 6.7, which shows the field distribution, obtained with FDTD, resulting from incidence upon an 8° grating with $r/a = 0.24$ at $\lambda = 1.5\mu$m (within the passband). The time step in which this distribution was collected is such that both averaged reflected and transmitted powers had reached steady-state.

Enhanced filter characteristics can be achieved by tuning the hole dimensions, as shown in Fig. 6.8. Increased radii lead to enhanced stop-band extinction, in detriment of passband roll-off. The band-edge shifts towards lower wavelengths with increasing radii, an effect clearly observed in the experimental curves. The enhanced extinction can be explained by an improved effective reflectivity obtained from larger holes: Figure 6.9 shows the simulated reflected and transmitted powers for one row of holes of varying radii.

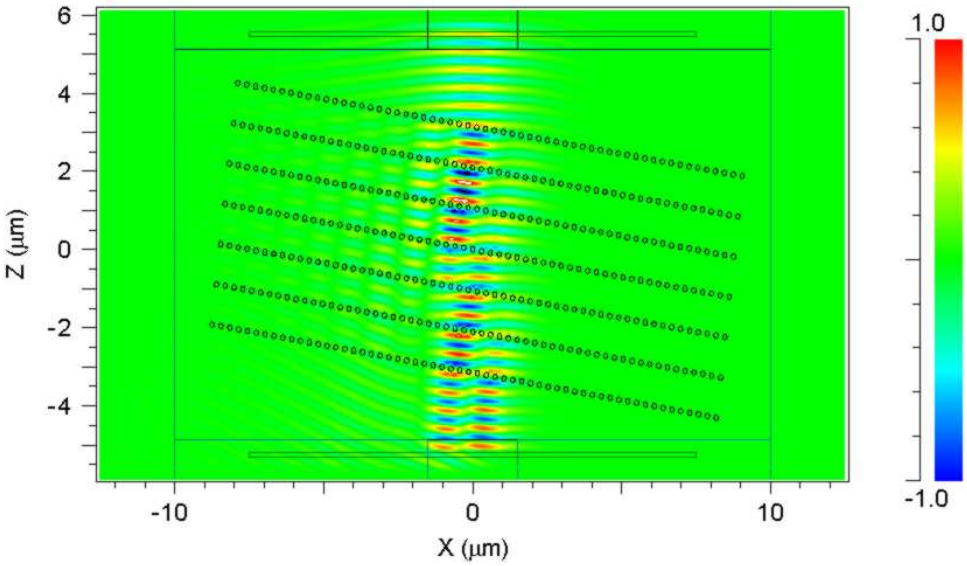

Figure 6.7: FDTD H_y-field component distribution for incidence upon an 8° grating with $r/a = 0.24$ at $\lambda = 1.5\mu$m.

The PC propagation characteristics cause the center of the output beam to be shifted by a small distance from the center of the mesa. Displacement of the output waveguide can thus lead to optimal stop-band extinction and edge slope, as indicated by the dashed curve in Fig. 6.8.

It must be pointed out that the compactness of the design and relatively low insertion loss may allow the cascading of various such filters for proper tailoring of the transmission transfer function.

The reflected power into the fundamental mode remains below -30dB throughout the displayed bandwidth in all cases, a much lower level than observed in the experimental results. One probable reason for this discrepancy is the existence of two high-order modes of the access waveguides, which can carry part of the total reflected power. FDTD simulations in fact show that approximately -15dB and -5dB of the incident power couple respectively into back-reflected first- and

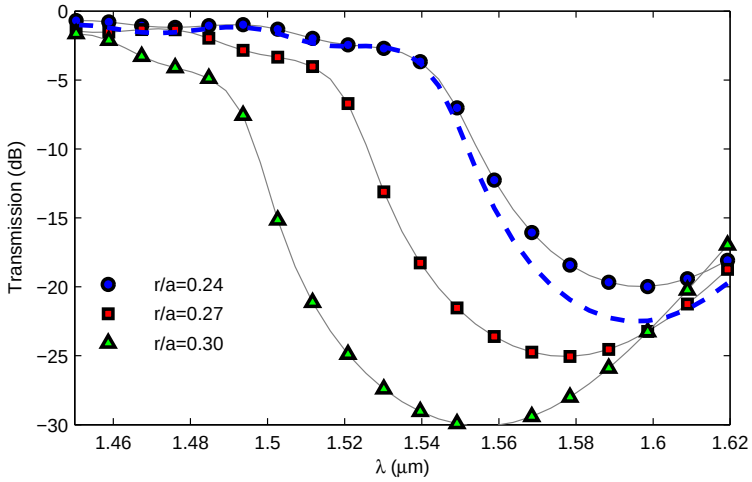

Figure 6.8: Finite-Differences Time-Domain simulation of 8° -tilted gratings with $a = 300$nm and varying r/a. The dashed curved is for a device with $r/a = 0.24$ the output waveguide of which has been displaced to the right by $0.55\mu m$.

second-order mode waves at $\lambda = 1.58\mu$m for an 8° tilt. These modes of course are expected to present considerably higher losses than the fundamental mode. Another possibility would be that the access waveguides are narrower than 3μm -due to imperfect contact lithography- and thus non-optimal for the considered tilt-angles [4] [2]. An FDTD simulation of the 8°-tilt case with a 2.5-μm-wide access waveguide showed approximately -25 and -12dB fundamental and first-order mode reflectivities at $\lambda = 1.58\mu$m. Most likely, a combination of these two possibilities is responsible for the observed power levels. Notice finally that the reference ridge waveguide reflectivity in Fig. 6.4(b) is relatively high and presents 60-nm-period fringes related to multi-mode propagation: this period corresponds to a group-index difference of 0.025, very close to the difference between effective indices of the fundamental and first-order access waveguide modes. This shows that collection of high-order-mode waves by the lensed fibers could significantly

[2] See Chapter 5

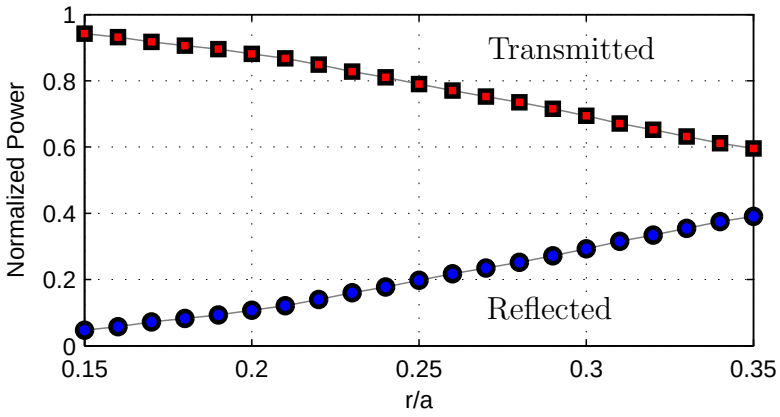

Figure 6.9: Power transmission and reflection from a single row of holes on a background of refractive index $n_{TE} = 3.26$, obtained with FDTD.

influence the signal measurement. Waveguide tapers or mode filters such as described in [8] could in principle be used to eliminate high-order modes thereby yielding improved reflected power levels.

Summary and Conclusions

The demonstrated gratings present an extremely compact footprint of 10mm and a wide bandwidth that could be used for rejection of the entire L-band optical communications band. The maximum extinction achieved was 20dB, which can be improved by etching larger holes. Given the relatively low insertion loss, the filter also offers the possibility of being cascaded, adding another degree of freedom for transfer-function design. Reflectivity levels can be theoretically reduced to very low levels depending upon the design. The experimental reflectivity curves did show a much larger reflected power level, part of which might be carried by a high-order access waveguide mode. This being the case, the experimental reflected power level could be reduced by employment of a mode filter at the

grating input. In summary, the reported structures present good prospects for the implementation of passive optical filters that can be directly incorporated into a monolithic PIC.

It is worthwhile to point out that similar results to the presented above may be obtained from gratings formed by deeply etched trenches rather than holes. The only reason for the choice of PC patterns rather than trenches in the present case was the unavailability of a stable deep trench etching process.

6.2 Three-line-defect Waveguide: Γ-M Orientation

Three-line-defect waveguides are in general multimode at frequencies within the bulk-crystal band-gap as a consequence of the wider channel widths; preferential excitation of particular modes can however be achieved by having proper field distributions at the waveguide input. For instance, incidence of a laterally-symmetric, N^{th} order mode of a butt-coupled ridge waveguide will cause the preferential excitation of symmetric PC modes of the same order [9]. The availability of multiple guided modes translates into a larger flexibility in the design of dispersive elements, since coupling of modes of different orders yields a series of band-gaps at various positions in the crystal band-structure, each having particular propagation characteristics. At the same time, out-of-plane radiation

losses have been predicted [10] to be much lower than those found in single-line counterparts, due to a lesser interaction between the field and PC holes.

The $W3^{(M)}$ waveguide shown in Fig.6.10, formed by omitting three lines of air holes along the $\Gamma - M$ direction of the 2D triangular lattice PC, presents a small band-gap close to the Brillouin-zone boundary; propagation close to the band-gap edges is expected to slow and dispersive. To verify this, a series of 80-μm-long waveguides with lattice constants $a = 400$nm and $a = 420$nm and varying air-filling fractions were fabricated and characterized. The channel widths were on the order of 400nm.

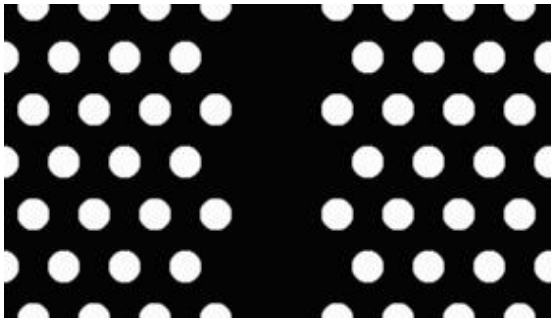

Figure 6.10: Three-line-defect waveguide in the Γ-M direction ($W3^{(M)}$)

Power Flux and Losses

The way in which power is coupled from the input access guides to the output is schematically depicted in Fig. 6.11. In this figure, the entire test-structure was divided in three regions: Region (I) corresponds to the input ridge waveguide; Region (II) to the PC waveguide; Region (III) to the output guide. Incident power upon the PC guide is carried by a fundamental access guide mode. At the interface between access and PC guides, part of the incident power is coupled

to defect- and unbound crystal modes that propagate forward in Region (II); part of it is lost radiatively into the substrate; and finally part of it is reflected into bound an unbound access waveguide modes travelling backwards in Region (I). Reflected power coupled to unbound access guide modes will be lost during propagation towards the collection fiber. Recall that the access guides are multi-mode, so the power collected by the lensed fibers is most likely carried by both fundamental and first-order access guide modes.

Concerning propagation in Region (II): as mentioned previously, part of the incoming power is coupled into the defect-modes of the PC guide, which present high confinement in the defect region. The propagation losses experienced by such modes is represented by the symbol α_b in Region (II) of Fig. 6.11. This includes material absorption and substrate radiation. At the same time, part of the incident power is coupled to poorly confined modes; power coupled to such modes propagates away from the defect, such that only a small portion of it is coupled into bound modes of the output access ridge waveguide in Region (III). The propagation losses of unbound modes are represented by the symbol α_u in Region (II). Unbound PC modes are spread over the crystal regions, interacting strongly with the PC holes; large propagation losses due to radiation are thus expected, such that $\alpha_u \gg \alpha_b$.

At frequencies near the defect-mode band-gap, power carried by forward-propagating defect modes is coupled into backward-propagating defect modes due to the Bragg effect. These reflected waves coupled into both bound and unbound, backward-propagating access waveguide modes in Region (I).

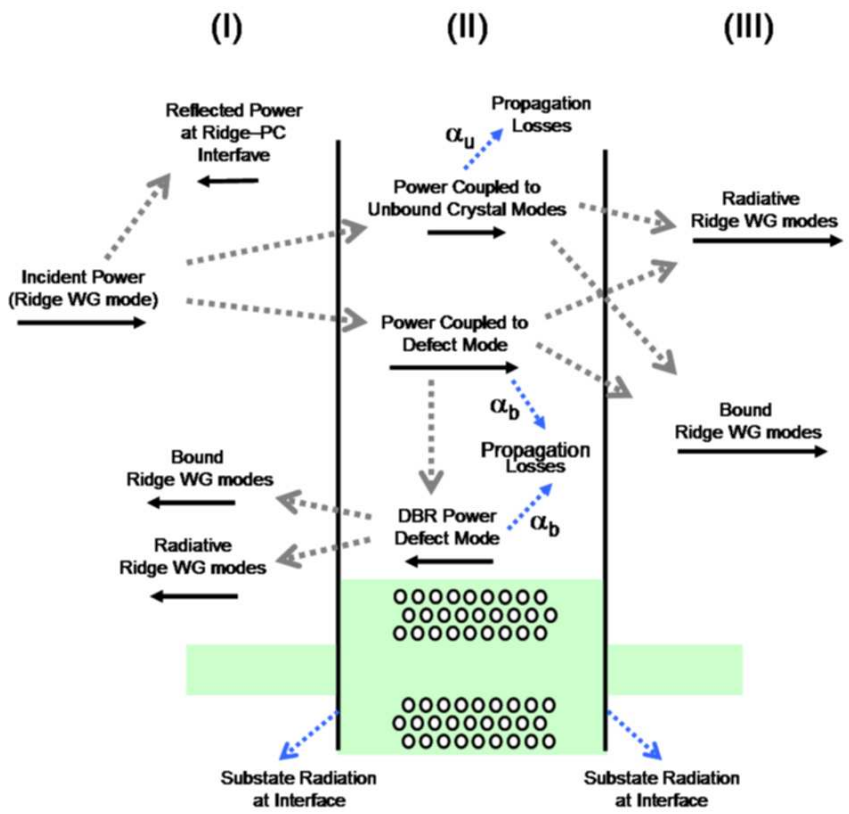

Figure 6.11: Schematic of power flux through test-structures. The symbols α_u and α_b correspond respectively to propagation losses of unbound and defect crystal modes.

From the discussion above, it is very reasonable to assume that power collected from the output ridge waveguide is carried exclusively by defect PC modes in the PC waveguide. The overall insertion loss of the test devices would then include: coupling losses at the fiber-ridge waveguide interface; propagation losses of the access ridge waveguide modes; coupling losses into the defect mode; propagation losses of the defect mode in the PC waveguide; coupling losses from the PC mode into bound access waveguide modes; propagation losses in the output access guides; coupling losses between ridge and collection fiber. Notice that substrate radiation losses at the interfaces, as well as power coupling to unbound access

guide modes can be all lumped together as coupling losses. Return losses of the PC waveguide include reflections from the interface between fiber and semiconductor, ridge and PC waveguides and the distributed Bragg reflectivity.

As will be shown later, the propagation losses of defect PC modes can be estimated by fitting with 1D Coupled-Mode Theory (CMT) expressions.

6.2.1 TE- and TM-polarization Power Transmission

The power transmission for TE and TM waveguide modes was obtained using the techniques described in Chapter 5. The correct correspondence between measured curves and polarization states was primarily verified by infrared imaging of the output waveguide signals through a free-space polarizer. Additionally, experimental results were correlated with effective 2D PC band structures, calculated with the 2D Plane-Wave Expansion (PWE) method [11]. The effectiveness of this technique has been experimentally demonstrated in various articles, including [12, 13, 14]; additionally, it has been detailed in [15] that band-structures of 3D lattice-of holes PC with weak vertical confinement and deep holes can be very well approximated by band structures of effective 2D PC.

Figure 6.12(a) shows band diagrams for TM modes of a waveguide with $r/a = 0.265$ (r being the hole radius) and background index $n_{TM} = 3.26$ (equal to the effective index of the epi-wafer's first TM slab mode at $\lambda = l.55\mu$m). The color scale corresponds to the electric field energy within the line-defect region, normalized to the total power in the unit cell. Well-confined modes (darker dots)

with even symmetry yield higher transmitted output power; two bands of such modes are clearly distinguishable, presenting a small band gap at the Brillouin-zone boundary, around $a/\lambda \approx 0.275$. This band-gap clearly corresponds to the stop-band found in the transmission curves shown in Fig. 6.12(b). Modes on the high-frequency band are well confined, while those on the low-frequency side are more spread out in the crystal region. It is expected that the latter will suffer higher losses, as a result of a larger interaction with holes. Notice that confined modes are of the index-guided type [13], since a bulk-crystal band gap does not exist for TM modes in the present case.

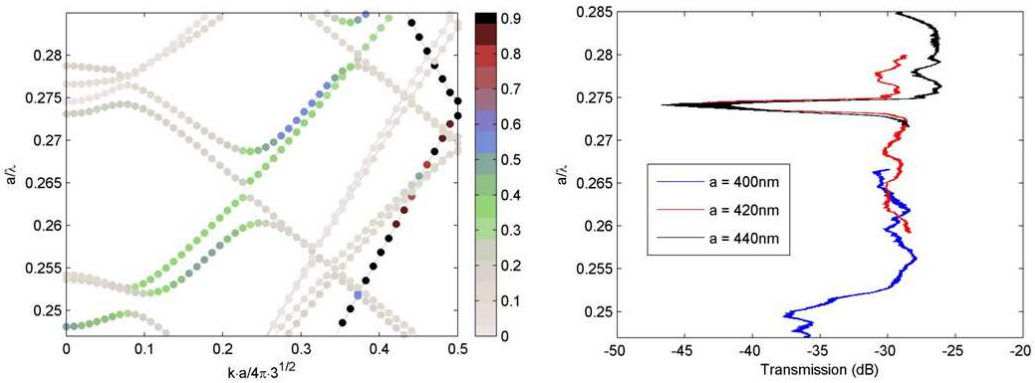

(a) (b)

Figure 6.12: (a) Band structure for TM modes of a W3$^{(M)}$ waveguide with $r/a = 0.265$ and $n = 3.26$. The yellow shaded area indicates the mini-band-gap position. (b) Corresponding TM transmission curves for devices with $a = 400$nm, $a = 420$nm, and $a = 440$nm.

Figure 6.13(a) shows the TE-mode band structure for the same waveguide with background refractive index $n_{TE} = 3.28$ and Fig. 6.13(b) shows the corresponding transmission curve. A high-confinement band below $a/\lambda \approx 0.255$ in Fig. 6.13(a) corresponds to the transmission band on Fig. 6.13(b). The inexistence of highly-

confined modes in the region above $a/\lambda \approx 0.255$ explains the low transmitted power in this range in Fig. 6.13(b). A very small band of highly-confined modes exists near $a/\lambda \approx 0.275$. Transmitted power carried by these is expected to be very low, given their closeness to the Brillouin zone boundary and the narrow width of the band. It must be pointed out that the substrate light-line in all cases meets the Brillouin-zone boundary at $a/\lambda \approx 0.09$ thus all displayed modes are expected to leak into the substrate.

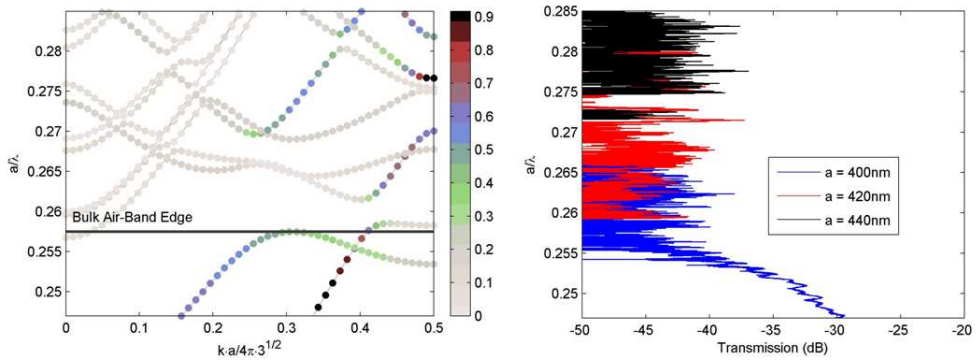

(a) (b)

Figure 6.13: (a) Band structure for TE modes of a W3$^{(M)}$ waveguide with $r/a = 0.265$ and $n = 3.26$. The yellow shaded area indicates the mini-band-gap position. (b) Corresponding TE transmission curves for devices with $a = 400$nm, $a = 420$nm, and $a = 440$nm.

6.2.2 TM Band-edge Propagation

The TM polarization filter characteristics near the band-gap are now studied in more detail. Measured power transmission and reflection from representative devices with $a = 420$nm and $a = 440$nm are shown with black lines in Fig. 6.14. These curves are normalized to their respective maxima within the measurement wavelength range. Transmission group delay curves are also shown in the figure.

An approximately 10-nm stop-band is observed centered at $\approx$ 1533nm for the first device and at $\approx$ 1607nm for the latter, both corresponding to $a/\lambda \approx 0.274$. The less pronounced resonances on the right side of the stop-bands can be explained by the predicted higher losses. The wide stop-band in transmission corresponds to a high-reflection band. Also, maxima in the transmission curves coincide with minima in reflection. These resonances are due to the finite extent of the PC waveguide [16].

It must be pointed out that the TM transmission PDL is more than 20dB at all wavelengths except within the stop-bands for all measured devices; PSP at $\lambda = 1520$nm and 1580nm were used to generate transmission curves respectively for $a = 420$nm and $a = 440$nm. For reflection, PSP at $\lambda = 1532$nm and $\lambda = 1610$nm were chosen, with PDL$\approx$10dB. The raw reflected signal curve presented a series of 0.4-nm-period oscillations caused by a beating of reflected light from the wafer facet and the PC waveguide input. To suppress this effect, the raw signal was filtered with a 51-sample (500pm) Locally Weighted Scatter Plot Smooth (LOWESS) filter.

Group Delay

Group delay curves for the transmitted signal were obtained from the same instrument [17] for a fixed polarization state at the input. Before the measurement was taken, the power in the pass-bands (determined from the previous transmission measurements) was maximized by tuning a polarization controller inserted before the input fiber. This procedure assured that mostly TM modes were be-

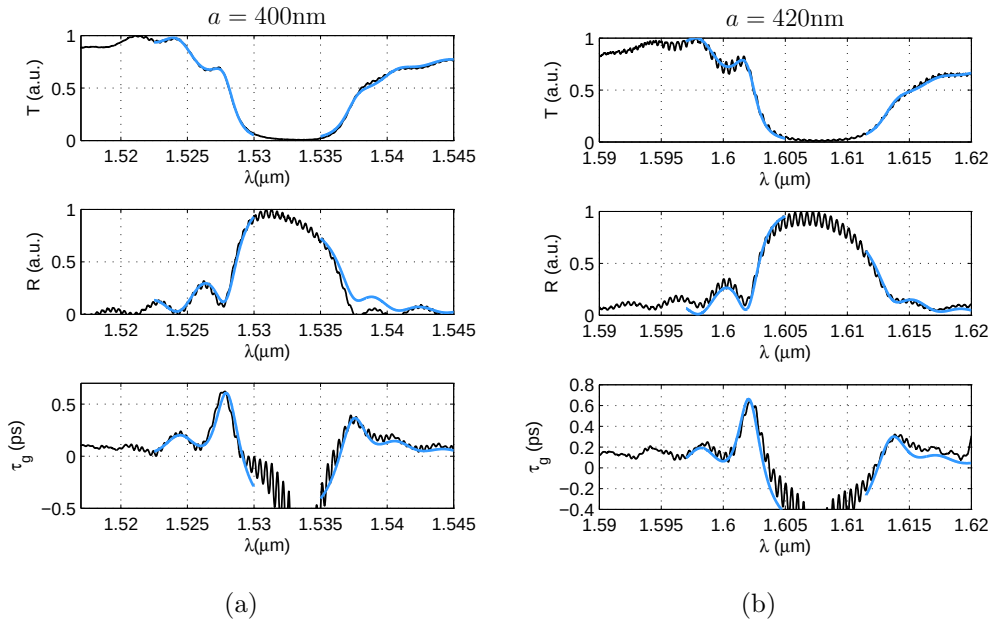

Figure 6.14: Transmission, reflection (T and R in a.u.) and excess group delay (τ_g) for waveguides with two different lattice constants. Black curves are experimental, blue are fitted. (a) $a = 400$nm. (b) $a = 420$nm.

ing excited in the input waveguide. At each wavelength, a 100-sample averaging was used for accuracy. The same measurement was performed for a regular ridge waveguide on the same wafer. The displayed group delay curves are obtained by subtracting the ridge waveguide results from those of the PC waveguides; the displayed values are thus of excess group delay. Cavities between the air-facet and ridge-PC waveguide interfaces caused a series of resonant peaks in the measured curves. Smoothing with a 101-sample (1nm) LOWESS filter revealed the PC waveguide group delay structure alone. Figures 6.14(a) and 6.14(b) show measured group delay for the same devices as in the previous section. The oscillatory profile with maxima at the first reflectivity minimum is due to the finite extent of the waveguides, as detailed in [16]. Similar group delay curves were experimentally observed in a multilayer GaAs PC [18] and more recently in a silica colloidal

PC [19]. The peak excess group delay is $\tau_g \approx 0.62ps$ for $a = 420$nm and $0.65ps$ for $a = 440$nm. The group delay enhancement over that experienced through a ridge waveguide of the same length is of about 60%.

Fitting with Coupled-Mode Theory

Coupled-Mode Theory curves were fitted to the experimental data to yield estimates of coupling strength and propagation losses in the waveguides [12]. In the present case, coupling happens between modes of the same order. Bloch modes on the two sides of the stop-band are considerably different, though, and thus require different fitting parameters. The simplified coupled-mode theory transmission and reflection coefficient expressions in this case are:

$$t = \frac{2\sigma}{(z+\sigma)e^{+\sigma L} - (z-\sigma)e^{-\sigma L}} \tag{6.1}$$

$$r = \frac{2i|\kappa|\sinh(\sigma L)}{(z+\sigma)e^{+\sigma L} - (z-\sigma)e^{-\sigma L}} \tag{6.2}$$

In these equations,κ is the coupling coefficient, $z = \alpha + i \cdot (\beta - \beta_0)$, $\sigma^2 = \kappa^2 + z^2$, α and β the loss and propagation constants for both forward- and backward-propagating modes and L is the total length. The parameter $\beta = 2\pi n/\lambda$ is related to the phase index n, which describes the spatial phase evolution of the field in an unperturbed medium. Notice that material absorption and out-of plane radiation, either intrinsic or caused by hole imperfections can be phenomenologically modeled by the loss parameter.

A least squares fitting algorithm was used to fit the experimental transmission curves of all devices using n, κ and α as parameters. The phase index n was

allowed to change within 10% of the values calculated from the PWE calculation [11]. Fitted curves for the devices shown in Fig. 6.14 are displayed in blue. Fitting values obtained from four devices with $a = 420$nm and slightly different filling fractions were in the ranges $n = 3.5 \pm 0.1$, $\alpha = (41.8 \pm 4.15)cm^{-1}$, $\kappa = (4.3 \pm 0.3)10^2 cm^{-1}$ on the high-frequency band-edge; on the low-frequency edge, $n = 3.7 \pm 0.2$, $\alpha = (77.2 \pm 2.4)cm^{-1}$, $\kappa = (3.7 \pm 0.1) \times 10^2 cm^{-1}$ were obtained. Five devices with $a = 440$nm and slightly different filling fractions yielded parameters in the ranges $n = 3.5 \pm 0.1$, $\alpha = (29.8 \pm 4.9)cm^{-1}$, $\kappa = (3.9 \pm 0.3) \times 10^2 cm^{-1}$ on the high-frequency side and $n = 3.7 \pm 0.1$, $\alpha = (90 \pm 1.2)cm^{-1}$, $\kappa = (4.1 \pm 0.4) \times 10^2 cm^{-1}$ on the low-frequency side. The spread in phase index and coupling coefficients can be attributed to the differing filling fractions and hole quality, as well as noise in the experimental data. Additionally, the CMT model used assumes uniform reflectivity and coupling coefficient distribution along the crystal, while the devices' filling-fractions vary slightly along the PC waveguide. The PC lithography was realized without any proximity-effect correction and thus a slight deviation from the theory is expected.

The large coupling coefficients dictate the wide resonance widths, as well as the stop-band width. It is apparent that losses are considerably higher on the low-frequency band for both groups of devices, as expected from the band diagrams. An inspection of Fig. 4.15 from Chapter 4, which shows a cross-sectional SEM of a representative PC guide, reveals that etched holes barely extend past 1μm below the quaternary layer and become conical in the bottom; some sidewall roughness

is also visible. These features cause large out-of-plane radiation that is directly related to the high loss figures [20].

Reflection and group delay curves were obtained with the same parameters. In all cases, a good agreement with experimental curves is observed. Despite the mild group delay enhancement, calculated GVD from CMT reaches $D \approx -8.5 \times 10^6$ps/km·nm on the high-frequency band-edge for the device in Fig. 6.14(b), almost five orders of magnitude greater than that of dispersion-compensating fiber [21]; this corresponds to a total dispersion of -0.7ps/nm for the $80-\mu$m waveguide. The bandwidth over which the dispersion remains within the same order of magnitude is slightly larger than 1.0nm, pointing towards possible uses of similar PC waveguides in dispersion compensation or pulse-shaping by proper tuning of the coupling coefficient and lattice constant. Considering the same parameters and zero loss, the maximum achievable excess delay and largest total dispersion are respectively 1.06ps, and -1.2ps/nm. On the other hand, it must be noted that the large dispersion figures reported here can in principle be found in any one-dimensional system with very large coupling coefficients. Photonic crystal waveguides naturally offer such characteristics, given the large index discontinuities and very narrow confinement regions.

6.2.3 Summary and Conclusions

Polarization-resolved measurements of transmission, reflection and group delay characteristics of a series of $W3^{(M)}$ PC waveguides was realized. Transmission

and reflection measurements revealed a small stop-band for TM-polarized modes. Measured excess group delay curves displayed a maximum enhancement of approximately 0.6ps (60% over that from a ridge waveguide of the same length) at the edge of the stop-band. Group-Velocity Dispersion of almost five orders of magnitude that of dispersion-compensating fiber was observed in the same region. Experimental curves were fitted with coupled-mode theory, yielding estimates for losses and coupling coefficient. Enhancement of group delay and GVD is clearly dependent on propagation losses. Even at zero loss, though, only a mild enhancement of group delay is found. On the other hand, dispersion is found to be extremely large over reasonably wide bandwidths, even when considerable losses are present. This suggests that, by proper tuning of coupling coefficients, very compact dispersion-compensating or pulse-shaping elements could be designed.

6.3 Multi-mode Line-defect Waveguides

As discussed in Chapter 3, multi-mode line-defect waveguides present small band-gaps for zero-order modes, a convenient characteristic for the realization of monolithically integrated CDWM notch filters. Stop-bands can be positioned by modification of the PC lattice constant or filling factors and of the defect region width. Achievable bandwidths can be rather wide, given the large index discontinuities and narrow channel widths. The transmission transfer-functions are on the other hand strongly dependent upon the propagation characteristics of the many coupled-to modes of the multi-mode PC guide.

Following the discussion from Chapter 3, stop-bands arise from the coupling between effective zero-order and counter-propagating high-order modes, so that, in a simple filter implementation in which a PC waveguide is butt-coupled to regular ridge access guides, waves reflected by the PC distributed-feedback mechanism will tend to couple mostly to higher-order-mode waves of the input access guide. These waves in turn can be mitigated in a number of ways, i.e., tapering of the input guide or even the use of MMI mode-filters [8].

The following investigation shows experimental evidence of multi-mode propagation in asymmetric PC waveguides of various channel widths and its detrimental effects for the realization of notch filters. The experimental test-structures were similar to those described in the previous sections and the same measurement technique was applied.

6.3.1 Anti-symmetric Waveguides

A series of 30- and 80-μm-long anti-symmetric waveguides was fabricated as schematized in Fig. 6.15, with $d = -0.2{\cdot}a_x$, $0.15{\cdot}a_x$ and $0.8{\cdot}a_x$, where $a_x = \sqrt{3}{\cdot}a/2$; these are henceforth respectively referred to as of Types 1, 2 and 3. Crystals were realized with two lattice constants, $a = 350$nm and $a = 360$nm, and slightly varying filling fractions. For the $a = 350$nm crystals, channel widths were 0.84μm, 1.06μm and 1.48μm for Types 1, 2 and 3 respectively; for $a = 360$nm, widths were 0.92μm, 1.12μm and 1.52μm. The choice of lattice constants was based on preliminary calculated band-structures, such that mini-band-gaps could be

observed within the test-equipment wavelength range, $\lambda = 1.5 - 1.62\mu$m. SEM images of representative fabricated waveguides are shown in Fig. 6.16.

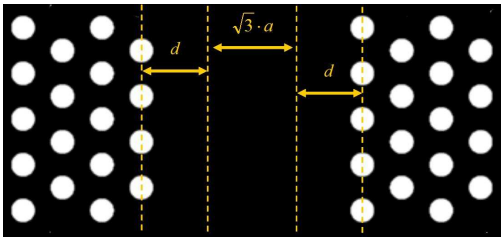

Figure 6.15: Schematic of fabricated asymmetric waveguides.

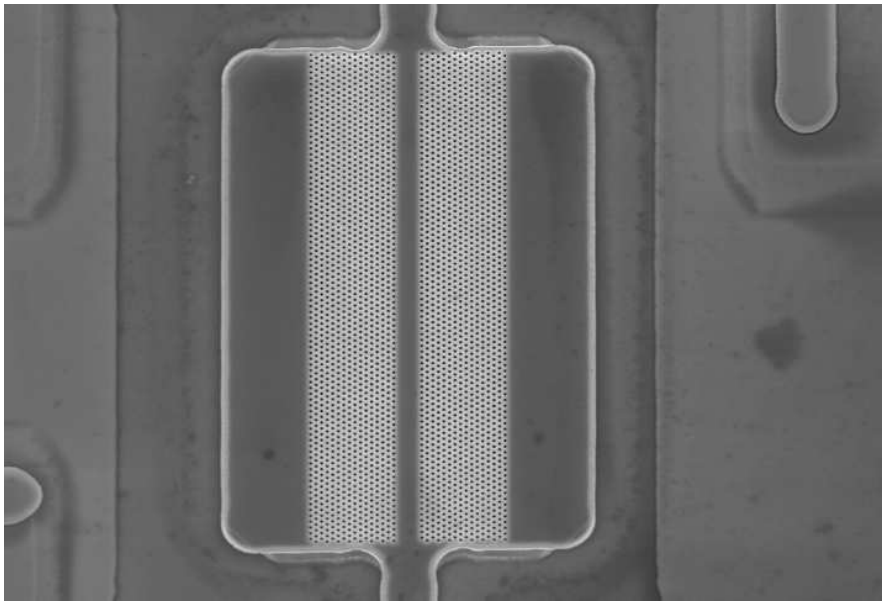

Figure 6.16: SEM image of fabricated PC waveguide on top of a mesa.

6.3.2 Power Transmission Characterization

The TE band-structures for the three waveguide Types and corresponding representative 30-μm-long waveguide power transmission spectra are shown in Figs. 6.17(a)- 6.17(c). The transmission stop-bands can be clearly related to the band anti-crossings - highlighted by grey areas with the label *a*. - between the

fundamental mode band and high-order odd-symmetry bands. Inspection of the band structures and Bloch-mode field distributions reveal that, in the Type 1 and Type 2 cases, the zero-order band anti-crosses with a 3^{rd}-order band, while in the Type 3 case anti-crossing occurs with a 5^{rd}-order band. It is apparent that anti-crossing high-order mode bands give rise to narrower band-gaps: stop-bands for Types 1, 2 and 3 are respectively 30, 17 and 9nm wide, measured at the -10dB level with respect to the pass-band. Notice that waveguide channels are made wider whilst hole radii are kept constant; it is then intuitive that the perturbation experienced by a wave at a fixed wavelength be less strong when guide walls are brought farther apart. Given the effective lesser-magnitude coupling coefficients, narrower band-gaps arise in accordance with the following CMT band-gap equation (repeated from Chapter 3):

$$\Delta_{\pm} = \frac{a}{2\pi} \cdot \frac{4\kappa}{n_{+} + n_{-}}, \tag{6.3}$$

The confinement of the backward-propagating high-order modes in each case tends to decrease with channel width. As mentioned in previously, a lower confinement means larger interaction with crystal holes, which translates into larger propagation losses. Another important aspect it that as crystal-guided bands approach the lower bulk crystal band-gap edge ($a/\lambda \approx 0.212$), confinement in the defect region tends to decrease. This is related to a less effective distributed reflectivity at the waveguide sidewalls.

Coupling coefficients can be estimated from the band-gap width $\Delta_{\pm}$ in the band diagram, by use of Eq. 6.3. For the Type 1 waveguide, the band structure

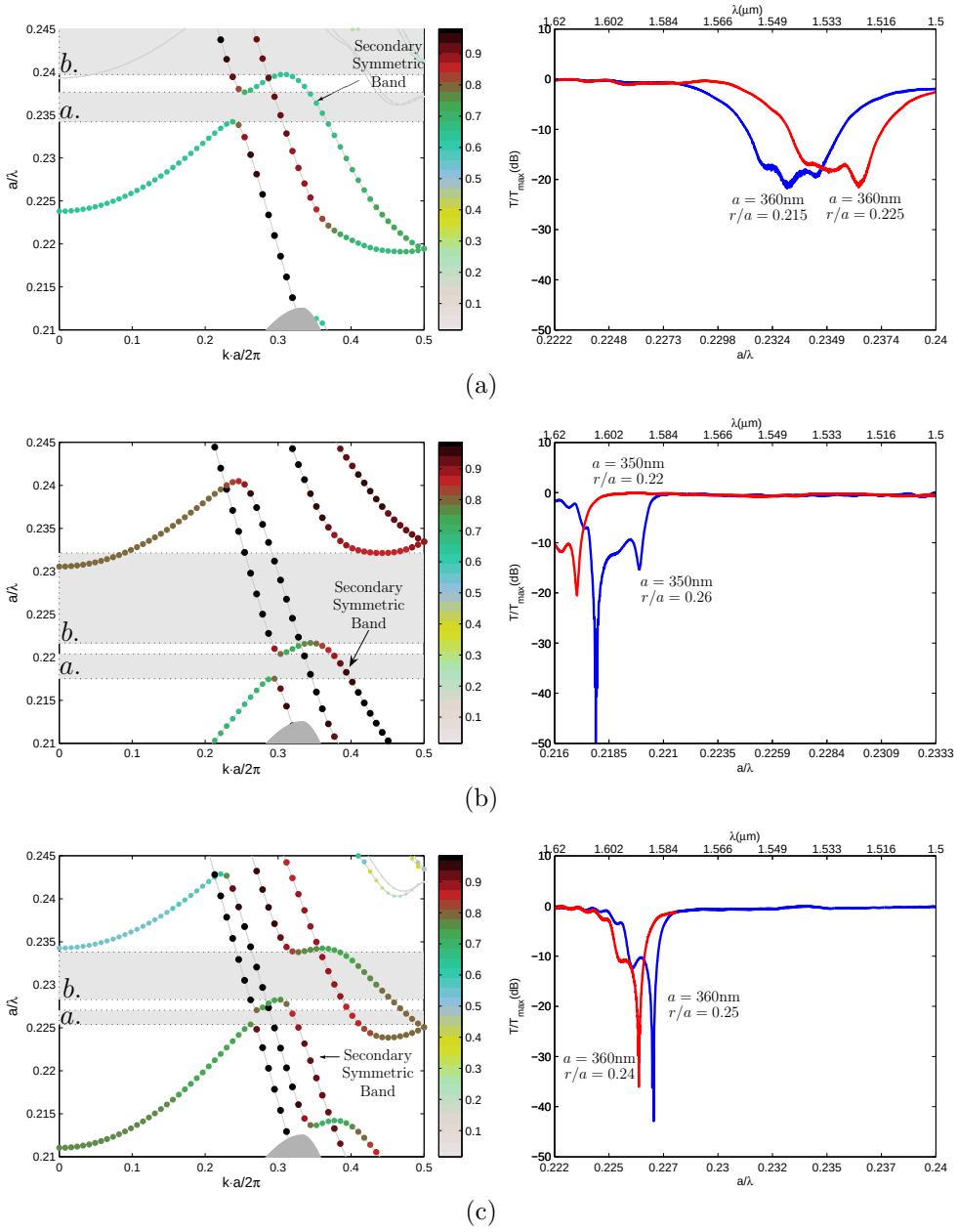

Figure 6.17: Band-structures for $n_{TE} = 3.27$ and $r/a = 0.24$ and corresponding power transmission for representative waveguides of Types (a) 1, (b) 2 and (c) 3. Displayed lattice constants and radii produced calculated band-gaps at corresponding stop-band frequencies. The grey regions labeled $a.$ and $b.$ correspond to band gaps.

yielded $n_+ = 3.42$, $n_- = 11.3$ and $\Delta u = 0.0017$, for which $\kappa \approx 250\text{cm}^{-1}$ ($\kappa \cdot a = 0.09$). In the Type 3 case, $n_+ = 3.42$, $n_- = 11.3$ and $\Delta u = 0.0017$, for which $\kappa \approx 110\text{cm}^{-1}$ ($\kappa \cdot a \approx 0.04$).

The stop-band position can be changed according to the radius dimensions. Very small variations can in fact cause the stop-bands to shift considerably in wavelength: in the Type 1 case, a ≈4nm radius increase causes a stop-band shift of ≈14nm towards shorter wavelengths; in the Type 2 case, a ≈14nm radius increase causes the stop-band to shift by ≈20nm; in the Type 3 case, a ≈4nm radius increase shifts the stop-band by ≈4nm.

It must be pointed out that the position of the band-gaps in the calculated band diagrams is very sensitive to the choice of the background index n_{TE}. The value used in the band structure calculations, $n_{TE} = 3.27$, was within the expected effective TE refractive index interval [3] and yielded band-gaps at frequencies corresponding to the experimental stop-bands for r/a values within the expected ranges: $0.20 < r/a < 0.27$, from inspection of SEM images of the etched crystals. Therefore, $n_{TE} = 3.27$ is assumed to be correct and r/a is used for fine adjustments in subsequent calculations.

Secondary high-order symmetric mode bands exist in all cases, pointed out in the band-structure diagrams, covering frequencies just below the high frequency zero-order-mode band-gap edges. Assuming partial coupling of the incident power to these modes, interference with (co-propagating) zero-order-mode waves is expected at the waveguide output. The deep transmission notches within the stop-

[3] Slab-waveguide mode calculations from Chapter 5 produced $3.25 < n_{TE} < 3.31$.

bands of Types 2 and 3 in fact can be attributed to very efficient destructive interference [4]. The absence of deep notches in the transmission of the Type 1 guide can be attributed to larger losses experienced by modes of the secondary band, which presents very low confinement factors as compared to corresponding bands of the other waveguide types. Notice also that the local power maxima within the stop-bands are about 10dB below the pass-band levels in Types 2 and 3, while Type 1 offers an extinction of roughly 20dB. This is due to the much larger coupling coefficient of the Type 1 waveguide, as well as the propagation losses of both zero- and high-order modes.

Figures 6.18(b) and 6.18(a) show transmission transfer-functions for devices with $a = 360$nm and $L = 80\mu$m of Types 1 and 3 respectively. The stop-band power for Type 1 in this case is lower by roughly 10dB with respect to the $L = 30\mu$m counterpart. This effect is expected from both the larger number of crystal rows and the higher secondary-mode losses. For the Type 2 waveguide, the power at the center of the stop-band is about 20dB below the pass-band and only modest notches are observed. This further corroborates the inference that the deep notches observed in the $L = 30\mu$m case are caused by interference with high-order modes, considering once again that these suffer considerably larger losses than zero-order modes.

The origin of the fringes on the low-frequency side of the stop-bands of the 30-μm-long Types 2 and 3 waveguides is not clear. In principle, similar-period

[4]Destructive interference in this case should be understood in the following way: the resulting field distribution at the interface between the PC guide and the access ridge is such that effectively very little power is coupled into the latter's fundamental mode.

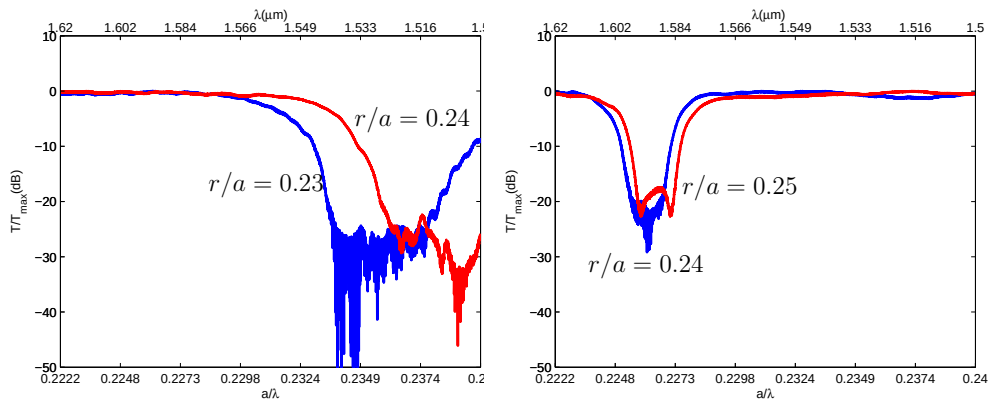

(a) (b)

Figure 6.18: Transmitted and power spectra for 80-μm-long (a) Type 1 and (b) Type 3 waveguides with a = 360nm. Displayed lattice constants and radii produced calculated band-gaps at corresponding stop-band frequencies.

resonances are predicted by coupled-mode theory (CMT) when one uses parameters extracted from the band-structures, as realized in Section 6.2; this however does not explain the absence of resonances on the high-frequency stop-band side, especially since the confinement factors (and therefore propagation losses) on the two stop-band sides are not considerably different. Moreover, when fitting with CMT, the propagation loss parameters required to generate fringes of comparable amplitude variation are too low to produce good fits with experimental curves of corresponding 80-μm-long waveguides, in terms of the stop-band edge slopes [5]. On the other hand, fitting to 80-μm-long waveguide data yields parameters that allow reasonable fits with 30-μm-long waveguide curves as far as the stop-band width is concerned, however with very subdued fringes. Most likely, interference with the secondary symmetric modes plays an important role in the definition of the transfer function, possibly causing the large fringe amplitudes. Notice as well

[5]These are strongly influenced by the backward-propagating wave losses.

that the absence of fringes on the high-frequency side of the stop-bands can be linked to the fact that secondary mode bands in these regions are very weakly confined and present band-gaps (indicated by the grey areas labeled *b.* in the band-structures).

Compared to the transmitted power of a reference straight ridge waveguide, the pass-band power transmission levels varied between -10dB and -5dB among the various tested devices. The uncertainty is due to the different fiber-to-waveguide coupling efficiencies at each alignment, since the devices were in different wafers. Nonetheless, one can estimate insertion losses below 10dB. This relatively high value is partly due to the large mismatch between the PC and butt-coupled ridge waveguide widths. The filter performance could in principle be improved by tapering input and output guides to compatible widths.

6.3.3 Reflectivity

Reflectivity curves for waveguides of Types 1 and 3 are shown in Figures 6.19(a) and 6.19(b). Corresponding transmitted power curves are displayed as well so that stop-bands can be easily located and reference waveguide curves are included for comparison. All reflectivity curves have been smoothed with a running average filter to eliminate Fabry-Pérot resonances.

Small reflectivity peaks can be seen within the band-gap wavelengths, at $\lambda = 1.53\mu$m in the Type 1 case and at $\lambda = 1.59\mu$m in the Type 3 case. The reflected power increase in this region however is not compatible with the large $\approx$20-dB drop

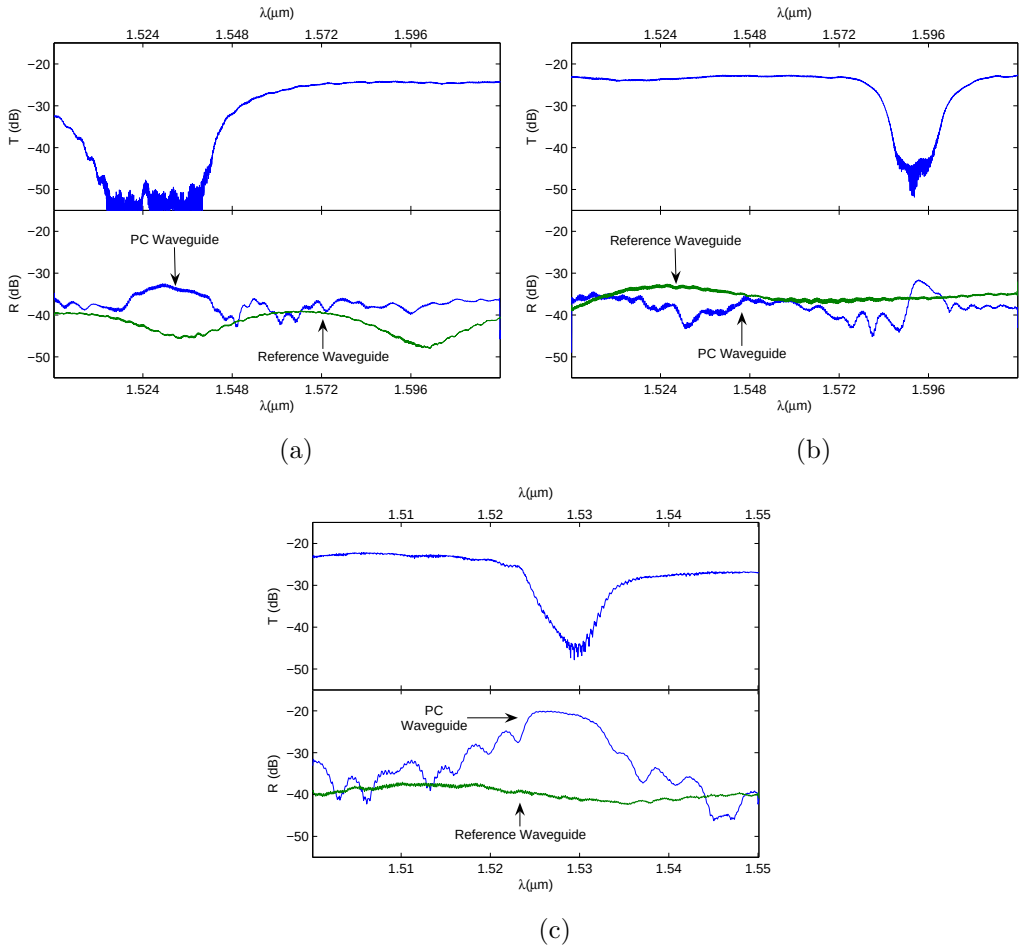

Figure 6.19: Transmitted and reflected power spectra for $80-\mu$m asymmetric waveguides of (a) Type 1 and (b) Type 3. (c) Transmitted and reflected power spectra of an $80-\mu$m $W3^{(M)}$ waveguide.

in transmitted power. Power reflectivity levels are in fact very similar to what is obtained from reference waveguides. In addition, the peak reflectivity levels are quite low when compared to that of the $W3^{(M)}$ waveguide from Section 6.2, shown in Fig. 6.10. In the latter case, backward-propagating modes are zero-order; the reflectivity peak reaches between 10-15dB above the power level outside the band-gap, corresponding to the large stop-band transmitted power drop. A clear distributed-feedback reflectivity signature is in fact easily identified.

It very likely that most of the collected reflected power in the asymmetric waveguide case is carried by high-order access waveguide modes. Nevertheless, a 10-dB reduction in reflected power can be inferred from the experimental results, with respect to the $W3^{(M)}$ reflectivity. This corroborates the validity of the hypothesis that coupling to asymmetric high-order modes may lead to considerably lower reflected power levels.

6.3.4 Stop-Band as Function of Length

Results above related to stop-band extinction are summarized in Figs. 6.20(a) and 6.20(b), which show the maximum insertion and return loss [6] as a function of waveguide length for waveguides of Type 1 and Type 3.

The higher maximum insertion loss observed in Type 1 guides is due to the higher losses experienced by forward-propagating zero- and (secondary) high-order modes, as well as the larger coupling between forward- and backward-propagating PC modes, which results in an increased distributed reflectivity. For the two Types, insertion losses increase considerably with waveguide length, a result of higher total losses experienced by forward-propagating modes and also the increased distributed reflectivity due to the larger number of crystal periods. This increased reflectivity can be linked to a small decrease in minimum return loss for longer waveguide lengths, observed in Fig. 6.20(b). The return loss at the same time remains roughly at the same level for both Type 1 and Type 3 guides,

[6] From the figures in the last two sections, insertion and return loss are maximal and minimal within the stop-bands.

reflecting the fact that the distributed reflected power collected by the access fiber is small.

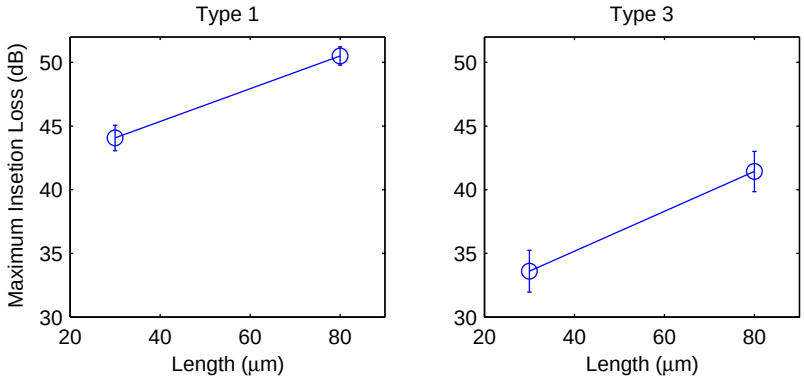

(a)

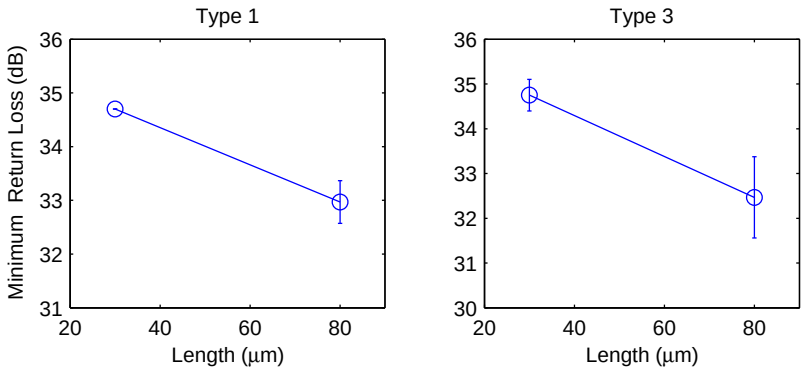

(b)

Figure 6.20: (a) Maximum insertion loss and (b) Minimum return loss as functions of waveguide length for waveguides of Types 1 and 3.

6.3.5 Summary and Conclusions

Asymmetric multi-mode PC waveguides with three different channel widths were fabricated and analyzed experimentally, each providing broad transmission stop-bands that can be convenient for the realization of extremely compact monolithically integrated optical notch filters. Stop-bands originate from the coupling between a forward-propagating zero-order-mode wave and a backward-

propagating high-order mode counterpart. The waveguide channel width determines the existence of high-order-mode bands available for coupling. In general, guides with increased channels widths support better-confined (i.e. with decreased propagation losses) high-order modes; additionally, coupling tends to occur for modes of higher order, which leads to narrower stop-band widths. As an example, channel widths of ≈0.5, 1.0 and 1.5 μm respectively yielded 30-, 17- and 9-nm 10dB bandwidths. High-order-mode losses are in general at least one order of magnitude larger than those of first-order modes and in general have a much larger influence on the stop-band edge slopes.

Multi-mode propagation may considerably affect the transfer functions of short waveguides due to wave interference at the PC guide output. Naturally, this effect is less noticeable if the losses of forward-propagating high-order modes are much higher than those of zero-order-modes; this was in fact the case for the narrowest-channel-width waveguide Type investigated. The stop-band extinction with respect to the pass-bands were on the order of 10dB for 30-μm-long waveguides of Types 2 and 3 (overlooking the deep notches caused by multi-mode interference) and ≈20dB in the Type 1 case. Increasing the waveguide lengths to 80μm causes the extinction to increase by almost 10dB in all cases. The larger extinction observed for Type 1 waveguides is due to the fact that the secondary co-propagating symmetric modes existing within the stop-band wavelength range are much higher than in the other two Types.

Due to a large uncertainty in the coupling efficiency between lensed fibers and ridge waveguides, insertion losses were estimated to be overall anywhere between 5 and 10dB.

Reflectivity measurements revealed small peaks at transmission stop-band wavelengths, however the reflected power level was everywhere comparable to that observed from a straight reference ridge waveguide. Moreover, compared to the reflectivity obtained from a $W3^{(M)}$ waveguide band-gap - which involves the coupling of exclusively zero-order mode waves-, the reflected power was observed to be at least 10dB lower. This shows that coupling to high-order asymmetric backward-propagating modes yields considerably less powerful distributed-feedback back-reflections, either due to large propagation loses or to a poorer coupling to fundamental modes of the access waveguide.

6.4 Single-line-defect Waveguide: Γ-K Direction

The simplest way of realizing a single-mode PC waveguide is to make the defect region sufficiently narrow. A $W1^{(K)}$ waveguide, formed by removing a single row of holes in the Γ-K direction of a triangular lattice, is a classical example of single-mode PC waveguide, with a single bound-mode band within the bulk-crystal band-gap. Due to the very narrow channel, a very strong coupling between counter-propagating waves at the Brillouin-zone boundary is available, such that even with

short waveguide lengths, considerable power extinction at band-gap frequencies are obtained, together with large band-edge group delays. On the other hand, a narrow channel yields larger losses [10], which may seriously deteriorate the available band-edge group delays.

In order to experimentally determine the filtering properties offered by such waveguides, a series of 10-μm-long $W1^{(K)}$ waveguides were fabricated and tested in the same fashion as in the previous sections. The chosen lattice constant was $a = 350$nm, to yield a band-gap within the wavelength range of the measurement instruments. Three devices with different r/a ratios -obtained by proper choice of current doses during the e-beam lithography step- were realized; a SEM picture of a representative device is shown in Fig. 6.21. Inspection of SEM pictures revealed that the fabricated crystals had $0.25 < r/a < 0.29$.

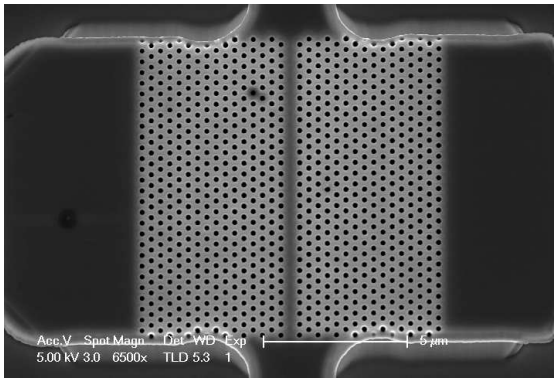

Figure 6.21: SEM image of fabricated 10-μm $W1^{(K)}$ waveguide.

The TE band-structure of a waveguide with $r/a = 0.27$ is shown in Fig. 6.22(a). A close-up of the region within the dotted lines is displayed in Figure 6.22(b), together with the transmitted power spectrum of one of the waveguides. The

transmission stop-band can be related to the non-existence of Bloch modes at frequencies below $a/\lambda \approx 0.219$.

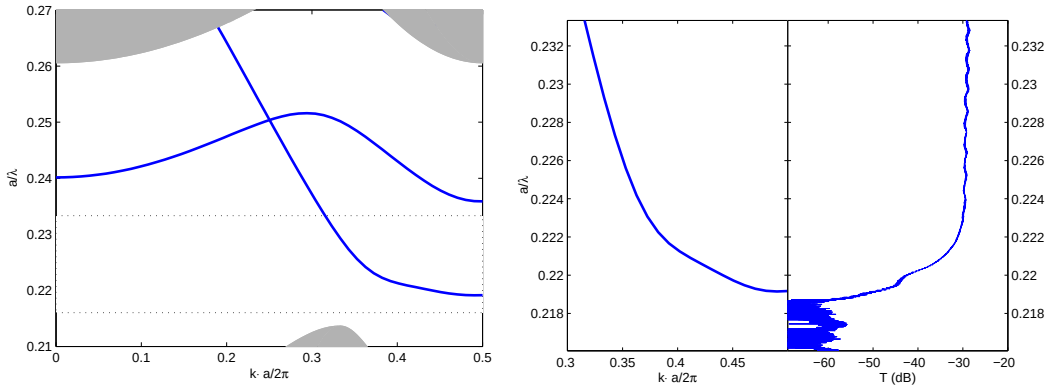

(a) (b)

Figure 6.22: (a) Band-structure for a $W1^{(K)}$ waveguide with $n_{TE} = 3.27$ and r/a=0.27. (b) Close-up of the region within dotted lines in 6.22(a) and corresponding transmission spectrum.

Figure 6.23 shows the stop-band-edge shift for increasing values of r/a, a trend followed by the calculated band-edges at the Brillouin-zone boundary. The r/a values in the graph gave band-edge eigenfrequencies corresponding to the -20dB points of the transmitted power curves. The refractive index was $n_{TE} = 3.27$ in all cases, as in the sections above. Notice that the transmitted power spectrum of a simple ridge waveguide is also plotted in Fig. 6.23, from which a pass-band insertion-loss of approximately 10dB can be estimated [7]. The stop-band extinction with respect to the pass-band is roughly 30dB in all cases, quite impressive for the short waveguide length.

Figures 6.24(a) and 6.24(b) show power transmission, relative Group Delay (GD) and Differential Group Delay (DGD) for the devices with $r/a = 0.255$

[7]Once again, given the $\approx$ 3dB uncertainty in the ridge waveguide transmitted power, the actual insertion loss is expected to be anywhere between 8-11dB.

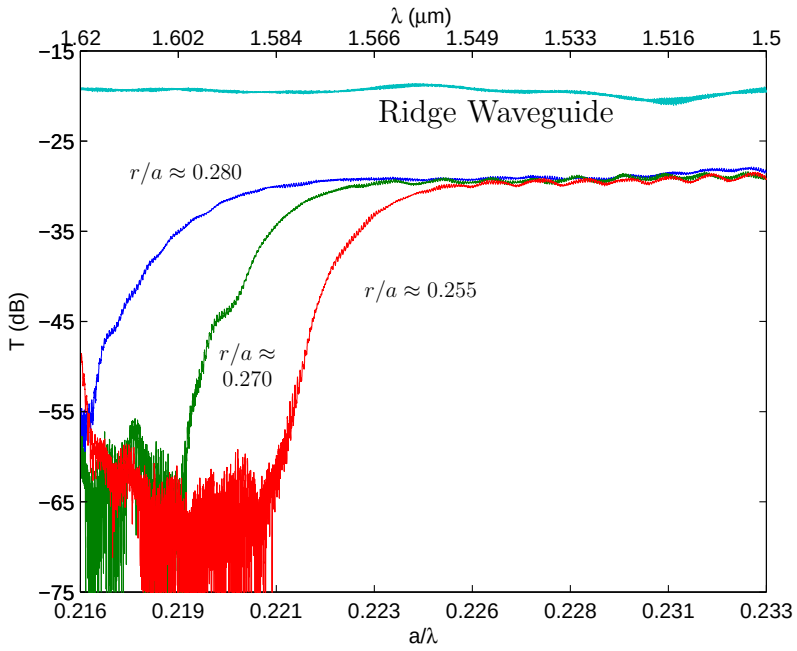

Figure 6.23: Transmitted power for $W1^{(K)}$ waveguides of varying r/a ratios. The values on the figure were obtained by matching the -10-dB wavelength (relative to the passband), of each curve to the band-edge eigenvalue at the Brillouin-zone boundary.

and $r/a = 0.270$ respectively. The relative GD was obtained by subtracting the measured group delay from a simple ridge waveguide from those of the PC guides. The DGD, obtained from Jones the Matrix method [8] gives the modulus of the difference between group delays for TE and TM modes. Since no bulk band-gap for TM modes exist, it is reasonable to say that a very small extra delay (due to the crystal structure) is incurred by TM waves when traversing the 10-μm region. As such, the fact that the DGD is roughly the same as the relative group delay is a good indication of the correctness of this assumption. Notice also that the curves increase by roughly 0.4ps towards the band-gaps, from their values at the highest frequencies. This is also in agreement with the theory from Chapter 3.

[8] See Chapter 5

In absolute terms, the TE group delay is quite modest, however impressive when compared to the maximum values obtained from much longer structures such as the 80μm $W3^{(M)}$ waveguide above. The low group delay levels are most likely due to extremely high propagation losses, as predicted in Chapter 3.

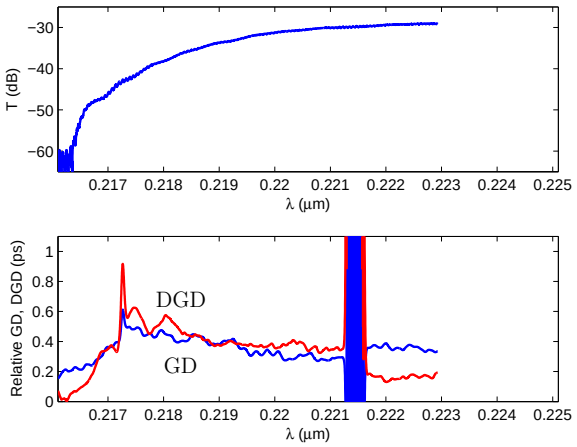

(a)

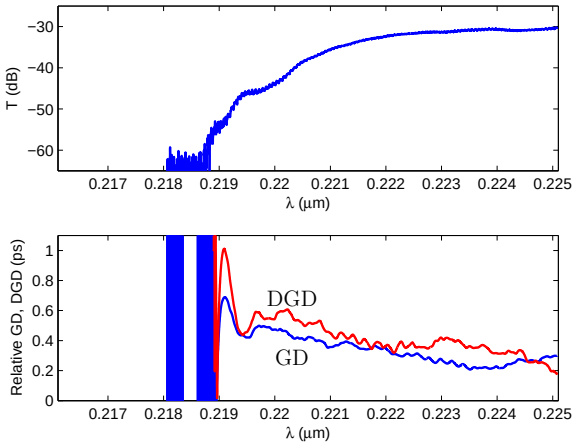

(b)

Figure 6.24: Transmitted power, DGD and Relative GD for (a) $r/a = 0.26$, (b) $r/a = 0.27$.

The large relative GD and DGD peaks are most likely artifacts from the measurement. The peaks in Figs. 6.24(a) and 6.24(b) are at wavelengths where the power transmission is extremely low. One possible source of measurement artifacts

is as follows: as explained in Chapter 5, GD and DGD are calculated from the Jones matrix of the measured device. The determination of the Jones matrix is done by performing a series of transmission intensity measurements for incidence with four different SOPs. Occasionally, in devices presenting very large PDL, one of the chosen input SOPs may produce an extremely low power level at the device output that falls below the reliable power measurement range of the instrument. The generated Jones matrix will then yield a considerable measurement error. In any case, no clear feature in the transmission amplitude transfer function indicate the existence of real group delay peaks, therefore, the existence of a real group delay peaks is very unlikely.

6.5 General Summary and Conclusions

The experimental characterization of four different PC structures was reported in this chapter: a short (10μm) rectangular lattice of holes providing a low-pass transmission transfer function with relatively low insertion loss, low modal reflectivity and a 20dB stop-band extinction; a $W3^{(M)}$ waveguide presenting a small (10nm) stop-band for TM polarization and slow and dispersive propagation at the stop-band edges; a series of short asymmetric multi-mode line-defect waveguides offering transmission stop-bands of more than 20nm and low modal reflectivity; a 10-μ-long single-mode, single-line defect PC waveguide in the Γ-K direction of a triangular lattice presenting a very high extinction stop-band and very low band-edge group velocities.

An overall conclusion of this chapter is that the PC structures studied (waveguides or gratings) offer very good prospects for the realization of very compact, broad-band passive rejection filters that can be monolithically integrated within a complex PIC. Very high transmission extinction can be obtained from very short PC lengths; stop-band widths are in general very wide, resulting mainly from the large index discontinuities involved; insertion losses are relatively high, however can be improved by proper design of ridge-to-PC transitions; stop-band positioning can be realized by tuning of the PC. Even though further work is necessary towards reducing insertion loss and modal reflectivity, the realization of rejection filters is the most direct and straightforward application of the PC waveguides studied.

Low group velocities were found at stop-band edges in some of the studied waveguides, however the reduction of light speed was quite low and limited to a small bandwidth. High propagation losses were in great part responsible for the low group delays observed; at the same time, very high dispersion was observed at the band-edges, even in the presence of high losses. Thus band-edge dispersion is still a very promising property of PC waveguides for pulse-shaping applications.

References

[1] A. S. Jugessur, P. Pottier, and R. M. D. L. Rue, "Microcavity filters base-don hexagonal lattice 2-D photonic crystal structures embedded in ridge waveguides," *Phot. Nanostruc. Fund. Appl.*, vol. 3, pp. 25–29, 2005.

[2] M. L. Mašanović, V. Lal, J. A. Summers, J. S. Barton, E. J. Skogen, L. G. Rau, L. A. Coldren, and D. J. Blumenthal, "Widely-tunable monolithically-integrated all-optical wavelength converters in InP," *J. Lightwave Technol.*, vol. 23, pp. 1350–63, 2005.

[3] P. Kwa, R. A. Tkach, and A. R. Chraplyvy, "Linewidth broadening and mode splitting due to weak feedback in single-frequency 1.5μm lasers," *Elec. Lett.*, vol. 21, pp. 1081–1083, 1985.

[4] M. J. Connelly, *Semiconductor Optical Amplifiers*. Dordrecht, The Netherlands: Kluwer, 2002.

[5] C. E. Zah, R. Bhat, S. G. Menocal, N. Andreakis, F. Favire, C. Caneau, M. A. Koza, and T. P. Lee, "1.5μm GaInAsP angled-facet flared-waveguide traveling-wave laser amplifiers," *Photon. Tech. Lett.*, vol. 2, no. 1, 1990.

[6] T. D. Happ, A. Markard, M. Kamp, J.-L. Gentner, and A. Forchel, "Short cavity InP-lasers with 2D photonic crystal mirrors," *IEE Proc.-Optoelecton.*, vol. 148, pp. 183–187, August 2001.

[7] L. Soldano and E. C. Pennings, "Optical multi-mode interference devices based on self-imaging: Principles and applications," *Jour. Lightw. Tech.*, vol. 13, no. 4, 1995.

[8] C. Aramburu, C. Vázquez, M. Galarza, M. López-Amo, and J. M. S. Pena, "Mode filter using multimode interference principles: Design and tolerance analysis for accessing waveguides supporting two guided modes," *Microw. Opt. Tech. Lett.*, vol. 26, no. 2, p. 140, 2000.

[9] M. Davanço and D. J. Blumenthal, "Exploring slow and dispersive propagation in 2D line-defect photonic crystal waveguides," *2003 IEEE LEOS Annual Meeting Conference Proceedings*, pp. 216–217, 2003.

[10] W. Kuang, C. Kim, A. Stapleton, W. J. Kim, and J. D. OBrien, "Calculated out-of-plane transmission loss for photonic-crystal slab waveguides," *Opt. Lett.*, vol. 28, pp. 1731–1783, 2003.

[11] S. G. Johnson and J. D. Joannopoulos, "Block-iterative frequency-domain methods for Maxwell's equations in a planewave basis," *Opt. Express*, vol. 8, no. 3, pp. 173–190, 2001.

[12] S. Olivier, H. Benisty, C. Weisbuch, C. Smith, T. F. Krauss, and R. Houdré, "Coupled-mode theory and propagation losses in photonic crystal waveguides," *Opt. Express*, vol. 11, p. 1490, 2003.

[13] S. Olivier, H. Benisty, C. Smith, M. Rattier, C. Weisbuch, and T. F. Krauss, "Transmission properties of two-dimensional photonic crystal channel waveguides," *Opt. Quantum Electron.*, vol. 34, pp. 171–181, 2002.

[14] A. Talneau, L. L. Gouezigou, N. Bouadma, M. Kafesaki, C. M. Soukoulis, and M. Agio, "Photonic-crystal ultrashort bends with improved tansmission and low reflection," *App. Phys. Lett.*, vol. 80, pp. 547–549, 2002.

[15] M. Qiu, "Effective index method for heterostructure-slab-waveguide-based two-dimensional photonic crystals," *App. Phys. Lett.*, vol. 81, pp. 1163–1165, 2002.

[16] J. M. Bendickson, J. P. Dowling, and M. Scalora, "Analytic expressions for the electromagnetic mode density in finite, one-dimensional photonic band-gap structures," *Phys. Rev. E*, vol. 53, pp. 4107–4121, 1994.

[17] T. Jensen, E. Witzel, A. Paduch, P. Ziegler, E.U.Wagemann, and O. Funke, "A new method to determine loss, PDL, GD and DGD of passive optical components," *18th NFOEC, Dallas*, p. 14621470, 2002.

[18] L. J. Gamble, W. M. Diffey, S. T. C. R. L. Fork, D. K. Jones, J. T. R. Nelson, J. P. Loehr, and J. E. Ehret, "Simultaneous measurement of group delay and

transmission of a one-dimensional photonic crystal," *Opt. Express*, vol. 5, p. 267, 1999.

[19] G. von Freymann, S. John, S. Wong, V. Kitaev, and G. A. Ozin, "Measurement of group velocity dispersion for finite size three-dimensional photonic crystals in the near-infrared spectral region," *App. Phys. Lett.*, vol. 86, p. 053108, 2005.

[20] H. Benisty, P. Lalanne, S. Olivier, M. Rattier, C. Weisbuch, C. J. M. Smith, T. F. Krauss, C. Jouanin, and D. Cassagne, "Finite-depth and intrinsic losses in vertically etched two-dimensional photonic crystals," *Opt. Quantum Elec.*, vol. 34, pp. 205–215, 2002.

[21] A. Xing, M. Davanço, S. Camatel, D. J. Blumenthal, and E. L. Hu, "Pulse compression in line defect photonic waveguide," in *Proceedings of the Optical Fiber Communications Conference 2005*, p. OWD5, 2005.

Chapter 7

Summary, Conclusions and Future Work

7.1 Summary and Conclusions

The main purpose of the present work was the development of novel applications for quasi-2D Photonic Crystals (PCs) in InP-based Photonic Integrated Circuits (PICs) for optical communications. The character of the investigation was exploratory, as the complex wave-propagation properties in PCs are generally not easily elucidated and not immediately usable in most common established PIC applications. At the same time, the exploration was biased towards practical applications, keeping in mind aspects of propagation in PCs that could be understood or achieved in a straightforward manner, or those that could not be easily avoided.

Line-Defect Waveguides

Focus was given to the investigation of slow and dispersive propagation in PC line-defect waveguides, which so far seems to be the strongest asset offered

by these structures, specially considering the high losses found in deeply etched crystals. The theoretical assessment was partly based on crystal band-structure calculations, numerical (Time-Domain) simulations and simplified analytical models, which contributed in a complementary way to the overall built-up knowledge: from the calculated band-structures one obtains a rough idea of spatial wave propagation by inspection of the available Bloch modes at specific frequency ranges and their associated dispersion characteristics; from simulations, one obtains information from realistic structures, which might not be immediately predictable from band-structures or simplified analytical models alone; from analytical models, one gains a clear insight on the physical mechanisms involved, as well as of the most influential parameters to the phenomena observed either in simulation or experimentally.

An attempt to explain slow and dispersive band-edge propagation in finite PC line-defect waveguides in terms of 1D Coupled-Mode Theory (CMT) was realized, with results confirmed experimentally for band-gaps at the Brillouin-zone boundary. The physical mechanism described by CMT is the coupling of counter-propagating one-dimensional waves caused by a periodic perturbation of the propagation medium, in exactly the same way as in Distributed-Feedback (DFB) mirrors.

Generalized CMT equations for coupling of modes of different orders were theoretically investigated for modelling the propagation around stop-bands formed at anti-crossings of Bloch mode bands away from the Brillouin-zone boundaries. The

generalized equations were shown produce very similar results to those obtained from exact simulations, evidencing the validity of the analytical approximation.

Following this, an assessment of the various parameters influencing the PC waveguide transfer-functions was carried out, assuming the validity of the analytical model. The following conclusions were reached regarding band-edge propagation in PC waveguides: the transmission and reflection transfer-functions of a finite PC guide at the edges of a band-anti-crossing stop-band present a series of Fabry-Pérot-like resonances related to the finiteness of the structure. A maximum transmission group delay is found at the first transmission maximum outside of the band-gap; the maximum delay is larger the narrower the bandwidth of the transmission peak, such that fundamentally large delays can never be achieved with large bandwidths. Additionally, large propagation losses are detrimental of the maximum achievable group delay, apart from the power transmission level.

It must be pointed out nonetheless that experimental evidence on the validity of the generalized CMT expressions for description of propagation at band anti-crossings has been found, at least as far as the prediction of stop-band widths. Initial evidence of this had already been reported in [1] in similar PC guides.

The lowest observed Group Velocity (GV), from a three-line-defect waveguide, was $0.17 \cdot c$, very close to the the smallest reported in the literature in multimode waveguides, $\approx 0.13 \cdot c$ [2]. A very large Group Velocity Dispersion (GVD) ($\approx$ 0.7ps/nm) was observed concomitantly with the enhanced band-edge group delay. The GVD remained within the same order of magnitude over $\approx$1nm.

The propagation losses observed were one order of magnitude higher than the lowest reported in similar systems [3, 4]; it must be pointed out the in the latter case the epitaxial structures were optimized for lower losses (guiding layers were $>0.9\mu$m thick) and waveguides were considerably wider (these were Γ-K-oriented rather than Γ-M as in our case). Moreover, our epi-structure included a p-doped upper InP cladding topped by a highly conductive InGaAs layer which certainly added up to the propagation losses. As such, in view of the large GVD obtained in spite of the large losses, one can infer the good potential of employing PC waveguides in pulse-shaping applications.

Notice that the GV values pointed out above are at least one order of magnitude larger than the lowest reported for Si-membrane, single-line defect waveguides [5], which present both lower losses and a considerably larger coupling coefficients. The present work also shows the evidence of the availability of much lower group velocities in single-line-defect waveguides in InP deeply etched crystals, despite the high propagation losses [6].

All things considered, this study was an attempt towards understanding the filtering properties of PC line-defect waveguides and their limitations and applications in optical signal processing in monolithic PICs.

Band-pass and Notch Filters

One obvious application of photonic band-gaps is the realization of extremely compact band-pass or notch filters. This objective was pursued in multi-mode

line-defect waveguides and one bulk PC lattice. In each case, a mechanism was devised for the reduction of modal back-reflections from the filter input.

Multi-mode waveguides in general present wide (typically $>$ 10nm) transmission stop-bands related to the anti-crossing of defect-mode Bloch bands of different orders. Roughly, the formation of the stop-band is related to coupling of counter-propagating modes of different orders by an effective waveguide-wall corrugation. The large width of transmission stop-bands can be attributed to the very strong wave-coupling stemming from the large index discontinuities and index-steps offered by the PC waveguide. Evidence of multi-modal propagation was observed in power transmission measurements in the form of deep stop-band notches and pass-band oscillations; this clearly indicates the necessity of managing mode-coupling and propagation for the definition of proper filter transfer-functions. The investigated waveguides were composed by PC walls displaced longitudinally by half a lattice constant, such that the stop-band-spanning coupling between modes of different parities -and therefore of different orders- was forced. The purpose of this design was the reduction of fundamental-mode back-reflected power, since it was expected that distributed-feedback waves of high order would couple preferentially to high-order access waveguide modes. The detected reflected power levels were in fact considerably lower than observed from waveguides displaying same-order-mode coupling. The result may however be partly attributed to the larger propagation losses suffered by high-order PC waveguide modes. Finally, a 30μm long waveguide was demonstrated with a 40-nm transmission stop-band with 20dB extinction that could be used as a coarse WDM notch-filter. The insertion loss of

this device (and others tested) exceeded 5dB, however this could in principle be improved by proper design of PC waveguide/ridge waveguide interfaces.

A 10-μm rectangular lattice bulk PC was investigated for application as a low-pass filter that could be used for rejection of the entire L optical communications band. The maximum stop-band extinction was close to 20dB and the pass-band insertion loss was below 3dB. Improvement of the extinction and band-edge slopes could in principle be realized by increasing hole-sizes and positioning of the ridge access waveguides. The comparison between measured and FDTD-calculated results was very good. In order to reduce the back-reflection levels, the PC structures were tilted by a few degrees with respect to the incident beam, in a scheme similar to what is used for mitigation of facet reflectivity in Traveling-wave Semiconductor Optical Amplifiers (TW-SOAs) [7]. This scheme produced a good (15dB) reduction of modal reflectivity, with respect to un-tilted gratings.

Fabrication

The fabrication process for InP-based PICs incorporating deeply etched PCs described in Chapter 4 is one of the principal achievements of the present investigation. The technique was developed from a process used to produce devices based on a mature PIC platform which had previously been used to successfully produce a large set of working components: Distributed-Feedback (DFB) or Sampled-Grating Distibuted-Feedback (SG-DBR) lasers, semiconductor optical amplifiers, photodetectors, interferometric wavelength converters, traveling-wave photodetectors, etc. The PICs produced with this platform are composed of

weakly guiding shallow ridge waveguides that can be electrically pumped through metal contacts. Active gain is provided by InGaAsP quantum-wells grown on top of the InGaAsP guiding layer which is in general selectively removed from the passive regions of the circuit previous to an InP regrowth step. Even though the devices fabricated in this work did not present optically active material regions (at least in the optical communications wavelength range), electrical pumping of selected waveguides was shown to be possible. The steps necessary for the inclusion of selected active regions within the PIC would not require substantial changes to the process; in fact it would only require the inclusion, without modification, of all steps previous to and including the top InP regrowth.

The fabricated test devices offered enough flexibility to allow the characterization of various different types of PC structures; in addition, the mechanism used for light insertion and extraction facilitated considerably the measurement procedure and yielded reliable and repeatable results.

It must be noticed that a similar platform has been used to produce extremely compact coupled-cavity tunable lasers composed of PC line-defect waveguides [8] and lasers with PC mirrors [9].

7.2 General Conclusions

Most of the more interesting properties of PC structures originate from resonant interference effects. The main application-limiting factor of deeply etched PC structures are, as such, radiation losses due to hole imperfections. Take for

instance slow band-edge propagation in line-defect waveguides: lower group velocities are observed for lower propagation losses, given that the slow-down of light is a result of the efficient interference of waves partially reflected along the waveguide length. Clearly, reduction of out-of-plane radiation losses is essential for the development of meaningful PC applications.

On the other hand, while the quality of the deeply etched PCs still needs considerable improvement, development of useful applications is still be possible if reduced interaction with lossy crystal regions is established and resonant regimes are avoided. This is the case of the grating filters, or even the notch filters based on short PC line-defect waveguides studied in Chapter 6. It is important to notice also that band-edge dispersion in line-defect waveguides is found to be quite large even in the presence of high propagation losses and thus constitute a very interesting asset for pulse-shaping applications.

A very important point in terms of PC analysis an design is that the simple study of band-structures only yields limited information regarding wave propagation and ultimately filter transfer functions. The finiteness of real PC structures has a decisive influence on the obtained filter transfer functions and so must be taken somehow into account. Numerical simulations, for instance using the FDTD method, yield very realistic transfer functions, allowing to some extent for general conclusions to be taken regarding the physical mechanisms involved. As much as possible, however, simplified analytical models should be employed to describe wave phenomena in PCs, so that the PC transfer functions can be understood in a general way. In summary, the analysis and design process should include these

three approaches in a synergistic way so that a complete understanding of the PC transfer functions can be attained.

Finally, it must be pointed out that the 2D band-structures used in the present work could be quite well correlated with experimentally obtained data. This further validates the assumption that effective 2D PC band structures approximate quite well those of equivalent quasi-2D PCs.

7.3 Future Work

Suggested future work based on the presented results is detailed in what follows, divided in three categories.

Novel Devices

The most useful PC properties offered by the fabricated photonic crystals are the high, controllable modal reflectivity, the relatively large group velocity dispersion and the broad, controllable transmission stop-band widths; these may be obtained from very compact structures, with lengths of a few tens of microns, and in spite of the large crystal radiation losses. Based on these results, the following possibilities should be immediately investigated:

The fabrication of devices with active QW regions would require very small modifications to the current process. Extremely compact laser sources could thus be implemented without much trouble. The demonstration in [8], realized in a similar PIC platform, shows the excellent prospects for the realization of com-

pact, tunable devices. Sources thus fabricated could be used to replace considerably larger monolithically integrated SG-DBR lasers, for instance in all-optical wavelength-converters [10]. On the other hand, the structures demonstrated in [8] were limited in terms of wavelength tunability, which was not continuous, and in efficiency, due to high levels of non-radiative recombination in the PC material. Investigation of novel, better-performing, compact tunable PC laser structures thus constitute a very interesting line of research.

One interesting possibility still not experimentally investigated is the realization of pulsed, mode-locked laser sources based on PC waveguides. Dispersion management provided by the photonic crystals could in principle be used for pulse-width enhancement.

Immediately viable is the realization of Gires-Tournois-interferometer all-pass filters. These structures offer a flat reflectivity response and a series of phase resonances that can be used for dispersion compensation [11]. The structures could be composed of passive, low-loss, electrically pumped ridge waveguides and PC mirrors whose reflectivities can be tuned through the crystal properties. The results from Chapter 6 demonstrate the feasability of good quality and highly reflective mirrors for this particular application. Active control of the phase response could be realized by current injection into the ridge waveguides.

The realization of PICs incorporating the band-pass and notch filters demonstrated in Chapter 6 would ultimately prove the usefulness of such structures. Applications would include C-to L- band and two-stage interferometric wavelength conversion, or even cross-gain modulation wavelength conversion.

On the other hand, the reflectivity characteristics have to be more closely investigated, as the presented results do not show whether sufficient suppression is obtained. This could be carried out by characterization of spectral resonances in cavities including active ridge waveguides and filter structures as mirrors. At the same time, an optimization of the ridge waveguide/PC waveguide interfaces must be carried out for further improvement of filter insertion and return losses.

Clearly, alternative filter functions can be produced by proper choice of bulk PC structures, as discussed in the first section of Chapter 6. Filters with narrower pass-bands based on PC microcavities have in fact been demonstrated in [12], and could easily be investigated, specially regarding the reflectivity suppression mechanism presented in this work.

Fine tuning of line-defect waveguide stop-band position by current injection is another very interesting concept to be explored. In InP SG-DBR lasers, index changes of 0.1% are typically are achieved [13], leading to grating-mirror reflectivity shifts on the order of a few nanometers. Shifts of the same order of magnitude can be expected for PC waveguides. This could prove a convenient way of tuning the large dispersion experienced by pulses propagating at stop-band edges.

Fabrication Technique

The Cl_2-Ar ICP etching recipe used in this work is not completely optimized and could be further improved for the achievement of much deeper holes and higher aspect-ratios, with better selectivity with respect to the SiO_2 mask. At the same time, optimization of the Cl_2-N_2 recipe would also be desired given

the possibility of achieving extremely smooth hole sidewalls. At the same time, etching schemes using alternate steps that successively etch the semiconductor surface and passivate the sidewalls could also be explored. This scheme has been shown to produce very high aspect-ratio structures in Silicon, and is generally used in Micro-Electro-Mechanical Systems (MEMS) fabrication [14]. The major difficulty in developing a Cl_2-based recipe using this scheme is the formation of non-volatile etch-products such as $InCl_x$, which are redeposited on the etched surfaces. The build-up of such etch-products eventually completely stops the substrate etching.

The improvement of propagation losses could in principle be realized through the design of a proper epitaxial structure, without compromising the performance of the additional PIC components. As mentioned in Chapter 1, order-of-magnitude lower losses were obtained from properly designed slab waveguide structures.

The present fabrication process can be yet simplified by realizing the PC definition step previous to the definition of ridges and mesas. This could be very convenient for the fabrication of devices in which PC alignment within the circuit is not critical.

Finally, the investigation on the possibilities of incorporation of InGaAsP membranes within monolithic PICs should be carried out, as these structures present potential advantages with respect to deeply etched PCs regarding propagation losses.

Basic Photonic Crystal Research

The good coincidence between calculated band-structures of 2D and 3D weakly guided PCs has not yet been rigorously explained, neither have strict general rules regarding the applicability of the effective 2D approximation been established. Even though much experimental evidence is available in favor of the utilization of effective 2D PC band-structures, a final in-depth theoretical analysis is in order.

One interesting possibility regarding the establishment of stricter rules for the approximation could be an analysis in terms of the coupling of slab modes, bound and radiative, by the etched holes, in a perturbation theory approach. This could furthermore lead to the development of useful guidelines for the design of epitaxial structures optimized for low out-of-plane radiation losses, based on the optimization of slab-mode field profiles.

At the same time, an interesting problem is the correlation between feature non-uniformity and achievable PC properties. A study of this problem could yield information regarding the necessary fabrication tolerances. This would be particularly useful for deeply etched crystals which in general present very rough hole sidewalls due to the aggressive (though necessary) etching processes. An interesting and simple study could be carried out by comparing the properties of equivalent PCs etched with Cl_2:Ar and Cl_2:N_2.

Finally, different PC waveguide configurations should be investigated providing larger, broad-band, band-edge dispersion characteristics. As discussed in the text, in line-defect waveguides these properties are linked to the wave-coupling

introduced by the crystal medium, with losses playing an important role. On the other hand, one interesting possibility would the utilization of crystal-guided modes close to the $k = 0$ point, which, as pointed out in Chapter 3, display slow group velocities simply because of the guiding mechanism. In this case, power transmission would be spectrally flat as long as one were able to couple to such waves in a wavelength-independent way. These modes however are in general of high order, thus requiring more involved coupling mechanisms. In addition, these modes are expected to be considerably lossy,due to an increased interaction of the field with the crystal holes.

References

[1] S. Olivier, H. Benisty, C. Weisbuch, C. Smith, T. F. Krauss, and R. Houdré, "Coupled-mode theory and propagation losses in photonic crystal waveguides," *Opt. Express*, vol. 11, p. 1490, 2003.

[2] H. Gersen, T. J. Karle, R. J. P. Engelen, W. Bogaerts, J. P. Korterik, N. F. van Hulst, T. F. Krauss, and L. Kuipers, "Real-space observation of ultraslow light in photonic crystal waveguides," *Phys. Rev. Lett.*, vol. 94, pp. 073903:1–4, 2005.

[3] M. V. Kotlyar, T. Karle, M. D. Settle, L. O. Faolain, and T. F. Krauss, "Low-loss photonic crystal defect waveguides in InP," *App. Phys. Lett.*, vol. 84, May 2004.

[4] J. Zimmermann, H. Scherer, M. Kamp, S. Deubert, J. P. Reithmaier, A. Forchel, R. März, and S. Anand, "Photonic crystal waveguides with propagation losses in the 1db/mm range," *J. Vac. Sci. Technol. B*, vol. 22, pp. 3356–3358, Nov/Dec 2004.

[5] J. Yamauchi, M. Sekiguchi, O. Uchiyama, J. Shibayama, and H. Nakano, "Modified finite-difference formula for the analysis of semivectorial modes in step-index optical waveguides," *Photon. Technol. Lett.*, vol. 9, p. 961, 1997.

[6] W. Kuang, C. Kim, A. Stapleton, W. J. Kim, and J. D. OBrien, "Calculated out-of-plane transmission loss for photonic-crystal slab waveguides," *Opt. Lett.*, vol. 28, pp. 1731–1783, 2003.

[7] M. J. Connelly, *Semiconductor Optical Amplifiers*. Dordrecht, The Netherlands: Kluwer, 2002.

[8] S. Mahnkopf, H. Hsin, G.-H. Duan, F. Lelarge, T. Happ, M. Kamp, R.März, and A. Forchel, "Wavelength switching by mode interference between longitudinally coupled photonic crystal channel waveguides," *Elect. Lett*, vol. 40, pp. 29–30, January 2004.

[9] T. D. Happ, A. Markard, M. Kamp, J.-L. Gentner, and A. Forchel, "Short cavity InP-lasers with 2D photonic crystal mirrors," *IEE Proc.-Optoelecton.*, vol. 148, pp. 183–187, August 2001.

[10] M. L. Mašanović, V. Lal, J. A. Summers, J. S. Barton, E. J. Skogen, L. G. Rau, L. A. Coldren, and D. J. Blumenthal, "Widely-tunable monolithically-integrated all-optical wavelength converters in InP," *J. Lightwave Technol.*, vol. 23, pp. 1350–63, 2005.

[11] C. K. Madsen and J. H. Zhao, *Optical Filter Design and Analysis: A Signal Processing Approach*. New York: Wiley-Interscience, 1999.

[12] A. S. Jugessur, P. Pottier, and R. M. D. L. Rue, "Microcavity filters base-don hexagonal lattice 2-D photonic crystal structures embedded in ridge waveguides," *Phot. Nanostruc. Fund. Appl.*, vol. 3, pp. 25–29, 2005.

[13] L. A. Coldren and S. W. Corzine, *Diode Lasers and Photonic Integrated Circuits*. New York: Wiley-Interscience, 1999.

[14] F. Laermer, A. Schilp, K. Funk, and M.Offenberg, "Bosch deep silion etching : Improving uniformity and etch rate for advanced MEMS applications," *MEMS 99 Technical Digest*, pp. 211–216, 1999.